

Ph.D. Dissertation 7740

RADIO ECHO STUDIES OF GLACIERS

by

BEVERLEY MICHAEL EWEN SMITH



A dissertation submitted for the degree of Doctor  
of Philosophy in the University of Cambridge.

Churchill College.

Cambridge.

May 1971

## PREFACE

The work described in this dissertation was carried out under the helpful guidance of my supervisor, Dr.S.Evans in the Scott Polar Research Institute, from January 1968 to January 1971.

The experimental work, discussion and figures are, unless otherwise stated, the original work of the author. The dissertation does not exceed 80 000 words and has not been submitted for a degree at any other University.


During December 1967, field work was carried out in the Antarctic with a party from the Scott Polar Research Institute. The work was made possible by the logistic capabilities of the United States Navy, under the auspices of the National Science Foundation of America.

During May 1968, field work was carried out in Norway with the assistance of T.M.Randall and the facilites of the Norwegian Water Resources and Electricity Board.

During the period between December 1969 and February 1970, field work was carried out in the Antarctic Peninsula with the logistic support of the British Antarctic Survey.

I am indebted to the British Antarctic Survey for financial support throughout the period of research, and to Dr.C.W.M.Swithinbank of the Survey, whose enthusiasm and advice have contributed much to the work.

I thank Dr.G.deQ.Robin, Director of the Scott Polar Research Institute, for his interest in the subject, and for making available the facilities of the Institute.



## Radio echo studies of glaciers - A summary

---

There is a need for measurements of the thickness of glaciers, ice sheets, and ice shelves. Radio waves propagating in naturally occurring ice masses are attenuated by absorption in the conducting medium, by reflection from discontinuities, and by scattering from inhomogeneities. These scattering centres may be impurities, free water, or solid ice within less dense firn. A v.h.f. radar system has been designed specifically to produce continuous profiles of ice thickness when used either on the surface of a glacier, or in an aircraft flying over it. The frequency dependence of the attenuation mechanisms influences the choice of radio frequency used by the echo sounder. Electronic control and annotation circuits have been developed for use in the echo sounder and its data recording system, to simplify field operation and avoid errors caused by mistakes in manual recording and annotation. The author has tested the equipment on glaciers in Norway and in the Antarctic, where extensive measurements of ice thickness



have been made both in Eastern Antarctica and in the Antarctic Peninsula. Information about glacier temperature and structure, and about the nature of the subglacial media, is also obtained. Measurements of ice thickness made from an aircraft, require navigational data to be used to determine the location of measurements. A digital computer has been used to analyse the available aircraft flight parameters and other navigational information, and to produce position coordinates which are collated with thickness measurements. Consideration has been given to the effect of random and systematic errors in the measurements, on the information obtained. Methods of presenting the measurements, which are distributed along flight lines, have been explored. An algorithm has been developed to produce contour maps of such measurements, with particular application to computer methods.

## CONTENTS

-----

Preface	
Summary	
Contents	
Chapter 1 - Development of the radio echo sounding technique	
1.1 Introduction	1
1.2 Choice of frequency and mode	3
1.3 Transmitter	7
1.4 Receiver	9
1.5 Aerial and transmit-receive switch	11
1.6 Recording of data	14
1.7 Parallel developments	18
Chapter 2 - Mark 4 radio echo sounder : timing circuits	
2.1 General objectives	20
2.2 Basic timing pulses	25
2.3 Sequencing of events	31
2.4 Character generation	36
2.5 Output facilities	41
2.6 Radio echo navigational aid	44
Chapter 3 - Factors affecting the strength of the received signal	
3.1 General considerations and geometrical effects	48
3.2 Electromagnetic parameters and reflection coefficients	54

3.3	Three layer problem	60
3.4	Surface melt layer	63
3.5	Brine percolation layer	67
3.6	Rain soaking of firn	69
3.7	Solid ice layering within firn	71
3.8	Scattering losses	72
3.9	Background signal due to scatter echoes	76
Chapter 4 - Field work		
4.1	Radio echo sounding of the Antarctic Ice Sheet, 1967	81
4.2	Results of the 1967 Antarctic season	84
4.3	Temperate glacier experiments	88
4.4	Antarctic Peninsula radio echo sounding, 1969-70	93
4.5	Results of the 1969-70 Antarctic Peninsula season	98
4.6	Note regarding iceberg '1967-A'	103
Chapter 5 - Navigational methods		
5.1	Available data	105
5.2	Dead reckoning methods	110
5.3	Position fixing methods	114
5.4	Navigational accuracy in general terms	118
5.5	Random errors in dead reckoning	122
5.6	Systematic errors in dead reckoning	124
5.7	Information gained	131

Chapter 6 -	The presentation of radio echo sounding results	
6.1	The purpose of presentation and the distribution of the data	139
6.2	Notes on the data used to illustrate the methods of presentation	141
6.3	Presentation methods applicable to all distributions of data	142
6.4	Presentation methods applicable to linearized data	143
6.5	Generalizing data using polynomials	146
6.6	Generalizing data using other algorithms	149
References		153

## CHAPTER 1

### Development of the radio echo sounding technique

#### 1.1 Introduction

Prerequisite to a complete understanding of the physics of naturally occurring ice masses, is a knowledge of their dimensions. The horizontal extent of glaciers and ice sheets can be determined using conventional surveying techniques; the measurement of ice depth or thickness is the subject of this dissertation.

The usual method of measuring the depth of glaciers has been seismic reflection shooting (Robin 1956). Other methods have included the interpretation of gravity variations (Bull and Hardy 1956), electrical resistance between spaced electrodes (Röthlisberger 1967), surface height of floating ice shelves (Robin 1958), and use of the relationship between surface slope and ice thickness for the large inland ice sheets (Nye 1952). Except for direct measurement by drilling to bedrock (Gow et al 1968), seismic measurements are usually more reliable than other techniques and a figure of  $\pm 10$  m accuracy is representative (Bentley 1964). The gravity method gives good relative depths in areas where the topography is favourable and it has often been used to interpolate between more widely spaced seismic soundings.

The suggestion that naturally occurring ice masses are transparent to radio waves has come from several independent sources. As early as 1927 radio methods were proposed for the

measurement of glacier thickness by Stern (1930) but development was limited by the available technology. When aircraft became equipped with radio altimeters (terrain clearance radar) there were reports of gross errors indicated over ice masses in polar regions. These reports were investigated by Steenson (1951) who suggested that development might lead to a technique for measuring ice thickness. His suggestion was not pursued but subsequent aircraft incidents led to experiments by Waite and Schmidt (1962) using an aircraft radio altimeter (SCR 718) on the surface of a glacier. Some measurements of thickness were obtained using this instrument.

Independently of the altimeter experiments, Evans (1961) investigated ionospheric sounder records obtained at stations situated on ice. These records showed an interference pattern caused by power reflected from the base of the ice mass. Evans (1963) describes how this evidence for the transparency of ice stimulated a design for a radio echo sounder specifically intended to measure ice thickness.

## 1.2 Choice of frequency and mode

The radio altimeter experiments were conducted using a pulse modulated transmission on a frequency of 440 MHz, while the ionospheric sounder results were obtained using a frequency modulated continuous wave transmission on frequencies below 30 MHz. In designing an instrument specifically for the measurement of polar ice thickness, it should be remembered that unlike an aircraft radio altimeter or a short range harbour radar, the transmitted wave propagates through a medium which exhibits absorption, scattering and refraction.

A pulse modulated system was chosen in preference to a frequency modulated system because of the relative ease of interpreting the received signal. A pulse modulated system is simpler than a frequency modulated system which would require a channel analyser to obtain the same type of display necessary when there may be several echoes at different ranges. The desired accuracy and resolution imposes a minimum limit on the width of the frequency spectrum. In order to match the accuracy of the seismic method, a range resolution of  $\pm 10$  m is required. The velocity of v.h.f. radio waves in ice is  $169 \text{ m } \mu\text{s}^{-1}$  (Evans 1965) so that a pulse rise time of 120 n s, or a bandwidth of at least 4 MHz, is required to obtain the desired resolution.

To avoid echoes from the ionosphere and confusion with long distance communications there is no entirely safe lower limit of

frequency particularly if we remember that the region to be studied includes the auroral zone. Radar echoes may be received at frequencies up to several hundred megahertz from auroral ionization, but with the power and beam width which we might use, these echoes will be rare at frequencies above 30 MHz for most of the sunspot cycle (see for example Tolstikov et al 1966).

It is obvious that the mechanical problems of supporting the aerial will become increasingly difficult at lower frequencies but more important, it is necessary to maintain the impedance bandwidth to accommodate the pulse rise time. The lower limit of frequency is similar to that obtained above. The aerial gain which can be obtained at low frequencies is not likely greatly to exceed that of an elementary dipole.

The effects of scattering are considered in detail in chapter 3 but for the time being we will state that the effect of scattering by bubbles or other inhomogeneities on the received echo strength is small at frequencies below 1000 MHz.

Absorption in the conducting medium is one of the most important considerations in the choice of carrier frequency. In chapter 3 we consider the electrical properties of ice and snow. Figure 1.2.1 shows the absorption per 100 m path in polar ice as



frequency particularly if we remember that the region to be studied includes the auroral zone. Radar echoes may be received at frequencies up to several hundred megahertz from auroral ionization, but with the power and beam width which we might use, these echoes will be rare at frequencies above 30 MHz for most of the sunspot cycle (see for example Tolstikov et al 1966).

It is obvious that the mechanical problems of supporting the aerial will become increasingly difficult at lower frequencies but more important, it is necessary to maintain the impedance bandwidth to accommodate the pulse rise time. The lower limit of frequency is similar to that obtained above. The aerial gain which can be obtained at low frequencies is not likely greatly to exceed that of an elementary dipole.

The effects of scattering are considered in detail in chapter 3 but for the time being we will state that the effect of scattering by bubbles or other inhomogeneities on the received echo strength is small at frequencies below 1000 MHz.

Absorption in the conducting medium is one of the most important considerations in the choice of carrier frequency. In chapter 3 we consider the electrical properties of ice and snow. Figure 1.2.1 shows the absorption per 100 m path in polar ice as

a function of frequency, with temperature as parameter. The data are derived from measurements by Westphal (1963 private communication) at frequencies above 150 MHz, and from measurements by Paren (1970) at 100 KHz. Both sets of measurements were made on samples of deep ice from the Greenland ice sheet. It may be seen that absorption increases steeply at frequencies above 500 MHz and it should be added that field measurements (Walford 1968, Weber and Andrieux 1969) suggest that absorption rises from 100 MHz upwards. It is unfortunate that accurate absolute field measurements of echo strength at different frequencies have not been made. The Westphal measurements used to construct figure 1.2.1 apply to only one ice sample with no indication of the variations to be expected in nature. In figure 1.2.2 we have included the effect of aerial gain in the strength of the received echo. The figure shows the signal to noise ratio of an echo assuming a transmitter peak power of 500 W, a receiver noise level of 0.1 pW and perfect reflection at a plane ice/bedrock interface. The aerial gain is assumed to be 1.6 below 100 MHz and the aperture is assumed to be a constant  $1 \text{ m}^2$  above 100 MHz. The temperatures and thicknesses chosen indicate some likely examples although the temperature in polar ice sheets is not, of course, constant with depth.

There are no marked variations in the transmitter and receiver performance which can be realized in the v.h.f. spectrum. A carrier frequency of 35 MHz was chosen, with a 3 dB bandwidth of

$\pm 7$  MHz so that the lower limit approached the restrictions mentioned earlier. The lowest frequency was chosen because of the uncertainty in dielectric properties at higher frequencies and, to a lesser extent, because of the slightly simpler engineering involved in the r.f. circuitry.

Evans (1963) describes the development of the first version of the instrument which was called the SPRI Mark 1 echo sounder. This early version was used in the field by Walford (1964, 1967 and 1968). The important parameters are included in table 1.7.1. More recently, an improved version called the SPRI Mark 2 using more modern techniques, was described by Evans and Smith (1969). In an attempt to produce a version which was particularly suitable for use on temperate glaciers, the Mark 3 versions have been similar to the Mark 2 but with alternative carrier frequencies. The Mark 4 version is the most recent, having similar r.f. circuits to the Mark 2 but incorporating refined timing and control circuits, which are described in chapter 2. In the remainder of this chapter we consider the r.f. circuits of the Mark 2, 3 and 4 versions.

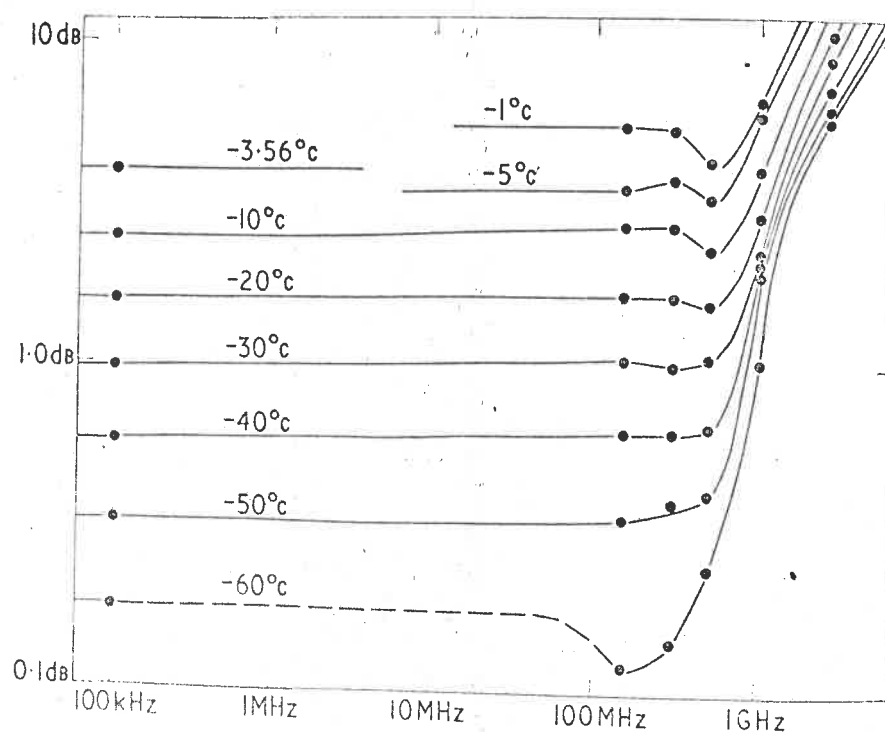


Figure 1.2.1

Absorption per 100 m path in polar ice, as a function of frequency, with temperature as parameter.

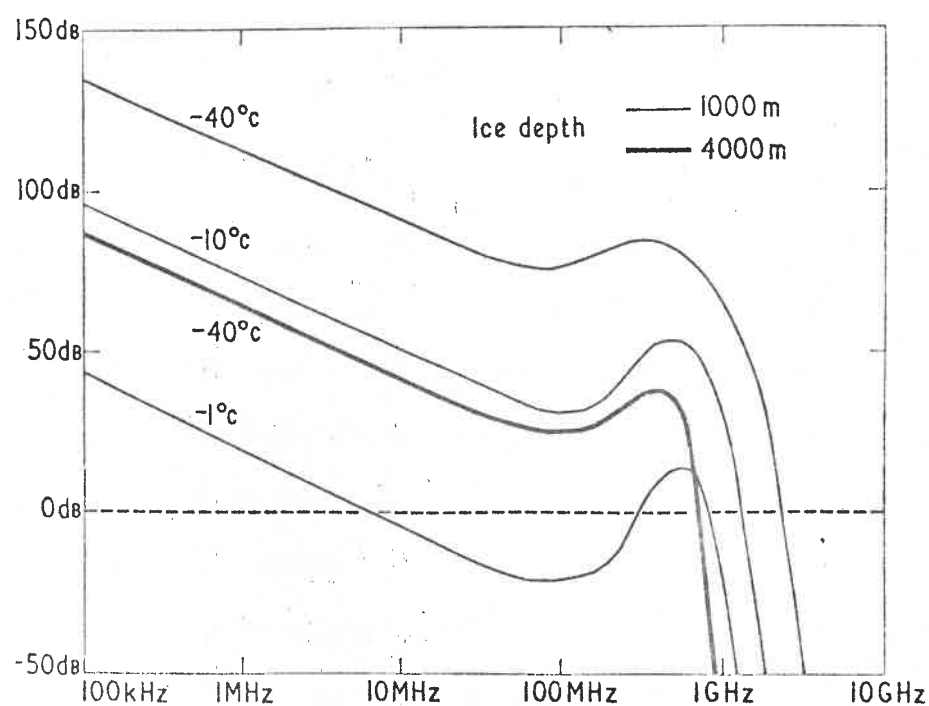


Figure 1.2.2

Echo signal-to-noise ratio for 500 W peak transmitter power, a receiver noise level of 0.1 pW and perfect reflection at an ice/bedrock interface; the aerial gain is assumed to be 1.6 below 100 MHz and the aperture is assumed to be  $1 \text{ m}^2$  above 100 MHz.

### 1.3 Transmitter

In order to obtain the maximum practical peak power from the transmitter, a thermionic design was chosen for this unit. A solid state version would probably have a peak power little more than its maximum mean power but in the case of thermionic designs, the peak power may be much greater than the mean. The mean power is dictated by the pulse repetition frequency (p.r.f.) and the pulse length. In order to resolve two echoes which are at similar ranges, the minimum pulse length which can be reproduced in the available bandwidth is chosen. The interval between pulses must be greater than that which corresponds to the range of the most distant echo. It may be assumed that more than 5000 m of ice will not be encountered, but allowance must be made for the possible height of the instrument above the surface if it is used in an aircraft. In section 1.6 we will see that it is desirable to use the highest p.r.f. within the limits stated. Figure 1.3.1 shows a schematic diagram of the transmitter circuit which is common to the Mark 2, 3 and 4 versions of the echo sounder. The p.r.f. of the Mark 2 and 3 versions was  $64 \mu\text{S}$ , that of the Mark 4 version is either 40 or  $80 \mu\text{S}$ . The Mark 2 version had a pulse length of 240 nS at 35 MHz. The Mark 4 version is similar but a recent modification to 60 MHz (to simplify aerial problems) has coincided with a reduction in the pulse length. The Mark 3 version has been used on several frequencies higher than 35 MHz and usually

associated with a reduced pulse length.

The operation of the transmitter is as follows: The trigger for the transmitter is derived from a blocking oscillator transformer which is d.c. coupled to the grid of the 3D21 modulator, driving it from - 50 v to + 30 v ( $I_g = 30$  mA) during the pulse. The anode current of the 3D21 rises to 1.5 A in 300 nS through a 150  $\mu$ H inductor storing  $\frac{1}{2} L I^2 = 0.2$  mJ, which discharges on the overshoot into the screen grids of the QQV06/40A tetrodes, raising them to +400 v. The tank circuit has a loaded Q of 10 to permit the short rise time. The series tuned output coupling loop has a Q of 2 in isolation, and for optimum coupling the output power is greater than 500 W into 50 ohm. An increase in the power supplied to the transmitter has raised the peak power to about 1.5 kW in the Mark 4 version. Figure 1.3.2 shows an oscillogram of the transmitted pulse.

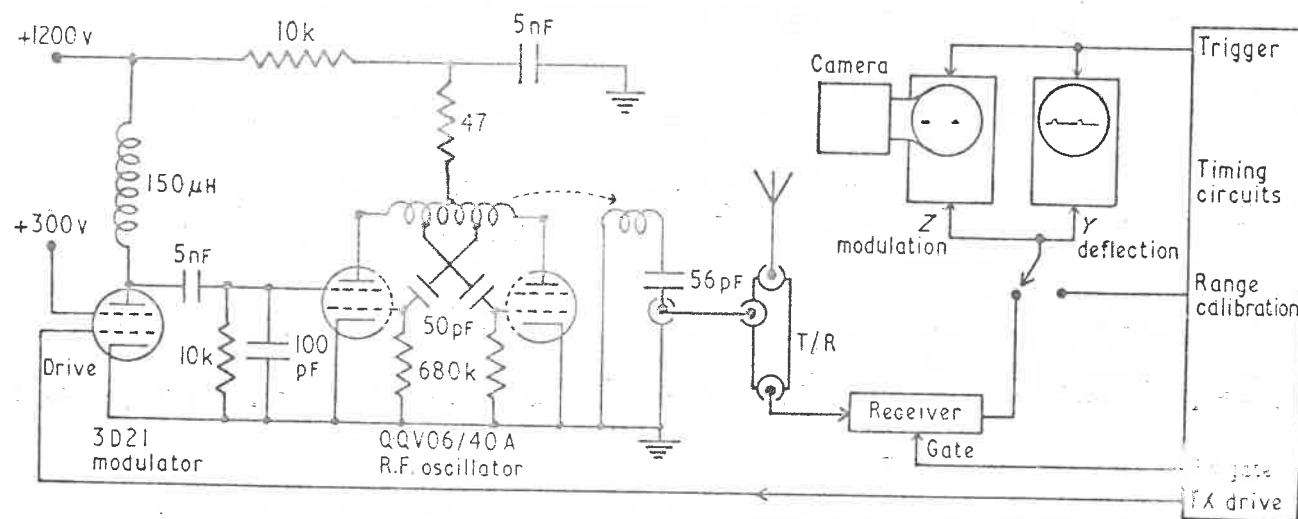


Figure 1.3.1

Schematic diagram of the Mark 2 radio echo sounder.



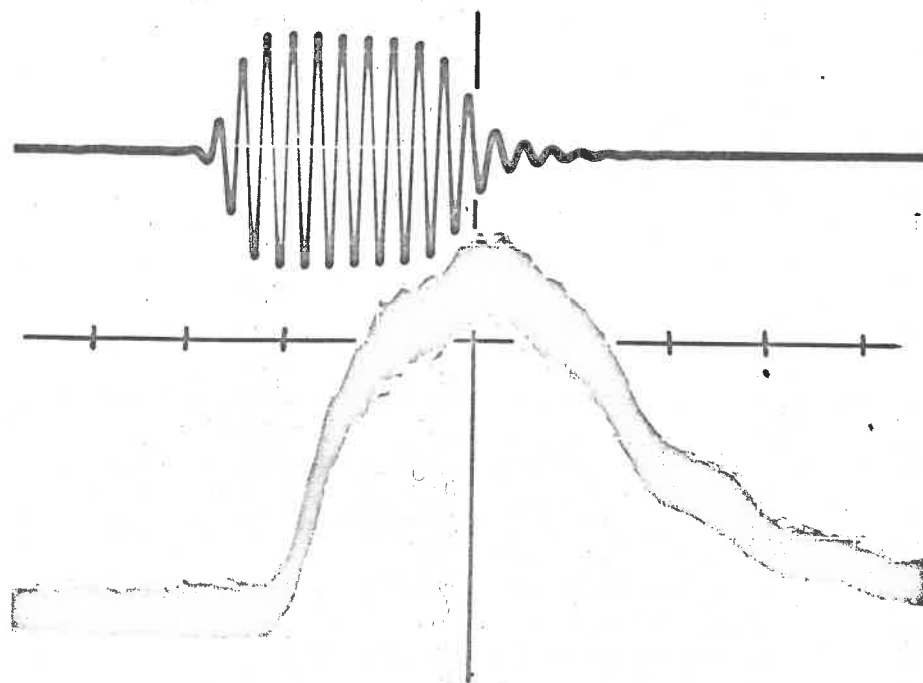


Figure 1.3.2

Oscillogram showing the r.f. transmitted pulse and the receiver output when the same signal is attenuated through 155 dB and fed into the receiver aerial input; one division on the horizontal scale represents  $0.1\mu\text{S}$ .

#### 1.4 Receiver

The receiver used in the Mark 2 version of the echo sounder included four stages of r.f. amplification using transistor type 2N918. Stagger tuning was used to achieve a 3 dB bandwidth of 14 MHz and a midband gain of 93 dB. There is no frequency conversion so that effective screening and filtering are necessary for stability and also for accuracy since it must be ensured that both the direct transmitter pulse and the received echo suffer the same time delay in passing through the whole receiver. Figure 1.3.2 shows an oscillogram of the receiver output for an input pulse which is about 10 dB above the input noise level. The proximity of the video and radio frequency bands requires particular attention to be paid to filtering. With five tuned stages in the receiver, the gain will fall at 60 dB per octave at frequencies far removed from the pass band. The video gain is 35 dB and the output falls at 18 dB per octave from 7 MHz upwards. It is clear that the response between 10 and 20 MHz is only just acceptable.

The recovery of the receiver after a large overload was not entirely satisfactory. In order to minimize the strength of very large signals a transmit-receive switch (described in the next section) is included in figure 1.3.1. This ensures that the input signal to the receiver does not exceed 1.5 v in 50 ohm. The receiver was suppressed during the transmitter pulse by removing the power supply, but during experiments in the field (section 4.1)

it was found that the strength of the surface echo when operating in an aircraft, was often sufficient to produce a significant change in the biasing of some of the receiver stages. This had the effect of reducing the receiver sensitivity and producing a threshold below which received signals were not detected. This unfortunate occurrence would have caused weak echoes to be lost but instead, the receiver was suppressed during the surface echo as well as during the transmitter pulse and the range of the surface was measured separately with a microwave surface altimeter. Subsequent versions of the equipment have used a different receiver in which more attention was paid to the design of a stable operating point. In the Mark 4 equipment, a non-linear filter was imposed on the output of the receiver to reduce the dynamic range of the signal. The filter consisted of a ladder of diodes connected so that the effective load resistance on the signal path increased as the signal level increased. More recently, the receiver has been modified to use integrated circuits in a logarithmic amplifier. The output of this receiver had a dynamic range of 10 dB, which is within that tolerated by the recording method, for input signals in a 60 dB range. This means that constant adjustment is no longer required to maintain the echo strength within the range of the recording method.

### 1.5 Aerial and Transmit-Receive Switch

The need for a 10 MHz bandwidth on a carrier frequency of 35 MHz makes considerable demands on the aerial design. Walford (1964) used quarter wavelength unipoles on a surface vehicle for experiments with the Mark 1 version. A folded quarter wavelength dipole can be made to have a wide impedance bandwidth by making the conductors thick. Unfortunately, any practical installation requires the aerial to be near some conducting surface, especially on an aircraft. Coupling to the image in the metal surface invariably reduces the impedance bandwidth to less than that which is required. Experiments using multiple conductors to increase the 'electrical thickness' of the aerial were made by Evans and Robin (1966) and Swithinbank (1968). More recently a terminated dipole has been used to achieve the desired impedance bandwidth. Bailey (1951) describes how the forward field strength is not greatly reduced by dissipation in the terminating resistor because the current distribution is almost constant along the wire. In addition, the flattest impedance characteristic is obtained with aerial lengths between a half and a full wavelength, so that the gain is somewhat greater than that of a half wave dipole. Figure 1.5.1 shows the aerial dimensions for a 35 MHz sounder. The impedance is such that the v.s.w.r. is less than 2 between 30 and 40 MHz. In the diagram, the aerial is shown a quarter wavelength below a reflecting surface. It has been found impossible

### 1.5 Aerial and Transmit-Receive Switch

The need for a 10 MHz bandwidth on a carrier frequency of 35 MHz makes considerable demands on the aerial design. Walford (1964) used quarter wavelength unipoles on a surface vehicle for experiments with the Mark 1 version. A folded quarter wavelength dipole can be made to have a wide impedance bandwidth by making the conductors thick. Unfortunately, any practical installation requires the aerial to be near some conducting surface, especially on an aircraft. Coupling to the image in the metal surface invariably reduces the impedance bandwidth to less than that which is required. Experiments using multiple conductors to increase the 'electrical thickness' of the aerial were made by Evans and Robin (1966) and Swithinbank (1968). More recently a terminated dipole has been used to achieve the desired impedance bandwidth. Bailey (1951) describes how the forward field strength is not greatly reduced by dissipation in the terminating resistor because the current distribution is almost constant along the wire. In addition, the flattest impedance characteristic is obtained with aerial lengths between a half and a full wavelength, so that the gain is somewhat greater than that of a half wave dipole. Figure 1.5.1 shows the aerial dimensions for a 35 MHz sounder. The impedance is such that the v.s.w.r. is less than 2 between 30 and 40 MHz. In the diagram, the aerial is shown a quarter wavelength below a reflecting surface. It has been found impossible

to achieve this desirable dimension in some aircraft installations (see chapter 4). The impedance bandwidth is not degraded by proximity to a conducting surface but the aerial efficiency does deteriorate as more power is dissipated in the termination. None of the aerial systems which can be engineered at this low frequency have a narrow beam width. This means that the range measured, is that to the nearest normal reflecting surface. Since the ice/bedrock interface is not in general horizontal, the range which is measured is not the vertical depth. A subglacial profile is therefore distorted, becoming the locus of a normal reflector in any direction within the limit of the aerial beamwidth plus the effect of refraction (see chapter 3). Harrison (1970) has described how the original surface can be reconstructed from the record obtained in one dimension - along the path of movement. It is not possible to interpret non vertical echoes from either side of the track so that it is desirable to have a minimum beam width in the rolling plane (of an aircraft). For this reason, the terminated dipole is usually mounted perpendicular to the direction of movement, in spite of the undesirable drag this entails on an aircraft. Chapter 4 describes actual measurements of the polar diagram of this type of aerial.

Figure 1.5.2 shows the transmit-receive switch which uses lumped-element quarter wavelength sections to isolate the receiver from large signals. Silicon diodes (type 1N916) are used back-to-

back to provide the necessary backlash. Large signals from the transmitter are effectively connected to the aerial. In addition, the large voltage in the centre of the circuit causes the diodes to conduct and the short circuit thus caused produces an open circuit at the ends of the quarter wave sections. Power is therefore excluded from the receiver. When small signals return from the aerial, the transmitter is isolated because the diodes do not conduct and the two sections of transmission line leading to the receiver are unshorted. In this way the transmit-receive function is achieved without external switching. The isolation is better than 40 dB but is degraded if the aerial impedance is incorrect.

A lumped-element quarter wavelength section has also been used to speed the decay of the transmitter pulse. A pair of diodes shorting the remote end of a quarter wavelength transformer appear as an open circuit during large signals (transmission) and a short circuit when the voltage falls below that which makes the diodes conduct. In this way the exponential decay of the transmitted pulse is truncated.

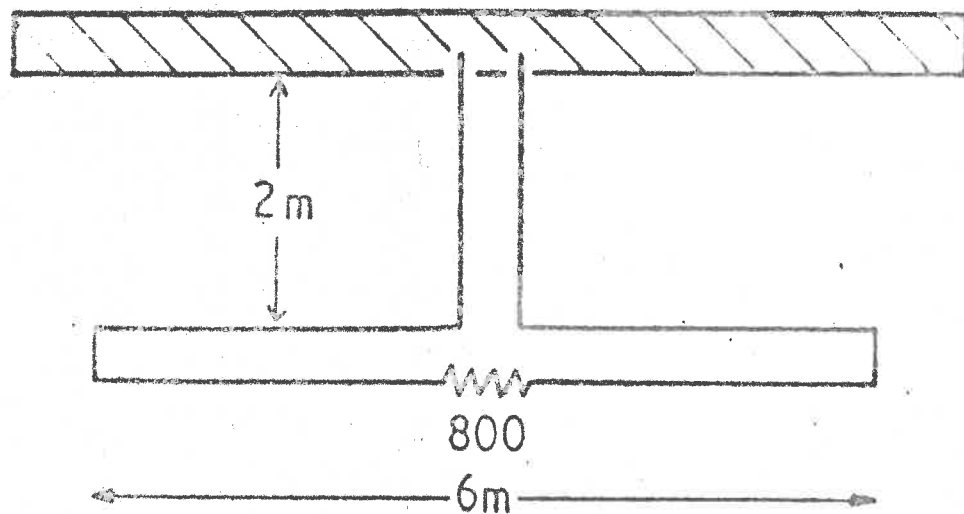


Figure 1.5.1

A terminated folded dipole which gives the desired impedance band width at  $35\text{ MHz}$ .



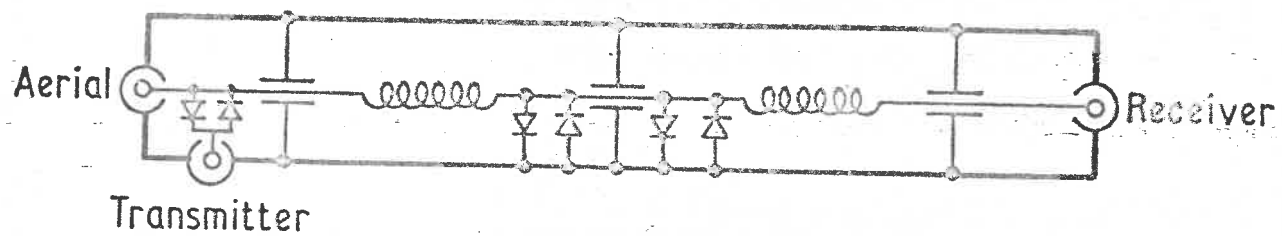


Figure 1.5.2

Schematic diagram of the transmit-receive switch.

### 1.6 Recording of data

For subsequent analysis it is necessary to record the data collected, and the quantities involved make photographic recording the most practical in spite of the need for processing facilities. We will see that there is a further advantage in using a photographic medium.

The video signal from the receiver is used to brightness-modulate an oscilloscope trace, as shown in figure 1.3.1. A camera records the appearance of the trace on a 35 mm film which is moved continuously so that the echo delay is measured across the film and time increases along it. The film therefore represents a profile of the range of reflecting surfaces in the field of view of the aerial. Echo delay may be measured from the film record to an accuracy which is dictated by the cathode ray tube spot size rather than the properties of the film or camera lens. On the fastest sweep range, the spot size is comparable to the overall equivalent rise time, but on slower sweeps the spot size limits the resolution to about 1 part in 200 of the total sweep width. A limit is imposed on the possible excursions of the video signal to prevent defocussing of the spot. The input attenuators in the receiver are adjusted by the operator to maintain the echo amplitude, which usually fluctuates with a Rayleigh probability distribution, within the dynamic range. The use of a logarithmic receiver makes this adjustment much less critical.

Without a logarithmic receiver, the absolute echo strength is indicated by the input attenuator setting to an accuracy determined by the dynamic range of the recording medium.

The use of photographic recording entails an increase in effective receiver sensitivity by an integrating process. The integrating action has been analysed as follows:

(i) Noise only. After a linear detector, in the presence of noise alone, the probability of obtaining an instantaneous video voltage  $r$  is (Lawson and Uhlenbeck 1950, p.61)

$$P(r) = \left(2r/k^2\right) \exp\left(-r^2/k^2\right)$$

It is a property of this Gaussian distribution that the mean square voltage  $\overline{r^2} = k^2$ , and the arithmetic mean voltage, or 'd.c. component' in electrical terms, is  $\overline{r} = k \left(\frac{1}{2\pi}\right)^{1/2}$ . It is on the basis of this latter relation that the output noise power has been measured in practice and, from the power gain in the linear region, the input noise power has been derived.

(ii) Noise plus signal. In the presence of a coherent or continuous-wave signal before detection, giving rise to an additional d.c. component  $s$  after detection, the probability distribution of the signal plus noise voltage is (Lawson and Uhlenbeck 1950, p154)

$$P(r) = \left(2r/k^2\right) \exp\left[-(r^2 + s^2)/k^2\right] I_0\left(2rs/k^2\right)$$

where  $I_0$  is the Bessel function of zero order and imaginary argument. The mean square voltage is  $\overline{r^2} = k^2 + s^2$  but there is no simple relation for the d.c. component. However, the properties of this distribution have been tabulated by Norton et al (1955) and from their data figure 1.6.1 has been drawn showing the probability that the instantaneous voltage will exceed any specified level. It is used as follows: on the abscissa a threshold level is found which is just sufficient for a single pulse to cause a detectable exposure of the film (this depends on the d.c. level of the cathode ray tube brightness control) and it is supposed that 1000 sweeps are integrated at a single point before the film advances by a distance equal to the spot diameter. Then, for example, if the threshold is + 6 dB above the r.m.s. noise level, a noise signal alone will exceed this level on 0.02 of the occasions, or 20 times per 1000 sweeps. Now consider the addition of a signal of strength - 6 dB, referred to the noise, and it can be seen that the threshold will be exceeded approximately 40 times per 1000 sweeps. This difference between the two observations, in the presence and the absence of the signal, could be established with a very high degree of certainty if individual occurrences were counted, but on the photographic film we consider a ratio of 2 : 1 in exposure to be the limit of distinction. Notice that the result is hardly affected by the adjustment of the threshold level, i.e. the brightness control, in the range 2 - 8 dB above

noise, and records of weak signals recorded in the laboratory have confirmed that a signal of strength - 6 dB is just detectable against the noise background.

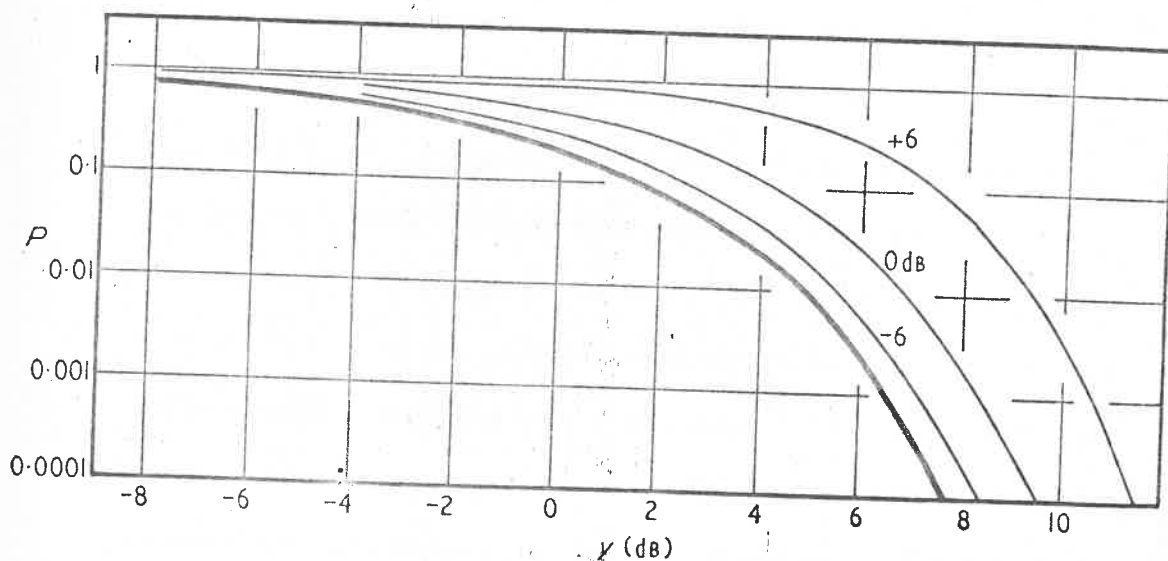


Figure 1.6.1

Probability  $P$  of a d.c. signal plus noise exceeding a given threshold  $\gamma$  in dB above r.m.s. noise volts, with signal-to-noise ratio as parameter; the thick line refers to noise alone.

### 1.7 Parallel developments

In addition to the radio echo sounding instruments developed at the Scott Polar Research Institute, there have been parallel developments by other bodies. In order to compare these instruments, figure 1.7.1 has been compiled to show the important characteristics. I am indebted to S. Evans for the parameters of the instruments not developed at SPRI. Each instrument is identified by an abbreviation and its carrier frequency. For each one, three important parameters are listed - range accuracy, absorption index, and scattering index.

The range accuracy is derived from the bandwidth of the instrument. The absorption index is a measure of the ability to detect echoes which are very attenuated. It is obtained by combining the system performance (ratio of transmitter power to minimum detectable received power including the integrating action of the recording system, if any) with the gain of the aerial system and the receiver aerial aperture. Note that for some aerials which are not efficient, the beam width may be less than that computed from the measured gain. The absorption index is expressed in dB relative to the figure obtained for the Mark 4 (35 MHz) version. The scattering index is the factor  $(G \lambda^4 / \ell)$ , (see chapter 3), expressed in dB relative to the figure for the Mark 4 (35 MHz) version. We will see in chapter 3 that it is this factor which is important for temperate glacier sounding where

bottom echoes may be masked by scattered echoes from inhomogeneities within the ice. To generalize, the absorption index is a measure of the performance of the equipment on deep polar glaciers and the scattering index is a measure of the performance of the equipment on temperate glaciers. The abbreviations are as follows:

SPRI	Scott Polar Research Institute
USAEL	US Army Electronics Laboratory
TUD	Technical University of Denmark.
ANARE	Australian National Antarctic Research Expeditions
DEMR	Department of Energy, Mines and Resources, Canada
USSR	Arctic and Antarctic Research Institute, USSR
HALS	Consulting engineer, Oslo, Norway
ADCOLE	Corporation - for US Army Cold Regions Research and Engineering Laboratory

The SPRI instruments have their respective 'Mark' designations. The abbreviation n.b. denotes a narrow band option of the particular instrument. The instrument 'SPRI (projected)' is the author's suggestion for a temperate glacier sounder using a low frequency and having a low resolution. It is intended to overcome the temperate glacier problems reported in section 4.3.



Equipment	Frequency (MHz)	Accuracy (m)	Absorption index (dB)	Scattering index (dB)
SPRI Mk 1	35	7	-27	-4
SPRI Mk 2	35	5	0	0
SPRI Mk 3	480	2.5	-22	-33
SPRI Mk 3	150	2.5	-15	-17
SPRI Mk 3	60	3	-3	-2
SPRI Mk 4	35	5	0	0
SPRI Mk 4	60 {	5	+6	-5
	n.b.	50	+16	-12
SPRI (projected)	6	60	+19	+37
USAEL SCR718	440	20	-48	-44
USAEL (1964)	30	20	-3	+3
TUD	60 {	5	+18	+4
	n.b.	60	+30	-8
TUD	300	5	-3	-22
ANARE (1969)	100	7	+6	-18
DEMR (1969)	623 {	2.5	-10	-35
	n.b.	7	-5	-42
USSR IM4	213	60	+16	-35
HALS	80	5	-46	-12
HALS	205	5	-47	-29
ADCOLE	150-600	0.15	-74	-12

Figure 1.7.1

Comparison of radio echo sounders.

## CHAPTER 2

### Mark 4 radio echo sounder: timing circuits

#### 2.1 General objectives

The design of the timing circuits used in the Mark 4 radio echo sounder was the responsibility of the author. The principal purpose of this module is to control the sequence of events in the echo sounder. In the Mark 2 version, the timing circuits functioned solely to provide calibration pulses at  $2\mu\text{S}$  intervals and transmitter trigger pulses at  $64\mu\text{S}$  intervals. These pulses were derived from a 500 kHz oscillator using an integrated circuit divider chain. A number of improvements were envisaged for the Mark 4 system and the timing circuits were designed to play a more complicated part in the functioning of the equipment.

A season using the Mark 2 sounder in the field had revealed several shortcomings. These were mostly of a practical rather than theoretical nature. The problem of receiver transient response has already been discussed. In the field, the author was aware that a great deal of time was spent on manual annotation of the radio echo film record and SFIM chart, so that they could be collated with other data, mostly noted by hand, at a later date. During actual flying operations most of the time was spent noting the routine changes and adjustments which were made to the equipment. It was reasoned that if these mundane activities were automated, more time would be available for maintaining optimum operation of

the equipment, and errors in manual recording could be eliminated. Accordingly, automatic annotation is one of the functions of the new timing circuits. This is achieved using a numeric character generator which displays figures on the recorder and monitor oscilloscopes so that they can be read from the resulting film record.

It was shown in chapter 1 that the film record performs an integrating function, so that the receiver sensitivity is increased by the large number of echoes recorded on one spot of the film. For this, it is clearly desirable to have a maximum transmitter pulse repetition frequency (p.r.f.) up to the limit imposed by the transit time of the most distant echo. For this reason the  $64\mu\text{S}$  p.r.f. of the Mark 2 radio echo sounder is replaced by a choice of 40 or  $80\mu\text{S}$  p.r.f. in the Mark 4 timing circuits, these times correspond to maximum ranges of 6 000 and 12 000 metres in air, respectively.

The Mark 2 equipment made use of the internal timebases of the recording and monitoring oscilloscopes for the trace sweep. Since the recorder and monitor were independent, there was always a danger that while an echo might be visible on the monitor, it might not be on the screen of the recorder (which cannot be seen without removing the camera) and the information might therefore be lost. Furthermore if the timing circuits were to generate numeric characters on the screens of the cathode ray tubes, it would require

access to both X and Y deflections as well as to the Z modulation input. For these reasons, a linear sweep generator is included in the new timing circuits, and those in the oscilloscopes are ignored, being available as a stand-by in the event of a failure.

In the Mark 2 equipment, the oscilloscope sweep was triggered by the same pulse as the transmitter, and therefore the transmitter pulse was always close to the start of the sweep. If the sounder was operated in an aircraft flying at a great height, the sweep scale had to be compressed to include the surface and bottom echoes, although they might then occupy only a small part of the trace length. This problem is overcome in the Mark 4 version by triggering the sweep generator at a selectable and well defined time after the transmitter pulse.

The camera used in the Mark 2 equipment had a stepping motor which required a particular type of square waveform to operate it. This had been provided by an astable oscillator in the camera. In the Mark 4 version the pulses are provided by the timing module, from a more stable source at frequencies which are selectable on the instrument front panel. It is also desirable to be able to advance the camera by means of pulses from an odometer wheel which might be towed if the echo sounder was used on a sledge, so that distance along the film record is proportional to distance moved. An interface to allow this, is included in the Mark 4 timing circuits.

The clock function, (calibration once per minute for example)

which was provided externally in the Mark 2 system, is included in the Mark 4 timing module. This simplifies the annotation circuits by avoiding the need for an interface with a proprietary digital clock.

The sequence of events which was chosen for the Mark 4 system is as follows: at the beginning of each minute the calibration marks (calpips) are displayed for 0.5 seconds; then the numeric information is displayed for 0.5 seconds; for the remaining 59 seconds the transmitter is triggered at the chosen rate and the received signal is displayed.

An experimental one-range 'Radio Echo Navigational Aid' (RENA) was devised which would provide primitive navigational information with only slight modification of the equipment.

The following numeric information is displayed on the oscilloscopes as ten decimal digits: the time in hours and minutes (1, 2, 3, 4); the attenuator setting in dB (5, 6); one digit describing the transmitter advance and calpip frequency (7); and three digits showing the RENA value (8, 9, 10). As an alternative to the RENA function, a dummy card is provided which can be coded to provide any three digits in the RENA position, and after the failure of the RENA experiment this was used to provide a date code on the film record. It is not necessary to annotate the film with the current setting of the transmitter p.r.f. since this does not materially affect the analysis of the radio echo record, but

merely improves its quality in certain circumstances. Since the annotation only occurs once in each minute, on the minute, indication of time in seconds is redundant.

The entire Mark 4 equipment was constructed in a proprietary (Vero Electronics Ltd.) modular rack system consisting of four 4" modules. Figure 2.1.1 shows the whole equipment and figure 2.1.2 shows the timing module detached from the frame. An abbreviated block diagram of the timing circuits is shown in figure 2.1.3. This will be referred to later. Texas Instruments Ltd. integrated circuits were chosen to be the basic circuit elements since they were readily available and the author was already familiar with their applications. The specification of the integrated circuits used, only guarantees operation down to 0°C but the circuit generates enough heat of its own, to maintain this internal temperature in any workable environment.

The components were assembled on to plug-in circuit cards which were accommodated in the module. This form of assembly was chosen for ease of construction and versatility. For example, alternative transmitter and receiver modules can be used with the same power supply and timing modules.

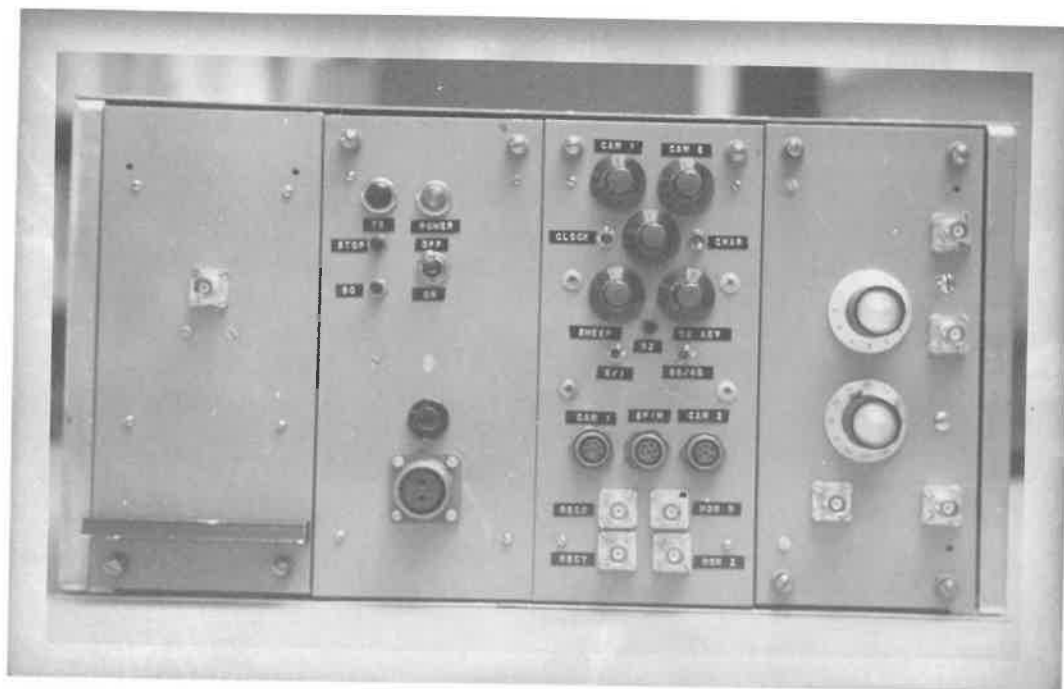


Figure 2.1.1

The front panel of the Mark 4 radio echo sounder.  
 From left to right : the transmitter ; the power supply ;  
 the timing module ; the receiver.

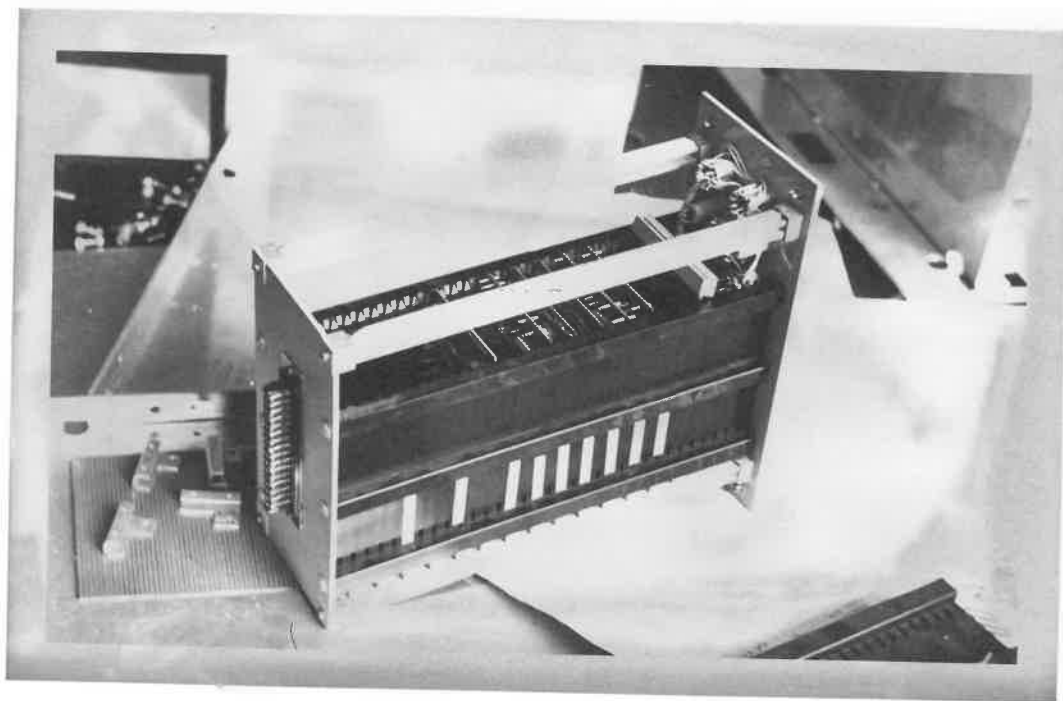


Figure 2.1.2

Showing the timing module removed from the equipment rack. All components are mounted on circuit cards which plug into the module. Connections to other modules are made through the plug on the end plate.



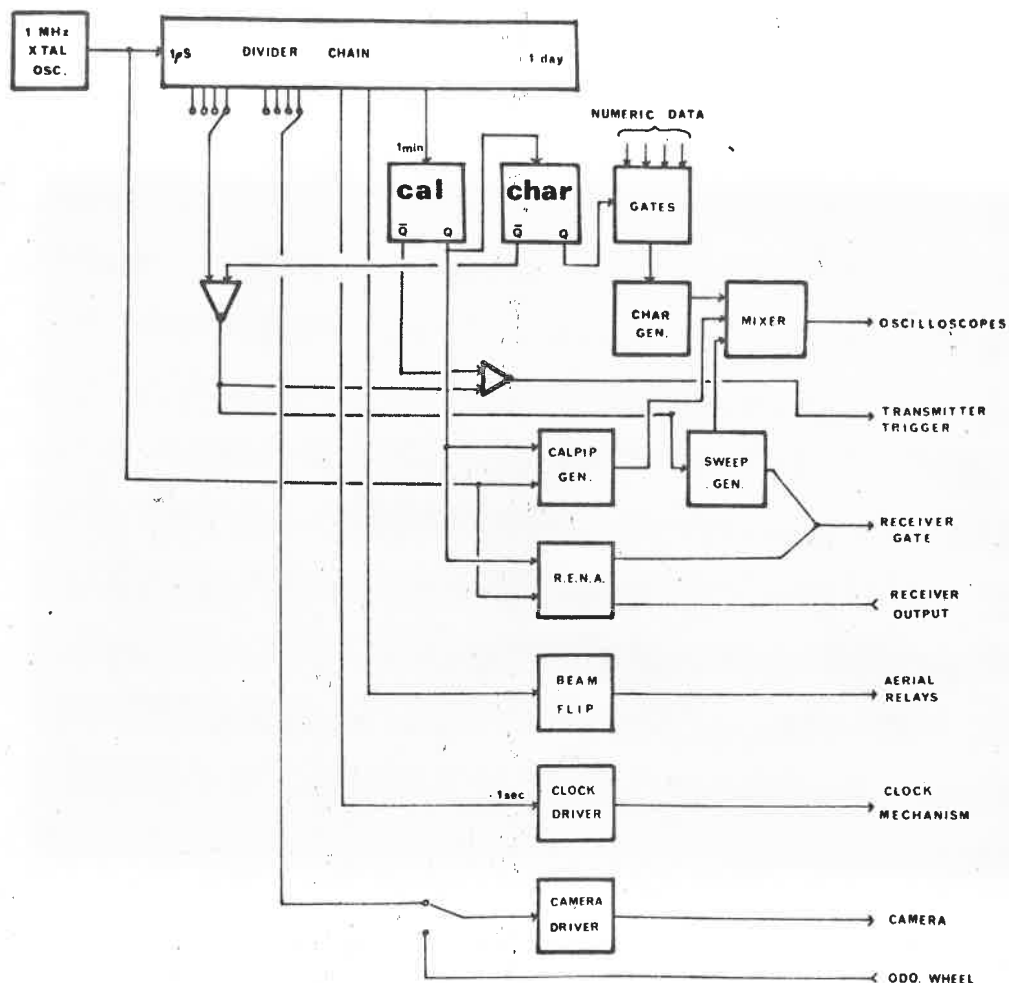


Figure 2.1.3

The block diagram of the timing circuits showing the crystal oscillator and divider chain which control the sequencing and annotation circuits.

## 2.2 Basic timing pulses

It may be seen from figure 2.1.3 that the fundamental source of all the pulses in the timing module is a 1 MHz quartz crystal oscillator. A schematic diagram of this circuit appears in figure 2.2.1. It is an emitter coupled oscillator using a series mode crystal, operating at its fundamental frequency. The crystal is the only frequency determining element and the loop gain of the oscillator is made deliberately small to avoid oscillation at overtones and maintain stability. There is no temperature stabilization because the long term stability of about 1 part in  $10^5$  is adequate for our purposes and an oven would be inconveniently bulky and wasteful of power. The oscillator is followed by an amplifier and buffer (not shown) which produce a 5 volt square wave having levels and rise times compatible with the transistor-transistor logic (TTL). This square wave with a period of  $1\mu\text{S}$  is the basis of all other waveforms. As far as possible, other rate determining circuits are avoided and replaced by counters driven from this master pulse train. This approach avoids the need for complicated setting-up procedures which might not be possible in a field situation due to the lack of test gear, and also prevents troublesome temperature effects which might otherwise occur.

Figure 2.2.2 shows the main divider chain which takes the  $1\mu\text{S}$  waveform and generates several waveforms ending with one having a period of 24 hours. Four types of circuit 'block' are shown and

these must be described before the nature of the various waveforms can be understood.

The simplest circuit blocks are those labelled '2'. As the name suggests these are bistable circuits which divide by 2. The output waveform has a mark-space ratio of unity, a change of state occurring on every negative edge of the input or clock waveform. By convention on figure 2.2.2 the input to each circuit 'block' is on the left hand side of the square, the output(s) come from the lower side, and reset inputs enter on the top.

The circuit blocks labelled '3' divide by 3 and therefore have two outputs to specify the three states. Often only the most significant output is used since this has one negative edge for every three input negative edges. This function is achieved using two J-K flip flops interconnected as shown in figure 2.2.3. A change of state of the output occurs on each negative edge of the input or clock waveform (t). The truth table of the combination shows how the count progresses. The arrangement escapes from  $Q_1 = Q_2 = 1$ , which should not normally occur, but might be the situation found when the power is turned on.

Blocks labelled '5' and '10' represent standard binary coded decimal (BCD) counters. Division by 5 is obtained by omitting the least significant binary count in the BCD series. The truth tables are as follows:

Count of 5  
(BCD without least  
significant bit.)

$Q_d$   $Q_c$   $Q_b$

0 0 0

0 0 1

0 1 0

0 1 1

1 0 0

0 0 0

etc.

Count of 10 (BCD)

$Q_d$   $Q_c$   $Q_b$   $Q_a$

0 0 0 0

0 0 0 1

0 0 1 0

0 0 1 1

0 1 0 0

0 1 0 1

0 1 1 0

0 1 1 1

1 0 0 0

1 0 0 1

0 0 0 0

etc.

It should be noticed that only the  $Q_a$  waveform has a unity mark-space ratio and we will refer to 'a', 'b', 'c' and 'd' type waveforms having mark-space ratios as defined in the above table. Notice that the 'd' type waveform is the most significant, it has only one negative edge for 10 (or 5 in the case of division-by-5) negative edges of the input waveform. On the block diagram in figure 2.2.2 the outputs are shown with increasing significance from left to right. The clock pulse for the next block always coming from the most significant or 'd' type waveform.

Starting from the  $1\mu\text{S}$  square wave output from the oscillator buffer there is first a division by 5. The  $1\mu\text{S}$  and the  $5\mu\text{S}$  period pulses are used to generate calibration marks or 'calpips'. Notice that the  $5\mu\text{S}$  waveform is a 'd' type. This is then divided by a factor of 2, four times. The outputs of these four bistables all have unity mark-space ratio with periods of 10, 20, 40, and

80  $\mu$ S. They are used to decode the transmitter trigger and sweep gate.

The 5  $\mu$ S waveform is also divided by 5, four successive times. At the end of these, the period of the resulting 'd' type waveform has a period of  $5 \times 5^4$  or 3125  $\mu$ S. This is more conveniently expressed as 320 Hz. The 'b', 'c', and 'd' type waveforms having a period of 125  $\mu$ S are used in the character pattern generation as we will see later.

The 320 Hz waveform is divided by  $2^5$  and each octave in frequency may be selected on the front panel to drive the camera circuitry. In this way camera speeds are available over a wide range and are adjustable by factors of two.

The 10 Hz pulse train which results from this last division feeds a divide-by-5 circuit. The 'b', 'c', and 'd' waveforms together with the output from the preceding divide-by-2 circuit (an 'a' type) constitute a BCD count having a period of 0.5 seconds. This count is decoded to gate the ten successive characters during the half second of numeric display.

The 'd' output is divided once more by 2 to give a 1 second period square wave. This is used to feed the drive circuits for an electromechanical clock escapement (Patek Philip Ltd.). The clock is used by the navigator, when airborne sounding, to time his observations.

The 1 second waveform is then divided by 10, by 3, and by 2

to give a square wave with period of 1 minute. The 1 minute pulses are used to initiate the display sequence at the start of each minute, a pulse at 30 seconds also being available should more frequent annotation and calibration be desired.

The 1 minute waveform is divided by 10, by 2, and by 3 to give a period of 1 hour. The outputs from these are decoded to give the time in minutes as two BCD 'words'. It is necessary to divide by 2 and then by 3 in order to obtain the correct BCD format using the three outputs as 'a', 'b', and 'c'. A 'd' type is not required for the tens-of-minutes since this figure is never more than 5 (in decimal).

The 1 hour waveform is then divided by 10, by 2, and by 2 in such a way as to reset to zero when 24 is reached. The 'c' bit from the BCD counter resets the most significant flip-flop in the tens-of-hours, and also resets itself when the most significant bit in the tens-of-hours is a '1'. These outputs are decoded to give the time in hours as two BCD words.

The setting up procedure for this divider, which has to synchronize with the electromechanical clock and with Greenwich Mean Time (by convention), caused some difficulty. Eventually the problem was solved by inserting a switch in the divider chain at the point where normally a  $625\mu\text{S}$  'd' type waveform would be, and allowing a  $625\mu\text{S}$  'b' type waveform, a  $25\mu\text{S}$  'd' type waveform, or the  $1\mu\text{S}$  waveform to be used. This gives clock rates of

x1, x2, x25, and x625 which can be used to advance the clock; 24 hours being covered in just over two minutes. The electro-mechanical clock is connected when the times shown by the divider chain and the clock agree, and they are then advanced together to the correct GMT. It is found that the electromechanical clock can keep in step at x25 speed but not at x625 so it is convenient if it shows a time a few minutes earlier than the actual time before setting up begins. The speed selecting switch is placed at the 625  $\mu$ S point in the divider chain to minimize the effect on the divider time of contact bounce in the speed selector switch. If placed at the 1 second point, ten rapid bounces as the speed selector was returned to its normal position, would produce an erroneous 10 second jump in time. At the 625  $\mu$ S point 10 such bounces would only change the time by 1/160 seconds, much less than the error in setting up the time.

We will now consider how the echo sounding, calibration, and annotation are ordered.

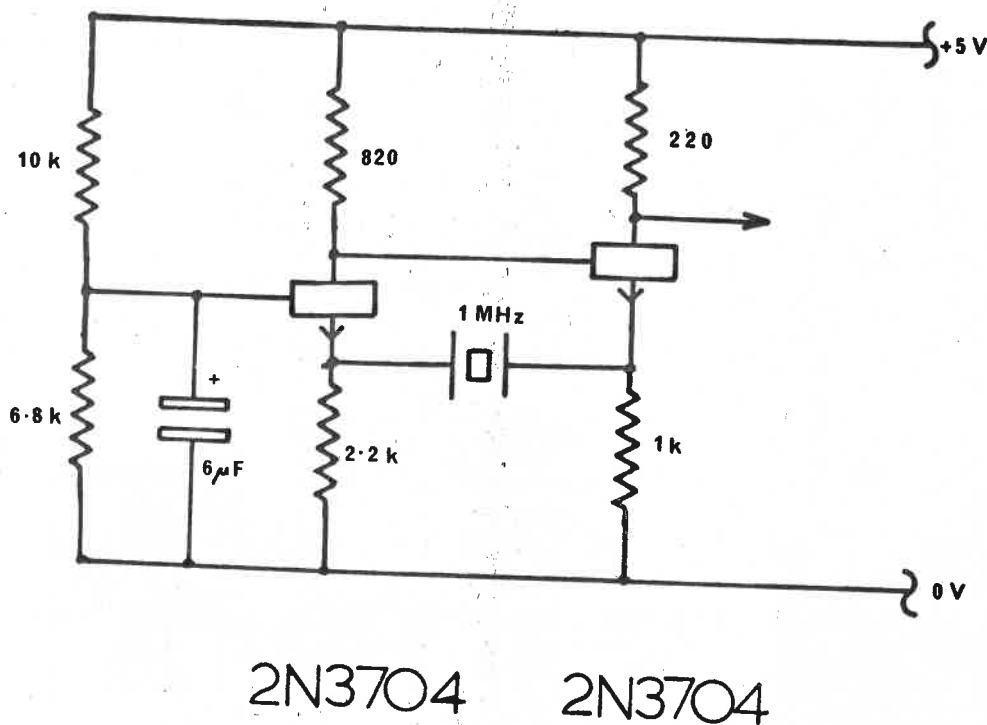


Figure 2.2.1

The schematic diagram of the emitter-coupled quartz crystal oscillator which is the time reference and source of all pulses in the timing circuits.



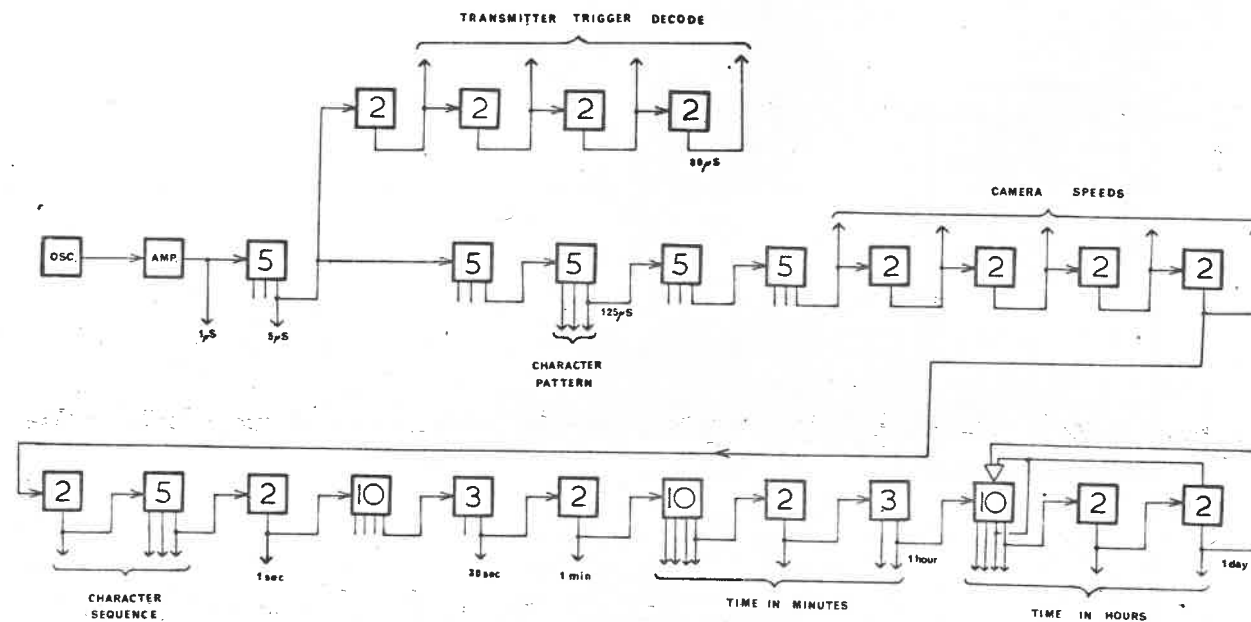
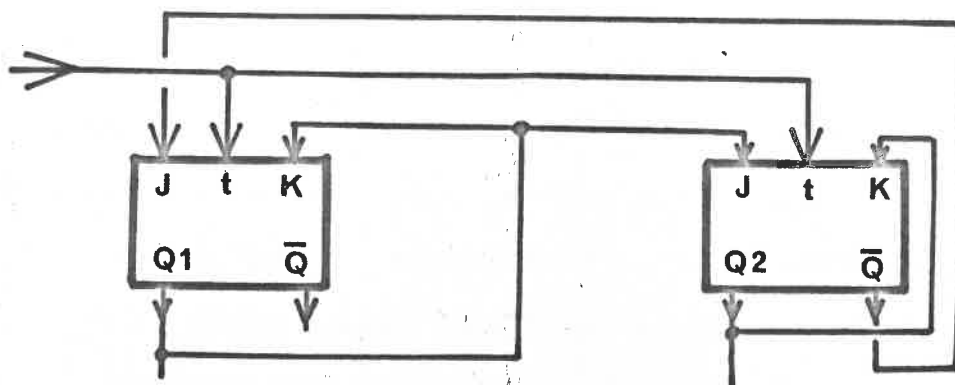


Figure 2.2.2

The block diagram of the main divider chain which counts the  $1\mu S$  pulses from the crystal oscillator down to a waveform having a period of 1 day.



Truth table of one  
J-K flip-flop

J	K	Q' (Q=0)	Q' (Q=1)
0	0	0	1
0	1	0	0
1	0	1	1
1	1	1	0

Truth table of  
combination

Q2	Q1
0	0
0	1
1	0
0	0
etc.	

Figure 2.2.3

Showing division by 3 using a pair of J-K flip-flops. The truth table for a J-K flip-flop shows the state of output Q after a negative clock edge for all combinations of J and K. The truth table of the combination shows the count of 3 with Q2 the most significant bit. The circuit escapes from  $Q1 = Q2 = 1$ .

### 2.3 Sequencing of events

As we saw in the first section the chosen operating sequence is: 0.5 seconds calibration; 0.5 seconds annotation; and 59 seconds sounding. On figure 2.1.3 the 1 minute waveform, which has unity mark-space ratio, is shown as the clock input to a flip-flop marked 'CAL'. This flip-flop may be called the 'calibrate latch'. At the instant the minute waveform goes from a '1' to a '0' this latch is 'set'. This corresponds to the start of a minute. The Q output of the calibrate latch feeds the 'calpip' generator and the RENA circuit. The latter will be described in more detail later. The calpip generator is a gated monostable which produces short pulses ( $\approx 0.1 \mu\text{S}$ ) every  $1 \mu\text{S}$ , or every  $5 \mu\text{S}$  if more widely spaced calpips are required. The input from the crystal oscillator may be switched to the  $5 \mu\text{S}$  signal by means of a front panel switch but this is not shown on the block diagram in the interests of clarity. The calpip generator is inhibited when the Q output of the calibrate latch is a '0', but after the commencement of a minute the calibrate latch is set, and calpips are produced.

The  $\bar{Q}$  output of the calibrate latch gates the trigger to the transmitter so that as long as the calibrate latch is set, triggering does not occur. The Q output of the calibrate latch is also the clock input to a second flip-flop, marked 'CHAR', which we will call the 'character latch'. Not shown on the block diagram is the

reset input to the calibrate latch. This is the 1 second waveform which, it may be remembered, is a square wave having unity mark-space ratio and a period of 1 second. Consequently it is a '0' for the first half second of each second, and a '1' for the next. At the start of each minute, the reset pulse is '0', and the latch can be set. After 0.5 seconds the reset pulse becomes '1' and the latch is reset, i.e. calibration ceases. As the calibrate latch goes to a '0' it sets the 'character latch'.

The character latch enables the input to the character generator and consequently, during the period following the reset of the calibrate latch, characters arrive at the mixing circuits. In addition, the  $\bar{Q}$  output of this latch gates the transmitter and sweep trigger. The character latch is reset by the 1 second waveform (not shown on figure 2.1.3), but it is inverted, so that it is a '0' for the second half second of the minute, and rises to a '1' at the end of the first second. Thus the character latch is reset 0.5 seconds after it is set. Thereafter both of these latches remain unset until the start of the next minute.

In the absence of either the calibrate or the character latch, the transmitter trigger is enabled. This trigger is obtained by an AND function operating on the 10, 20, 40, and 80  $\mu$ S pulses which are derived in the main divider chain. Figure 2.3.1 shows these four waveforms and also shows the waveform obtained by certain AND operations. It may be seen that the result of the

operation (10) & (20) & (40) & (80) is a  $5\mu\text{S}$  wide positive going pulse. In order to achieve an advance of the transmitter trigger relative to the sweep trigger, the transmitter is triggered by the positive edge, while the sweep is triggered by the negative edge. In this way, the transmitter pulse is triggered  $5\mu\text{S}$  before the sweep. In fact, the sweep starts almost immediately it is triggered, while the transmitter pulse can be delayed a few microseconds after its trigger. This short delay is adjusted so that the transmitter pulse has just decayed as the sweep starts. There is a 'sweep latch' which is set by the trigger to start the sweep and this enables the ramp generator, so that the linear sweep begins. The latch also enables the receiver, which therefore comes on during the sweep. A voltage trip senses the linear ramp, and when it reaches a voltage which corresponds to the end of the oscilloscope screen, the sweep latch is reset and the receiver is therefore muted. At this point flyback occurs. A switch on the front panel allows the  $80\mu\text{S}$  input to the trigger decode to be disconnected so that the function becomes (10) & (20) & (40). On figure 2.3.1 this may be seen to be identical to the previous case, but the p.r.f. is now  $40\mu\text{S}$  instead of  $80\mu\text{S}$ ; we have therefore a means of doubling the p.r.f.. In addition a front panel switch allows the  $10\mu\text{S}$ , or the 10 and the  $20\mu\text{S}$ , or the 10, 20 and  $40\mu\text{S}$  inputs to the trigger decode to be disconnected. The function then becomes (20) & (40) & (80); (40) & (80); and

(80) respectively. It may be seen on figure 2.3.1 that this does not affect the instant at which the sweep is triggered (the negative edge), but it causes the transmitter pulse (the positive edge) to occur  $5\ \mu\text{S}$ ,  $15\ \mu\text{S}$ , and  $35\ \mu\text{S}$  respectively before the usual time. We have therefore devised a system whereby the p.r.f. may be changed, and also the transmitter pulse may be advanced by a 'crystal-controlled' time interval. Field use of the equipment has shown that a desirable modification to this part of the circuit would allow an even lower triggering rate, say  $150\ \mu\text{S}$ , for use in high flying aircraft. In addition, a transmitter advance in equal steps of  $5\ \mu\text{S}$  up to perhaps  $40\ \mu\text{S}$  would be preferable to the existing method.

The ramp generator is a bootstrap circuit, with an emitter follower to avoid loading and consequent loss of linearity. A linearity of better than 1% was the intention of the design, but this may be degraded very slightly by the mixing circuitry which is necessary to combine the linear sweep and the character generating waveforms. The 'character latch' inhibits the transmitter trigger, but does not inhibit the sweep, so that the same linear sweep is operating while the 'calpips' are being displayed.

A 'range-zero' button is also provided on the front panel, to allow the precise instant of the transmitter pulse to be deduced. This is achieved by inverting the sense of the trigger to the

transmitter. The transmitter is then actuated by the same edge as the sweep and, since there is a delay before the transmitter pulse occurs, the transmitter pulse is always visible on the trace in this condition. If the position of the transmitter pulse is then noted, it is known that in the normal running mode it occurs exactly  $5\mu$  S before that (or 10, 20 or  $40\mu$  S in the case of the alternative transmitter advances).

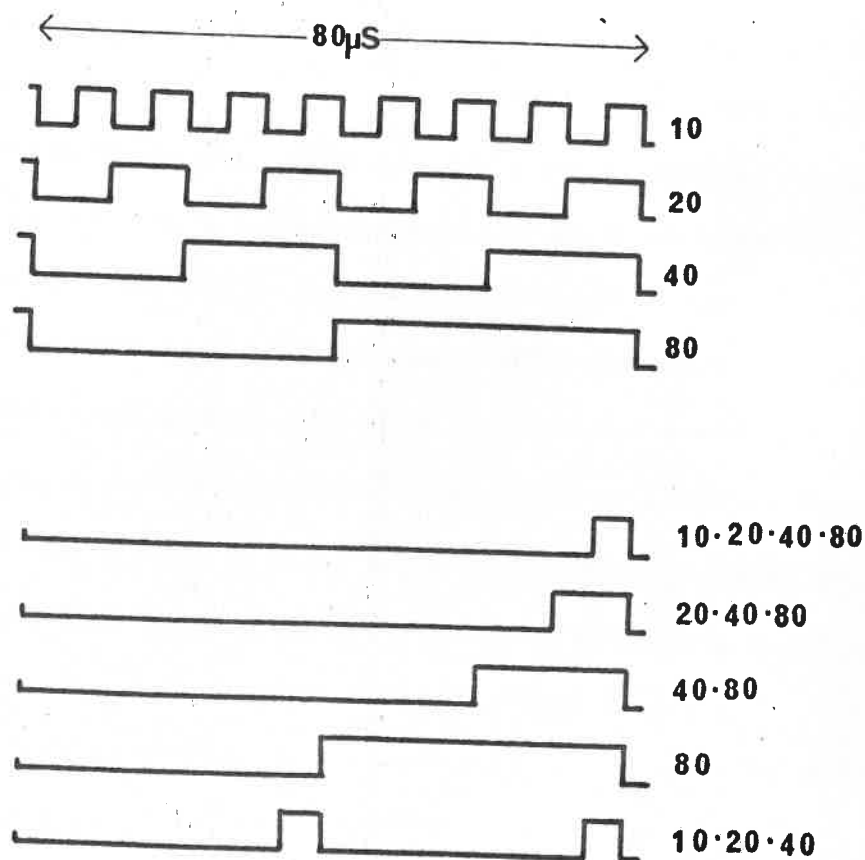


Figure 2.3.1

Showing the four waveforms from which the transmitter trigger is decoded. Below, five possible combinations of decoding are shown to give a selection of transmitter advances and an alternative pulse repetition rate.



## 2.4 Character generation

The object of the character generator is to produce numeric figures on the screens of the recording and monitoring oscilloscopes. It was decided to produce these figures using a matrix of dots on the screen, which are selectively intensified. It was hoped to use a Read-Only-Memory (ROM) which was about to become commercially available, and which would provide the necessary bits given the code value (in this case ASCII code) of the character. This device would have allowed us to use a 5 x 8 matrix to produce the figures, but unfortunately delivery of this product was delayed and we were obliged to build a read-only-memory using diodes. For simplicity the size of the matrix was reduced to 3 x 5 and the designs for the figures are shown in figure 2.4.1.

The first problem we will consider is the ordering of the characters for decoding and display. As we have seen there are ten decimal figures which are present as ten BCD words. The time in hours and minutes, four BCD words, come from the main divider chain. The receiver attenuator settings, two BCD words, come from encoding rotary switches which are fixed to the rear of the attenuators. Unfortunately there are 12 positions on the attenuators which are used, 0-11 dB and 0-110 dB. The encoding must therefore contain some ambiguity. It was decided to make 11=10=9 dB in the case of the units of dB, since an error of 2 dB would not be serious and these values would normally be avoided,

and in the case of the tens of dB, we made  $110 = 10$ , and  $100 = 0$ , since an ambiguity of 100 dB should be obvious from the appearance of the radio echo record obtained. The single digit (one BCD word) which describes the transmitter advance and the calpip setting was wired to the control switches, so that the two least-significant bits were controlled by the four possible settings of the transmitter advance, and the next most significant bit was connected to the 1 or  $5\ \mu\text{S}$  calpip switch. The digit is therefore interpreted according to the following:

Calpips at:				
$1\ \mu\text{S}$	$5\ \mu\text{S}$		Transmitter triggered	
0	4	$5\ \mu\text{S}$	}	before the sweep
1	5	$10\ \mu\text{S}$		
2	6	$20\ \mu\text{S}$		
3	7	$40\ \mu\text{S}$		

The three digits from the RENA function were available as three parallel BCD words. The BCD count which is found in the main divider chain (figure 2.2.2) having a period of 0.5 seconds, is decoded to give ten signals which are '1's, sequentially for 0.05 seconds each. These ten signals are used to gate the ten input words which represent the numbers to be displayed. These

are then OR'd to give one parallel BCD word (the 'OR-word') which has the value of each input for 0.05 seconds once every half second. We now have a single BCD word (the 'OR-word') which represents all the BCD input words serially during the half second of character display.

Individual characters are formed using the count-of-5 available from the main divider chain at a period of  $125 \mu\text{S}$ . The most significant bit of this count is divided by a further factor of three to give the horizontal movement of the dot matrix. These bits are then used in a digital-analogue converter to produce X and Y deflections. The waveforms are illustrated in figure in 2.4.2, the total scan taking  $375 \mu\text{S}$ . In addition the digital-analogue converter is fed with the BCD count of period 0.5 seconds so that ten successive  $5 \times 3$  matrices are painted, synchronously with the scanning of the ten input BCD words. The diode read-only-memory decodes each of the 15 matrix points for each one has a selection of possible decimal characters for which that particular point must be intensified according to figure 2.4.1. The decimal characters are obtained by decoding the BCD 'OR-word' which carries the information about each digit sequentially.

The effect of this process is that during the 0.5 seconds for which characters are displayed, each number is decoded for 0.05 seconds and a  $3 \times 5$  matrix of dots intensified in the

appropriate pattern. At the end of each 0.05 seconds the matrix of dots is moved by the digital-analogue converter to an adjacent position and the next number in the series is decoded. In this way all ten numbers are painted. Notice that each character is scanned once every  $375 \mu\text{S}$ , that is to say 133 times during its 0.05 seconds of decoding. An alternative method of painting the characters would be to scan the entire ten words in  $3750 \mu\text{S}$  and maintain this display for 0.5 seconds. This method was rejected because the recorder film is continually moving and it was realised that if all ten words were displayed for 0.5 seconds, the film movement would probably blur the characters. The chosen method completely paints one character in 0.05 seconds and then proceeds to the next, so that the amount of blurring is reduced by a factor of ten.

The X, Y, and Z waveforms must be mixed with the outputs from the calpip generator and the receiver. This is achieved by an operation which might be called 'linear OR'. During non-operating periods the unwanted signals are made to be at zero potential while the wanted signal follows the desired positive excursions. By using a circuit analogous to a diode OR gate, the output can be made to follow whichever input has the highest potential. There are two mixing circuits, although only one is shown on figure 2.1.3; one is for the monitor oscilloscope, and one for the recorder oscilloscope. They are separate because the received

signal must Z-modulate the recorder, but Y-deflect the monitor, and the characters must appear horizontally on the monitor (to be read) and vertically on the recorder, so that they appear above the radio echo record. Figure 2.4.3 shows the full picture during one second of calibration and annotation on the monitor (above) and recorder (below). By suitable adjustment of the levels in the digital-analogue converter, a pleasing layout on the film record can be achieved (figure 2.4.4).

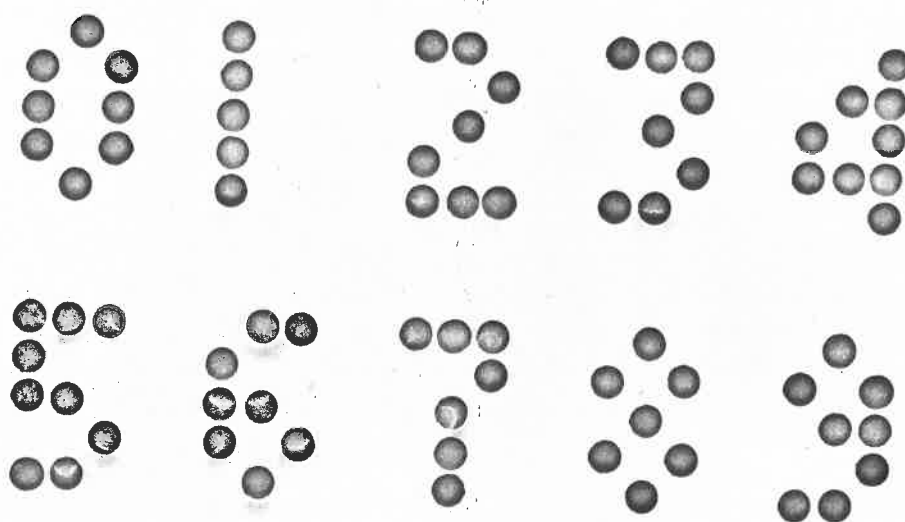


Figure 2.4.1

The representation of decimal figures using a matrix of 5 by 3 dots.

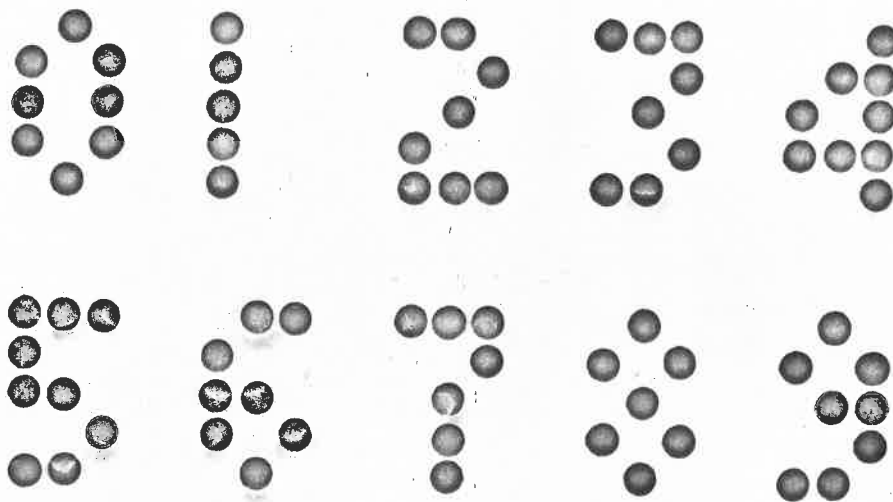


Figure 2.4.1

The representation of decimal figures using a matrix of 5 by 3 dots.

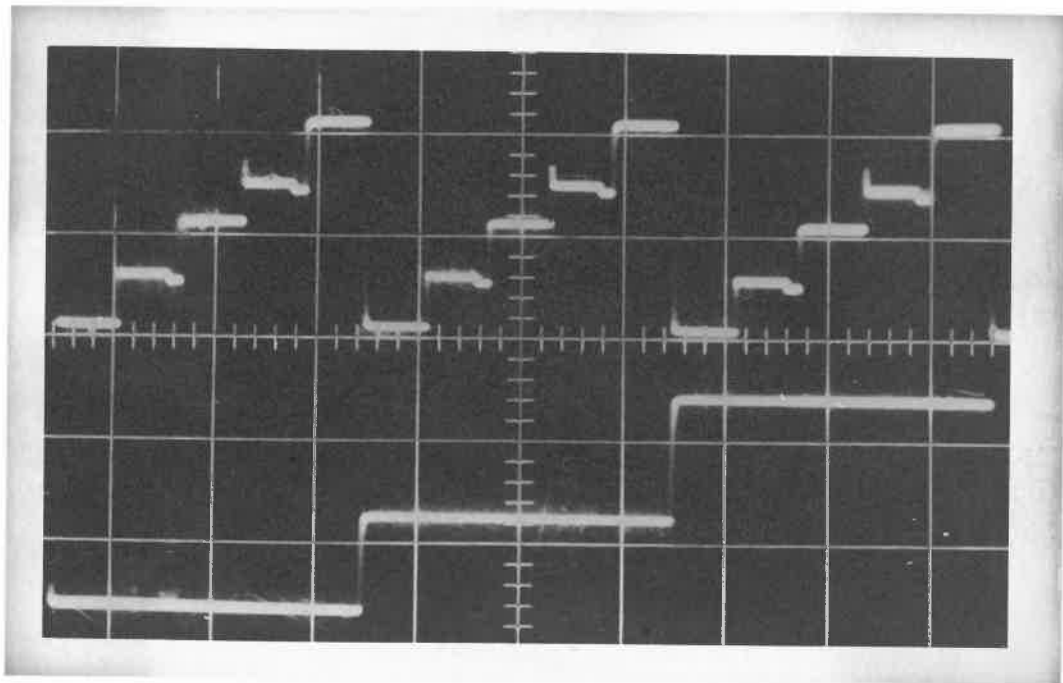


Figure 2.4.2

An oscillogram of the deflection waveforms used to produce a 3 x 5 dot matrix on a cathode ray tube. The upper trace is the Y deflection, the lower trace is the X deflection.



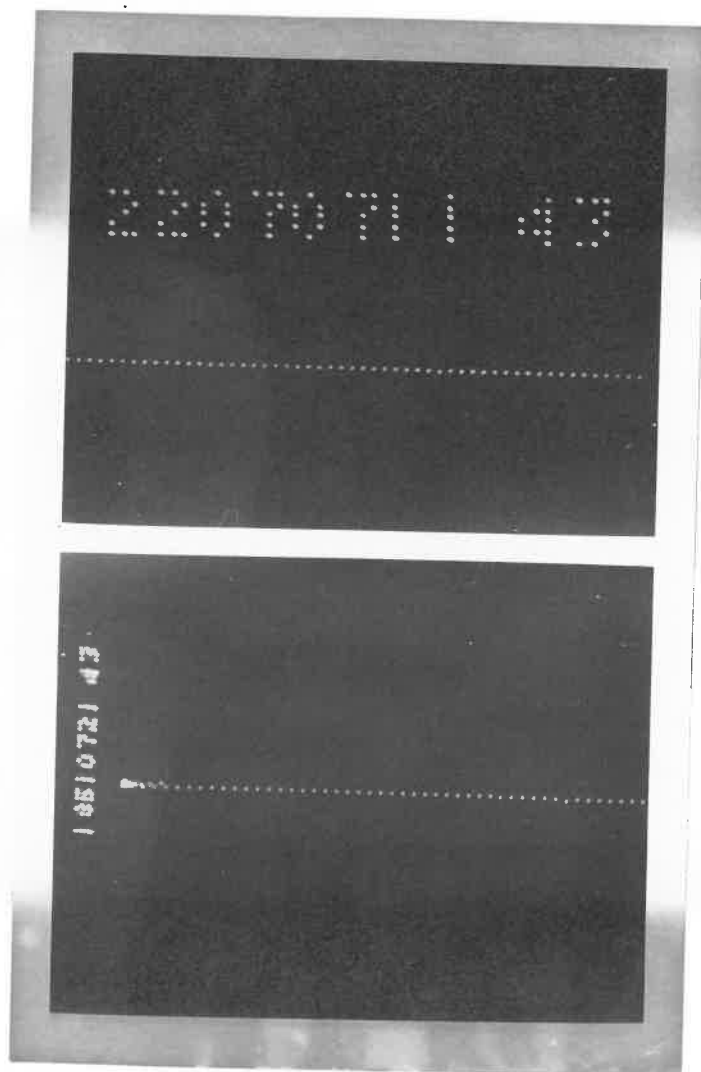


Figure 2.4.3

Photographs of the monitor (above) and recorder (below) oscilloscope screens showing the positions of the character annotation and the calibration marks.

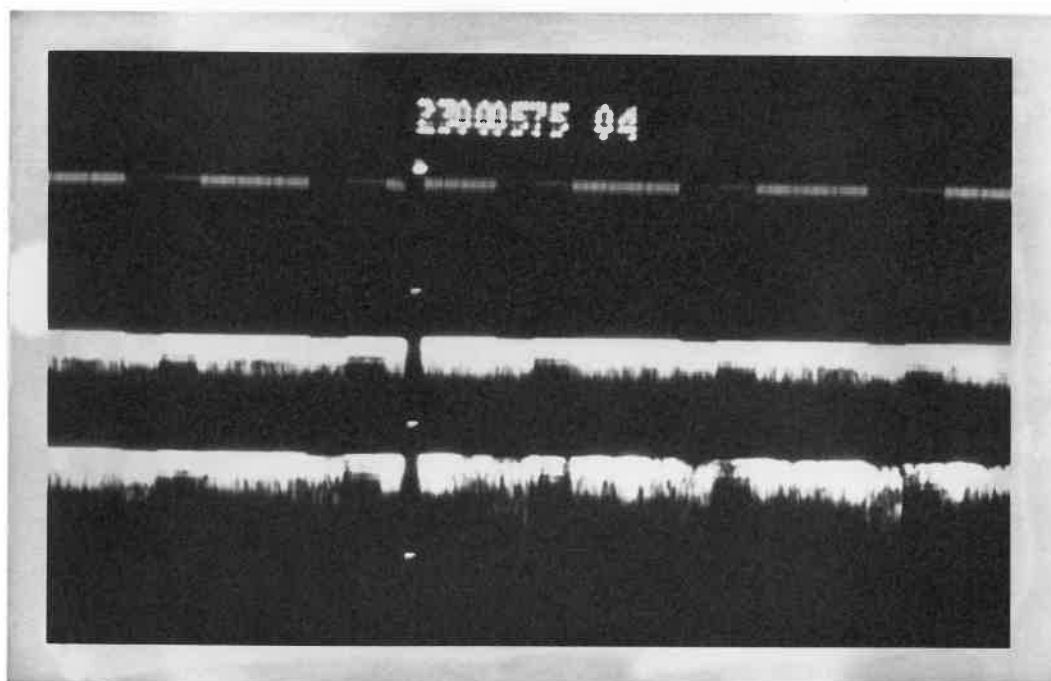


Figure 2.4.4

Part of a radio echo record showing strong surface and bottom echoes. The calibration marks are the four dots in a vertical line which interrupt the echoes. The numeric annotation indicates the following : time, 2300; attenuation, 05; transmitter code, 7; date code, 5 04.

## 2.5 Output facilities

The film transport mechanism in the recording camera of the Mark 4 echo sounder is driven by a Mullard AU 5056 stepping motor. The waveforms required in the two sets of motor windings are shown in figure 2.5.1. This waveform is obtained by a 'gray-code' counter also shown in figure 2.5.1 (see figure 2.2.3 for details of each J-K flip flop). For each change of state of the waveforms, the motor shaft turns  $7\frac{1}{2}^\circ$ . With a reduction gear of 50:1 and a film drive wheel having 12 sprockets, this means that 200 input pulses to the gray-code counter, advance the 35 mm recording film by one sprocket. With such small increments the movement may be considered to be continuous. The pulse repetition frequency of the drive pulses is selected by means of a front panel switch from the waveforms in the main divider chain (figure 2.2.2). Frequencies from 5 to 320 Hz were used, in steps of one octave. These frequencies correspond to film speeds of 1.6 to 96 sprockets per minute (approximately 8 to 480 mm per minute). The highest speed, 320 Hz, is the maximum speed at which the stepping motor is reliable. Above this speed the inductance of the motor windings reduces the mean current to a level which is too low for operation. The output from the gray-code counter is at logic levels and a current driver is necessary to feed the motor windings. The driver circuits are able to operate two separate cameras in parallel. The current drawn by a single camera from the 24 volt power line

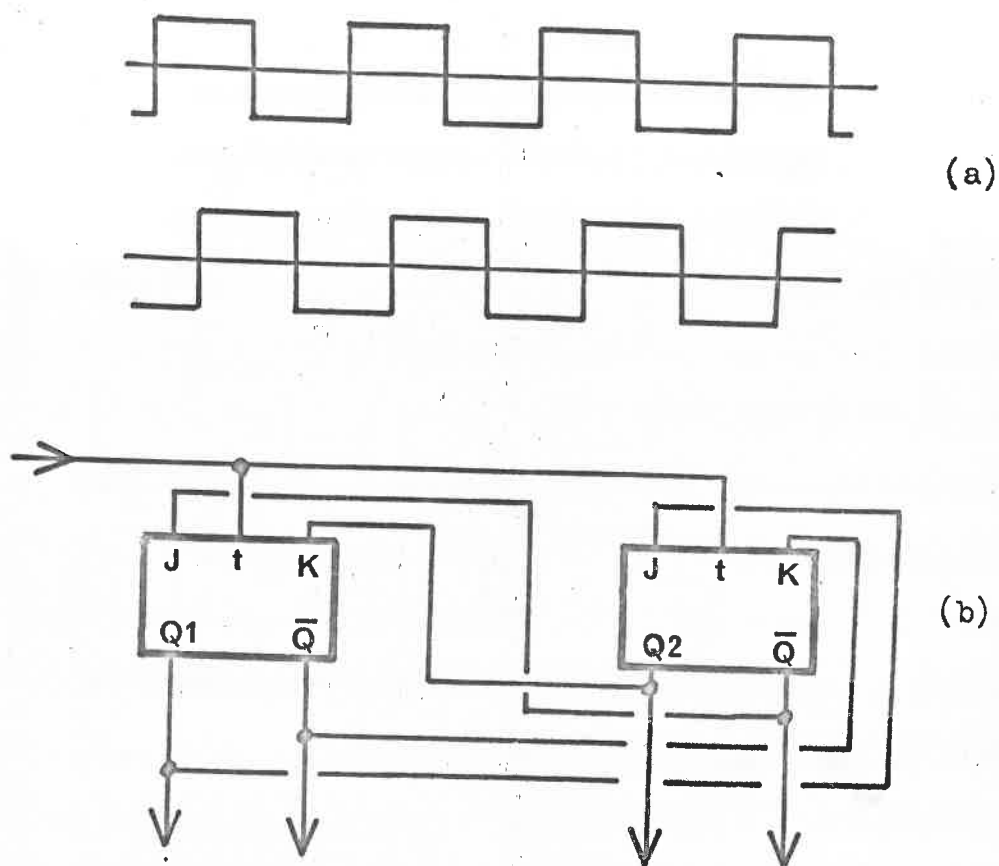
is 280 mA at 5 Hz and 100 mA at 320 Hz.

The electromechanical clock, which was used by the aircraft navigator to time his observations, is driven from the 1 second square waveform in the divider chain. A current driver, similar to that for the camera stepping motor, provides the necessary reversing current in the clock escapement winding.

A bicycle wheel with an odometer is often towed behind a sledge during surface traverses, to allow the distance covered to be estimated. Since the speed of travel is usually very variable, the horizontal scale on a radio echo film record driven at a constant speed would be difficult to interpret. A solution to this problem is to use a 'Dynohub' bicycle wheel which gives an AC output of a few volts, at a frequency proportional to the speed of rotation. An amplifier is incorporated in the timing module which produces a logic-compatible square wave, from the AC output of the 'Dynohub'. There are 10 pulses per rotation of the wheel, and the circuit is sufficiently sensitive to operate at travelling speeds down to 350 metres per hour. The pulses are used to drive the camera circuits as an alternative to the pulses from the divider chain. The scale of distance along the film is fixed by the circumference of the wheel ( $=2\pi m$ ) so that 1 km on the ground represents 125 mm on the film.

Although the author's use of the Mark 4 radio echo sounder has been restricted to light aircraft, it has also been used in

C 130 Hercules. This aircraft was equipped with two radio echo aeralis, so that by changing their relative phases, the direction of the main lobe of the beam could be altered. Figure 2.5.2 shows how the 'b' and 'c' outputs of a BCD counter driven from the 1 second waveform were used to direct the beam to the left for 2 seconds, to the right for 2 seconds, and vertically downwards for 6 seconds, using relays in a phase shift network (not shown). The records obtained using this feature, permitted the direction of a reflector to be deduced.

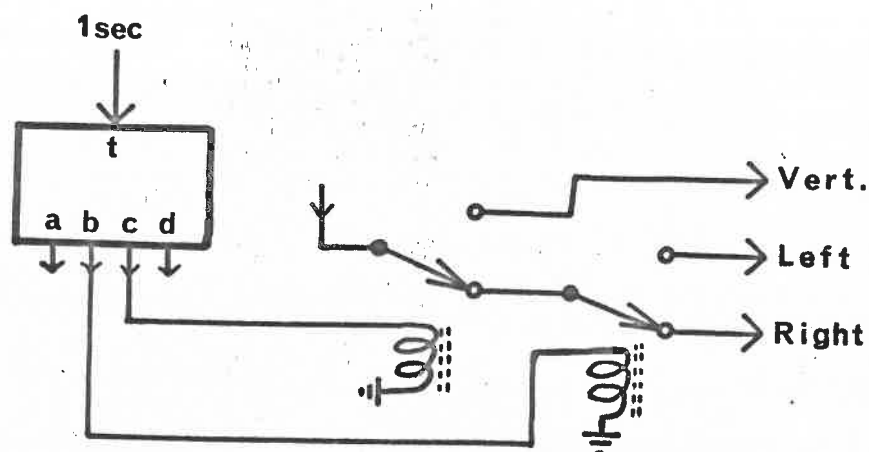


Truth table	
Q1	Q2
0	0
1	0
1	1
0	1
0	0
etc.	

Figure 2.5.1

a). The waveforms required in the two windings of the camera stepping motor.

b). Two J-K flip-flops wired to produce the waveform required by the camera stepping motor.



Truth table

(d)	c	b	(a)
0	0	0	x
0	0	1	x
0	1	0	x
0	1	1	x
1	0	0	x
0	0	0	x
etc.			

Figure 2.5.2

Showing the use of a BCD counter to direct the aerial to the left for two seconds, to the right for two seconds, and vertically for six seconds. In the truth table, the 'a' output counts 0, 1 (two seconds) where an x is shown.

## 2.6 Radio echo navigational aid

The radio echo navigational aid (RENA) was devised by the author to provide primitive navigational information for use when airborne sounding. It was stimulated by the fact that at least two complete radio echo sounders are usually taken on an expedition as a safeguard against failure. RENA is an attempt to use the spare equipment as a navigational beacon. The facility is intended to provide a one-range measurement which would fix the aircraft's position to an accuracy of 150 m, on a circle round the beacon.

Measurement of the transit time of radio wave to the beacon and back to the aircraft, is made once per minute. The timing module in the equipment used as a beacon, is removed, and is replaced with a single 'transponder control' circuit. This circuit monitors the output of the beacon receiver, is able to mute the receiver, and is able to trigger the beacon transmitter. The method of operation is as follows: A ramp generator in the transponder control circuit is reset whenever a pulse is received. Normally this occurs every 40 or 80  $\mu$  S, as the pulses are transmitted by the airborne sounder. When the period of calibration begins, the transmitted pulse ceases, so that the transponder ramp is permitted to reach a threshold which corresponds to an elapsed time of 100  $\mu$  S since the last received transmitter pulse. At this threshold a flip-flop is set. The flip-flop mutes the receiver, and initiates the beacon transmitter so that a pulse is



sent in reply to the silence of the airborne installation. 100  $\mu$  S after this reply (sufficient time for local echoes to subside), the receiver is turned on again in preparation for the next series of pulses from the airborne sounder. The circuit is designed so that no further response will be initiated by the beacon until a signal is received from the airborne equipment. This prevents the beacon from replying continuously to the lack of signals when the airborne equipment goes out of range. Meanwhile, in the airborne sounder, when 100  $\mu$  S has elapsed since calibration began (i. e., since transmission ceased), a counter starts to count 1  $\mu$  S pulses from the crystal. At the same time the airborne receiver is returned to its on state. As soon as a reply pulse is received, the counting is stopped and the receiver is muted. At this stage, the number of microseconds counted is equal to the distance of the beacon in units of 150 m. Figure 2.6.1 shows a block diagram of the circuitry in the airborne sounder which controls the counting. The flip-flop labelled A is set by the negative edge of the minute waveform, that is at the commencement of calibration. The Q output of this flip-flop resets the three BCD counters to zero, and enables a 'd' waveform having a period of 125  $\mu$  S. This forms the clock input to the flip-flop marked B. The 125  $\mu$  S 'd' type waveform goes from a '0' to a '1' after 100  $\mu$  S and consequently the output of the inverting gate goes to zero 100  $\mu$  S after calibration begins.

This sets the B flip-flop which then clears flip-flop A and brings on the receiver and the  $1\ \mu\text{S}$  pulses are permitted to enter the counting network. The receiver is muted until  $100\ \mu\text{S}$  have elapsed since the last transmitter pulse. This delay ensures that local echoes will not be interpreted as beacon replies. When a reply pulse is received, flip-flop B is reset and counting stops. No further action is possible until the next minute. The whole process has occurred before the 0.5 seconds of calibration has ended, so that when the character generator examines the outputs of the three BCD counters, it displays the range of the beacon which was measured a fraction of a second before. The counters have a wrap-around ambiguity of 1000 units so that the range measurement has an ambiguity of 150 km. This would normally be easily resolved. The maximum range of operation depends on the system performance, and upon the path between the airborne sounder and the beacon. In free space a system performance of 160 dB and isotropic aerials would permit a maximum range of more than  $10^4$  km. In practice the aerial used by the beacon and the aircraft probably have adverse gain in the required direction and the path may not be line of sight. In addition the attenuators of the airborne receiver will attenuate the received pulse from the beacon. This is rather unsatisfactory but the alternative of using solenoid operated attenuators which were set to 0 dB for the period of measurement could not be implemented. One advantage of attenuation

in the airborne receiver is that the reply pulse is lost by the airborne receiver before the beacon loses the aircraft's signals, so that spurious responses from the beacon should not cause interference to normal sounding. RENA worked well in the laboratory using a pulse generator to produce a delayed reply to the 'minute' event, but when the author set up a beacon in the field, using the spare radio echo sounder, no measurements of distance were successfully made. The reason was later found to be a fault in the transmitter design which caused it to transmit a continuous low level signal if it was not triggered in the normal way for more than about 100  $\mu$  S. This meant that both the airborne receiver and the beacon receiver were alerted by local transmission, and the correct transmissions were ignored. An alternative circuit card was carried which could be wired up to present any three BCD words to the character generator and after the failure of RENA, this was used to annotate the film with a date code, the three digits representing the month and the day-of-the-month.

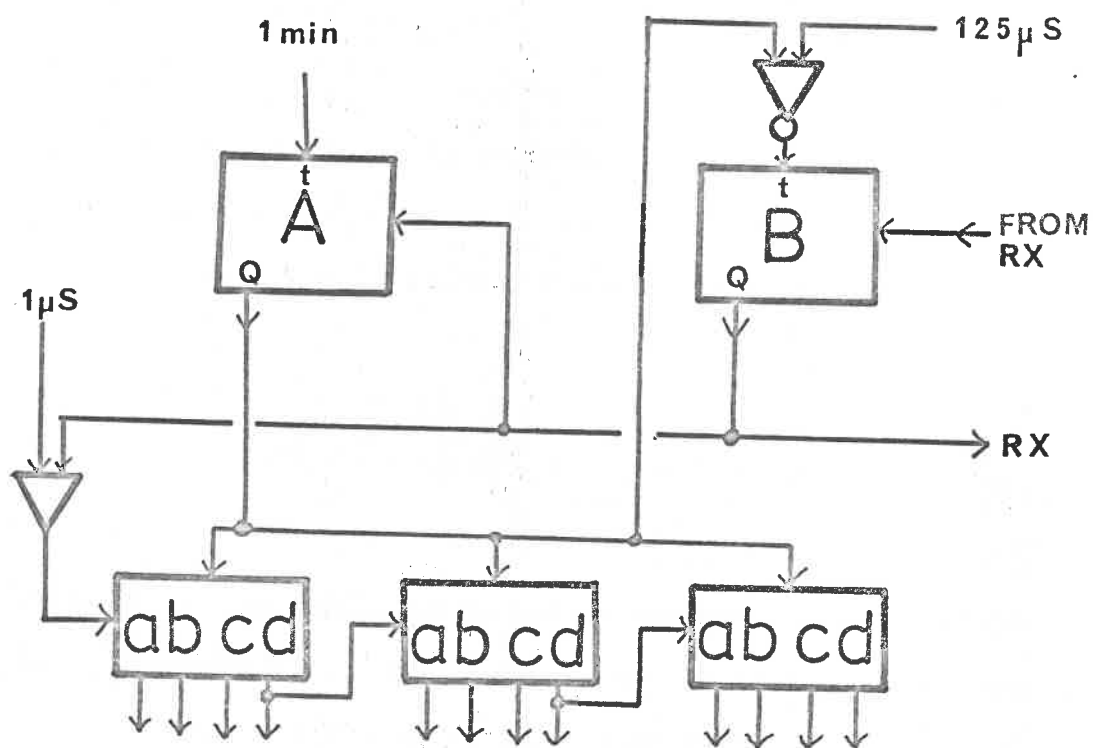


Figure 2.6.1

A block diagram of the RENA circuit in the airborne radio echo sounder. Counting of the  $1\mu\text{S}$  pulses by the three BCD counters, begins  $100\mu\text{S}$  after the negative edge of the minute waveform and ends when a reply is received.

## CHAPTER 3

Factors affecting the strength of the received signal3.1 General considerations and geometrical effects

We have already considered the transmitter power,  $P_t$ , the receiver sensitivity,  $P_r$ , and the aerial gain,  $G$ , which can be achieved. In our case the receiver aerial will either be the same as the transmitter aerial, or it will be an identical aerial, and we may define its cross sectional area in reception as:

$$A = \frac{G \lambda^2}{4\pi} \quad (1)$$

where  $\lambda$  is the wavelength in the medium containing the aerial.

We will characterize a medium of propagation by its conductivity  $\sigma$ , its permittivity  $\epsilon$ , and its permeability  $\mu$ . The relative permeability of all media which we will consider is unity and therefore  $\mu = 4\pi 10^{-7}$  henries  $m^{-1}$ . At some distance  $r$  from a transmitting aerial, a spherical wave will propagate with an electric vector:

$$\mathcal{E} = \mathcal{E}_0 \frac{1}{r} \exp(j\omega t - \gamma r) \quad (2)$$

where  $\omega$  is the angular frequency,  $t$  is the time,  $\gamma$  is the

propagation constant, and  $\mathcal{E}_0$  is defined by the transmitter power and aerial gain thus:

$$\mathcal{E}_0 = \sqrt{\frac{P_t G}{2\pi R_e(1/\eta)}} \quad (3)$$

where  $R_e(1/\eta)$  is the intrinsic conductance; the intrinsic impedance  $\eta$ , of the medium of propagation being defined as:

$$\eta = \sqrt{\frac{\mu}{\epsilon(1 + \sigma/j\omega\epsilon)}} \quad (4)$$

The propagation constant  $\gamma$  is usually written:  $\gamma = \alpha + j\beta$  where:

$$\alpha = \omega \sqrt{\frac{\mu\epsilon}{2} \left( \sqrt{1 + \frac{\sigma^2}{\omega^2\epsilon^2}} - 1 \right)}$$

$$\beta = \omega \sqrt{\frac{\mu\epsilon}{2} \left( \sqrt{1 + \frac{\sigma^2}{\omega^2\epsilon^2}} + 1 \right)}$$

(5)

Note that the amplitude falls as  $\exp(-\alpha r)$ , and therefore  $\alpha$  is known as the attenuation constant; attenuation in the medium being  $8.68 \alpha$  dB  $\text{m}^{-1}$ . The wavelength is defined by  $\lambda = 2\pi/\beta$ .

The mean power per unit area in a wave having an electric vector with magnitude  $E$ , is given by:

$$\overline{P} = \frac{E^2}{2} R_e(\frac{1}{\eta}) \quad (6)$$

And the power received by our aerial of cross section  $A$  is:

$$P_r = A \frac{E_0^2}{2} R_e(\frac{1}{\eta}) \quad \text{or, using equation (1)} \quad P_r = \frac{G\lambda^2}{8\pi} E_0^2 R_e(\frac{1}{\eta}) \quad (7)$$

If we now consider a medium having negligible conductivity, e.g. air, then equation (2) becomes:

$$E_0 = \sqrt{\frac{P_t G}{2\pi \sqrt{\epsilon/\mu}}} \frac{1}{r} \exp[j\omega(t - \sqrt{\mu\epsilon} r)] \quad (8)$$

and equation (7) becomes:

$$P_r = \frac{G\lambda^2}{8\pi} E_0^2 \sqrt{\epsilon/\mu} \quad (9)$$

Let us imagine a specular reflection from a surface at a distance  $R$ ,

in air, having an amplitude reflection coefficient of  $\rho$ . The incident wave at the reflector has amplitude:

$$\sqrt{\frac{P_t G}{2\pi \sqrt{\frac{\epsilon}{\mu}}}} \frac{1}{R} \quad (10)$$

and the echo received at an aerial close to the transmitting aerial has amplitude:

$$\rho \sqrt{\frac{P_t G}{2\pi \sqrt{\frac{\epsilon}{\mu}}}} \frac{1}{2R} \quad (11)$$

Using equation (8), the received power is:

$$P_r = P_t \left( \frac{G \lambda \rho}{8\pi R} \right)^2 \quad (12)$$

The echo will only be detected if this power is greater than the receiver sensitivity.

If the reflecting surface is water then  $\rho$  is approximately unity and equation (12) allows the aerial gain of an airborne radio echo sounder to be calculated from the ratio of transmitted power to received power on reflection from a calm sea. The technique may also be applied to the measurement of the aerial polar diagram, by banking the aircraft. Measurement in the pitching plane is not



usually possible.

We will now consider the echo strength for a path of propagation which is partly in air and partly in ice, as shown in figure 3.1.1. The reflection from the surface of the ice is formally the same as the reflection from a calm sea. However, the reflection from the bottom of the ice is, in addition, subject to refraction. For the moment we will neglect absorption in the ice and attenuation by reflection at the air/ice interface. Since ice is optically denser than air, the wave front diverges more slowly in ice than in air, having been refracted at the air/ice interface. The effect of this is the modification of the inverse square law. Instead of  $(h + d)$  in figure 3.1.1, the apparent range of the bottom is  $(h + d/\sqrt{\epsilon})$ . Note that the refractive index of the medium is  $\sqrt{\epsilon}$ , where  $\epsilon$  is the relative permittivity. Substituting this figure into equation (12) the received power is increased by a factor equal to:

$$\left( \frac{h + d}{h + d/\sqrt{\epsilon}} \right)^2 \quad (13)$$

If  $h$  is much greater than  $d$  this factor is unity, but if  $h$  is small compared to  $d$  then the factor tends to  $\epsilon$ . Since ice has a relative permittivity of about 3.2 this means that the received echo is 5 dB stronger than it would be without the effect

of refraction. Robin, Evans and Bailey (1969 p 455) have derived this result but make the comment that ray optics does not apply to the situation where  $h$  is less than a wavelength. When the aerial is embedded in the ice, it is the area of the aerial, rather than the gain, that remains the same, so that in equation (12) we replace  $G$  with  $4\pi A/\lambda^2$  from equation (1). Then with the range  $R$  equal to  $d$  (neglecting the proximity of the boundary) and remembering that  $\lambda$  is reduced by the factor  $1/\epsilon$ , the received power is again 5 dB stronger than it would be without the effect of permittivity. There is therefore no difference between an aerial which is just above the ice surface and one just below it, provided that ray optics applies.

Having disposed of the geometrical effects of the spherical wave front, we will now assume that the waves are plane for the purpose of evaluating the reflection coefficients and attenuations. A plane wave propagates with electric vector:

$$\mathcal{E} = \mathcal{E}_0 \exp(j\omega t - \gamma x) \quad (14)$$

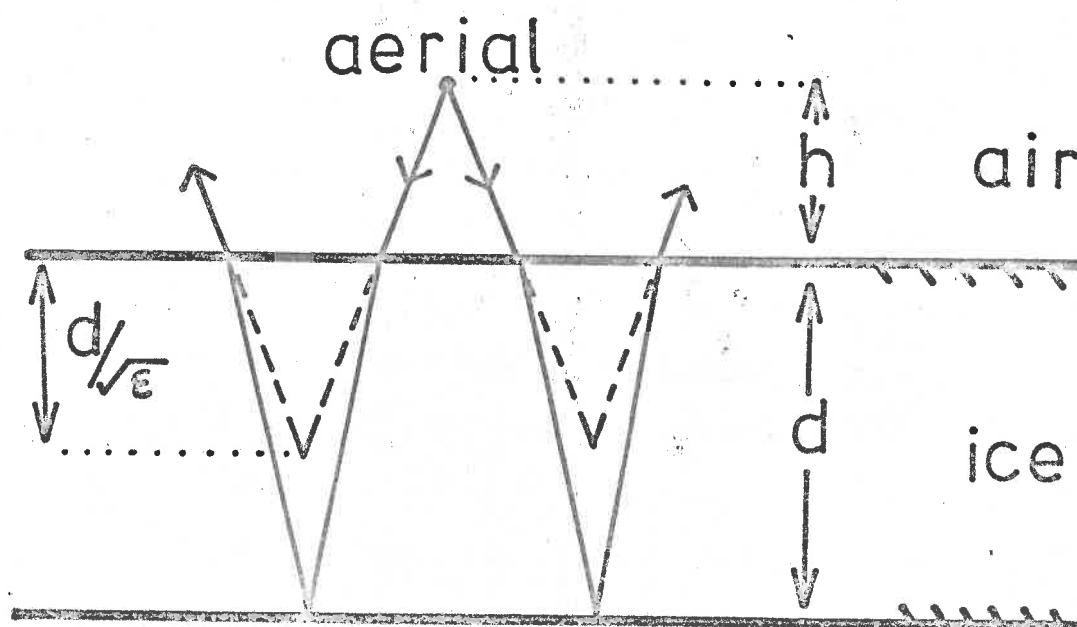


Figure 3.1.1

To illustrate the more gradual spreading of the wavefront in ice due to refraction at the air/ice interface.

### 3.2 Electromagnetic parameters and reflection coefficients

We have already asserted that the permeability of all media of interest is  $4\pi 10^{-7}$  henries  $m^{-1}$ . The permittivity of air is approximately  $\epsilon_0 = 10^{-9} / 36\pi$  farad  $m^{-1}$ . The permittivity of ice is almost constant over the frequency, temperature, and impurity ranges of interest. The table in figure 3.2.1 gives values for relative permittivity of ice according to Paren (1970). The conductivity varies with both temperature and impurity concentration. The conductivity of pure ice, that is having purity equal to, or higher than, distilled water in equilibrium with the atmosphere, is shown on the lower curve of figure 3.2.2. All in situ measurements of conductivity on temperate glaciers conform to this behaviour within a few percent, probably because the impurities have been flushed out (Nye and Frank 1971). An accurate empirical relation to absolute temperature according to Paren (1970) is:

$$\sigma = 4.6 \cdot 10^{-5} \exp - \left[ \frac{E}{R} \left( \frac{1}{T} - \frac{1}{T_0} \right) \right] \text{ ohm}^{-1} \text{ m}^{-1}$$

where  $E = 55 \text{ kJ mol}^{-1}$  for pure ice

$$R = 8.4 \text{ J mol}^{-1} \text{ K}^{-1}$$

$$T_0 = 273 \text{ K}$$

(15)

Most polar ice, on the other hand, conforms to the behaviour of 'solubility-limit' ice as described by Paren and Walker (1971). The total impurity content in polar conditions is usually higher than the equilibrium solubility for solid solution within the ice

grain; the excess impurity lies in the triple junctions of the grains and, because of the geometry, makes a negligible contribution to the bulk conductivity. Below  $-10^{\circ}\text{C}$  equation (15) may still be applied to obtain the conductivity of polar ice, but  $E = 25 \text{ kJ mol}^{-1}$  at the solubility limit. Above  $-10^{\circ}\text{C}$  both contributions to the conductivity are of comparable magnitude and they reinforce one another, reaching  $6 \cdot 10^{-5} \text{ ohm}^{-1} \text{ m}^{-1}$  at  $0^{\circ}\text{C}$  as shown in the upper curve of figure 3.2.2. In some situations in polar regions near to the melting point, temperate glacier behaviour is found, probably due to the flushing mechanism. Robin, Evans and Bailey (1969) found attenuations of 4.5 dB per 100 m for ice in Greenland having surface elevations below 1000 m, and the author measured attenuations of 4.8 dB per 100 m on the Fuchs Ice Piedmont, Adelaide Island, Antarctica. In addition to polar and temperate ice behaviour, there is sea ice having much higher conductivity as a result of inclusions of liquid brine. The problems of sea ice are not considered in this dissertation.

The permittivity of liquid water near the freezing point does not vary much with impurity concentration, but the conductivity varies over many orders of magnitude. The table in figure 3.2.1 gives some representative figures for conductivity.

The electrical properties of mixtures of dielectric materials are considered by Paren (1971) who has provided the following relations:

Dry snow is a mixture of ice and air in proportions which may be defined by the density ratio  $\rho' = \rho_{(\text{snow})} / \rho_{(\text{ice})}$

Then: 
$$\epsilon^{1/3}_{(\text{snow})} - 1 = \rho' (\epsilon^{1/3}_{(\text{ice})} - 1) \quad (16)$$

and 
$$\sigma_{(\text{snow})} = \sigma_{\text{ice}} \rho' (0.68 + 0.32 \rho') \quad (17)$$

Soaked snow, in which all available air spaces are filled with water, which is assumed to lie in randomly-oriented but inter-connecting veins, has permittivity:

$$\epsilon_{(\text{soaked})} = \epsilon_{(\text{dry})} + \frac{1}{3} \epsilon_{(\text{water})} (1 - \rho') \quad (18)$$

and conductivity:

$$\sigma_{(\text{soaked})} = \sigma_{(\text{dry})} + \frac{1}{3} \sigma_{(\text{water})} (1 - \rho') \quad (19)$$

The values of  $\sigma$  and  $\epsilon$  in figure 3.2.1 are virtually constant between 1 MHz and 500 MHz.

The dielectric properties of rocks have been studied by Parkhomenko (1967) for example. Unfortunately in many cases the nature of subglacial rock is unknown. However the relative permittivity of dry rock varies from about 2 for volcanic pumice

and tuff to about 10 for some forms of basalt. Granite has an intermediate value of between 5 and 6. The conductivity of minerals varies from the  $500 \text{ ohm}^{-1} \text{ m}^{-1}$  of native silver to the  $10^{-15} \text{ ohm}^{-1} \text{ m}^{-1}$  of native sulphur. However the conductivity of most rock-forming minerals is about  $10^{-8} \text{ ohm}^{-1} \text{ m}^{-1}$  when dry and about  $10^{-3} \text{ ohm}^{-1} \text{ m}^{-1}$  (much more variable) when wet. We are now in a position to evaluate the intrinsic impedance of any of the materials which we have discussed and, by using the mixture model of equations (18) and (19), we can evaluate the intrinsic impedance of mixtures of the materials. It is the intrinsic impedances of two media which determine the reflection and transmission coefficients of an electromagnetic wave crossing the interface between them. The reflection coefficient for normal incidence of a wave on the boundary between medium '1' and medium '2' is:

$$\rho_{12} = \frac{\eta_2 - \eta_1}{\eta_2 + \eta_1} \quad (20)$$

And the transmission coefficient is:

$$\tau_{12} = \frac{2\eta_2}{\eta_2 + \eta_1} \quad (21)$$

In general the intrinsic impedance of a medium as defined in

equation (4) is a complex quantity, and the coefficients expressed above are therefore also complex. The amplitude reflection and transmission coefficients are scalars, given by  $|\rho|$  and  $|\tau|$  respectively, the phase change on reflection or transmission being contained in the complex coefficient. The power reflection and transmission coefficients are given by:

$$R = |\rho|^2 \quad (22)$$

and

$$T = |\tau|^2 \frac{R_e(1/\eta_2)}{R_e(1/\eta_1)} \quad (23)$$

The reflection coefficient of power does not include the impedances of the media (except in  $\rho$ ) because reflection occurs into the same medium as the incident wave. The transmission coefficient of power has to take into account the impedance change in accordance with equation (6). The sum of the power reflection and transmission coefficients is unity, i.e. energy is conserved at the interface. We will now evaluate the reflection and transmission coefficients for some of the interfaces which are commonly encountered in glaciers.



We will take five media as representative: air ( $\epsilon = 1$ ); snow of density  $0.5 \text{ Mg m}^{-3}$  ( $\epsilon = 2$ ); ice ( $\epsilon = 3.2$ ); water ( $\epsilon = 80$ ) and rock ( $\epsilon = 6$ ). We neglect the small effect of the finite conductivities of these media. The power reflection and transmission coefficients in dB are tabulated in figure 3.2.3. It may be seen that an echo from the bottom of a glacier will be some 12 dB stronger if the glacier rests on water than it would be if the glacier rested on rock. If the calculation is performed for highly conducting sea water, then the power loss on reflection at the ice/water interface would be even less.

We have already seen that certain volcanic rocks may have a relative permittivity which is less than that of ice, it is therefore possible to conceive of an ice/rock interface having no discontinuity in relative permittivity and from which almost no power is reflected, but this situation must be very rare. The effect on reflection coefficient due to roughness of an interface might, in an extreme example, cause an additional loss of 10 dB (Beckmann and Spizzichino p 89). However in any example where the reflection could be loosely described as specular and where 'normal incidence' is meaningful then the additional loss should be much less than this figure. The net power reflected and transmitted from an interface such as we have calculated only applies to the simple case of a single incident wave and two infinite media. The next section deals with a more complicated situation.

	$\epsilon$	$\sigma \text{ ohm}^{-1} \text{ m}^{-1}$	
Ice at 0°C	3.24±0.03	(fig 3.2.2)	Paren (1970)
Ice at -40°C	3.20±0.03		

Water at 0°C

Pure	86	3.6 $10^{-6}$	Hasted (1961)
Distilled	86	1 $10^{-4}$	(in equilibrium with atmosphere)
Temperate glacier melt	86	2 $10^{-4}$	Gorham (1958)
Polar ice melt	86	2 to 8 $10^{-4}$	Paren & Walker (1971)
Rain (Norway)	80	1 to 30 $10^{-3}$	Egner & Eriksson (1955)
-do- typical	80	4 $10^{-3}$	
Brine, given salinity in parts per 1000 (s)	<80	9 s $10^{-2}$	Handbook. U.S. Navy Oceanographic Office (1966)
Sea water	77	2.9	Hasted (1961)

Figure 3.2.1

A table of conductivity and relative permittivity of ice and various waters.

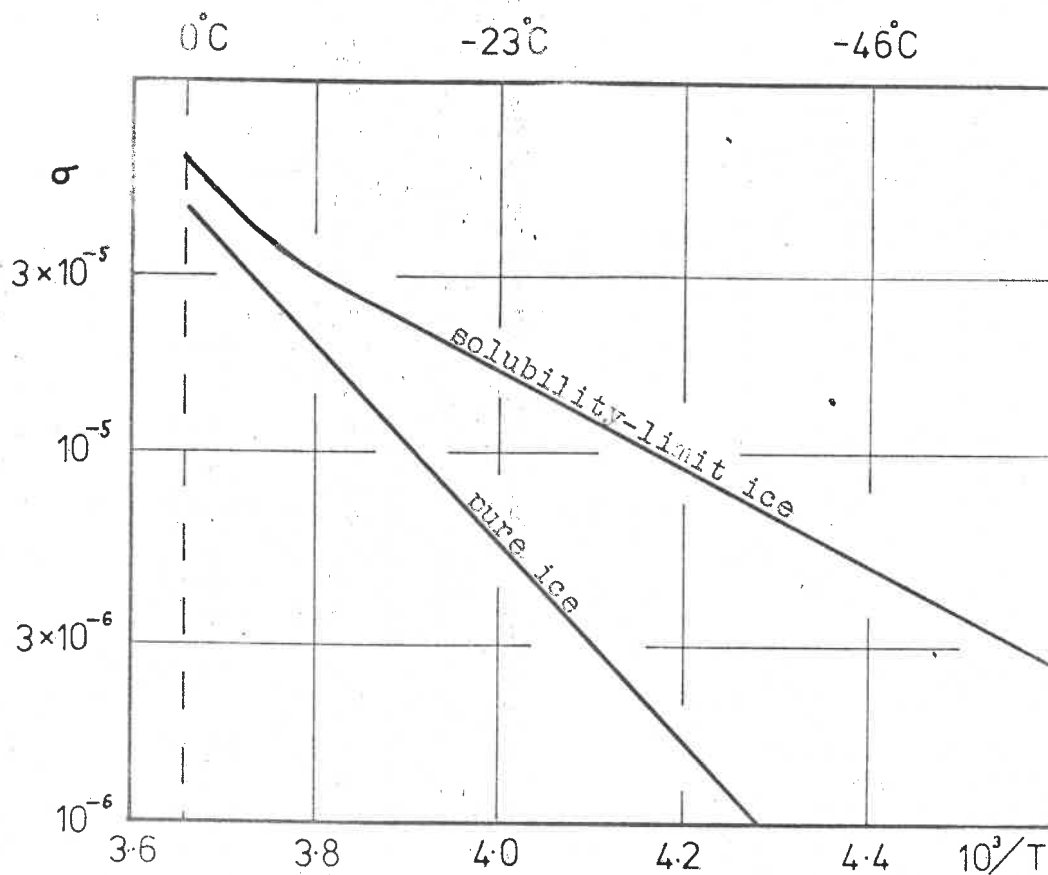


Figure 3.2.2

The conductivity of ice,  $\sigma$  in  $\text{ohm}^{-1} \text{m}^{-1}$  as a function of temperature,  $T$  in degrees Kelvin. The upper curve (solubility-limit ice) usually applies to polar ice, and the lower curve (pure ice) usually applies to temperate glacier ice.

Interface	Power loss on reflection(dB)	Power loss on transmission(dB)
Air/snow	15.3	0.1
Air/ice	11.0	0.3
Air/water	1.9	4.4
Air/rock	7.3	0.9
Snow/ice	18.6	0.0
Ice/water	3.5	2.5
Ice/rock	15.6	0.1

Figure 3.2.3

Power reflection and transmission coefficients  
in dB, for various interfaces.

### 3.3 Three layer problem

Consider two media of infinite extent separated by a plane layer medium of uniform thickness  $t$  as shown in figure 3.3.1. We shall evaluate the power reflected by, and transmitted through, the layer in terms of the three intrinsic impedances and the propagation constant of the middle layer. The incident wave is normal to the interface although in figure 3.3.1 it is shown at a small angle in the interests of clarity. If the incident wave has an amplitude of  $\mathcal{E}$ , then the reflected wave is the sum of an infinite number of multiply reflected waves as shown:

$$\begin{aligned} & \mathcal{E} \rho_{12} + \mathcal{E} \tau_{12} \rho_{23} \tau_{21} e^{-2\gamma t} \\ & + \mathcal{E} \tau_{12} \rho_{23} \rho_{21} \rho_{23} \tau_{21} e^{-2\gamma t} e^{-2\gamma t} \\ & + \dots \end{aligned} \quad (24)$$

which is equal to

$$\mathcal{E} \left\{ \rho_{12} + \tau_{12} \rho_{23} \tau_{21} e^{-2\gamma t} (1 + D + D^2 + \dots) \right\} \quad (25)$$

where:  $D = \rho_{21} \rho_{23} e^{-2\gamma t}$

The reflection coefficient  $R$  is therefore given by:

$$R = \rho_{12} + \frac{\tau_{12} \rho_{23} \tau_{21} e^{-2\gamma t}}{1 - \rho_{21} \rho_{23} e^{-2\gamma t}} \quad (26)$$

In a similar way the transmitted wave is the sum of an infinite series of multiply reflected waves:

$$\begin{aligned} & e^{-\gamma t} \tau_{12} \tau_{23} \\ & + e^{-\gamma t} \tau_{12} \rho_{23} \rho_{21} e^{-2\gamma t} \tau_{23} \\ & + \dots \end{aligned} \quad (27)$$

which is equal to:

$$e^{-\gamma t} \tau_{12} \tau_{23} (1 + D + D^2 + \dots) \quad (28)$$

where  $D = \rho_{23} \rho_{21} e^{-2\gamma t}$

Hence the transmission coefficient  $T$  is given by:

$$T = \frac{\tau_{12} \tau_{23} e^{-\gamma t}}{1 - \rho_{23} \rho_{21} e^{-2\gamma t}} \quad (29)$$

As we saw in the last section, the amplitude reflection and transmission coefficients are  $|R|$  and  $|T|$  respectively and the power reflection and transmission coefficients are

$$|R|^2 \text{ and } |T|^2 \frac{Re(\frac{1}{\eta_2})}{Re(\frac{1}{\eta_1})} \text{ respectively.}$$

It should be noted that strictly these results only apply if media 1 and 3 are of infinite extent, and to a continuous incident wave. In practice however, the results will apply if the incident pulse length is long compared to the length of the intermediate layer and short compared with the finite dimensions of the other media. In the following sections the expressions have been evaluated by a digital computer for a number of examples which are known to occur or suspected in nature.

Saxton (1950) has derived reflection coefficients for plane waves in air, incident on ice or snow lying above land or sea. His analysis neglects the effect of conductivity, and he has used incorrect values for the relative permittivity of ice and of snow. In addition he has not evaluated transmission coefficients for the three layer problem, and in general the sum of the power reflection and transmission coefficients is not unity. His results have not been used.

As we saw in the last section, the amplitude reflection and transmission coefficients are  $|R|$  and  $|T|$  respectively and the power reflection and transmission coefficients are

$$|R|^2 \text{ and } |T|^2 \frac{R_e(\frac{1}{\eta_2})}{R_e(\frac{1}{\eta_1})} \text{ respectively.}$$

It should be noted that strictly these results only apply if media 1 and 3 are of infinite extent, and to a continuous incident wave. In practice however, the results will apply if the incident pulse length is long compared to the length of the intermediate layer and short compared with the finite dimensions of the other media. In the following sections the expressions have been evaluated by a digital computer for a number of examples which are known to occur or suspected in nature.

Saxton (1950) has derived reflection coefficients for plane waves in air, incident on ice or snow lying above land or sea. His analysis neglects the effect of conductivity, and he has used incorrect values for the relative permittivity of ice and of snow. In addition he has not evaluated transmission coefficients for the three layer problem, and in general the sum of the power reflection and transmission coefficients is not unity. His results have not been used.



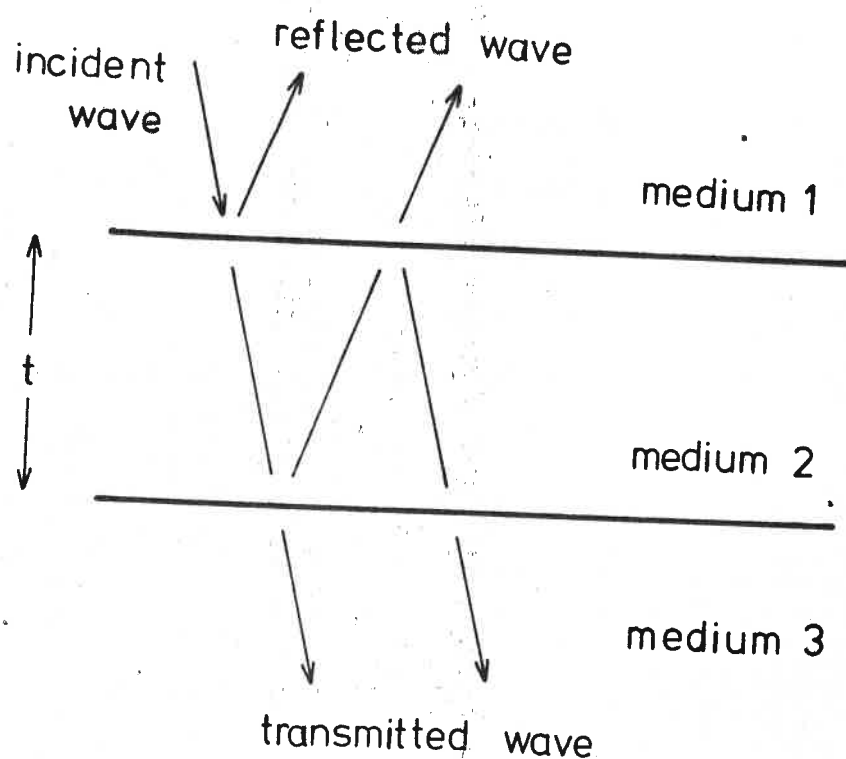


Figure 3.3.1

Three media of propagation having two parallel interfaces, showing the reflected and transmitted waves due to an incident wave close to the normal.

### 3.4 Surface melt layer

Figure 3.4.1 shows the computed power transmission coefficient for a 35 MHz wave passing through a layer of water ( $\sigma = 2 \cdot 10^{-4} \text{ ohm}^{-1} \text{ m}^{-1}$ ) lying between air and solid ice as a function of layer thickness. For an infinitely thin layer the loss is not zero but 0.3 dB; this is the loss due to reflection at an air/ice interface. When the water layer is a quarter wavelength (in water) thick, the loss is a maximum of about 11 dB. For depths up to several metres the loss by absorption in the water is negligible, this is evident from the almost constant maximum and minimum values in the interference pattern. If, in equation (5), we make the assumption that  $\sigma$  is much less than  $\omega\epsilon$ , then the expression for  $\alpha$  becomes:

$$\alpha = \frac{\sigma \eta}{2} \quad (30)$$

This gives an attenuation in the medium of  $4.34 \sigma \eta \text{ dB m}^{-1}$ . Using this figure we see that the attenuation in ice ( $\sigma = 5 \cdot 10^{-5} \text{ ohm}^{-1} \text{ m}^{-1}$ ;  $\eta = 210 \text{ ohm}$ ) is approximately the same as in water ( $\sigma = 2 \cdot 10^{-4} \text{ ohm}^{-1} \text{ m}^{-1}$ ;  $\eta = 42 \text{ ohm}$ ) both being about 4 dB because, although the conductivity of water is higher, the relative permittivity is also higher and hence the intrinsic impedance is lower. Within the limit of a few metres depth whilst

the absorption is small, the behaviour at other radio frequencies may be read from figure 3.4.1 by scaling the horizontal axis. For very thin layers a linear approximation may be fitted to the loss on transmission through the layer, and we find that loss is  $(2.4 f t)$  dB; where  $f$  is the frequency in MHz and  $t$  is the thickness in metres.

During the summer season, on George VI Sound in the Antarctic Peninsula, there are numerous melt pools on the surface of the ice. They occur between latitudes  $70^{\circ}40'S$  and  $71^{\circ}50'S$  where the ice is about 200 m thick and floating. The pools are typically 0.5 m deep and are thought to be caused by a lowering of the albedo by wind blown dust from the adjacent sedimentary rock exposures (private communication from A.C. Wager). There is no evidence on radio echo sounding records obtained in this area by the author and by Swithinbank (1968) that melt pools cause the bottom echo to be lost. This result is somewhat surprising at first but remembering that in this situation the signal may be 60 dB over the receiver sensitivity, the loss of about 5 dB in each direction for a 0.5 m pool (two-way loss 10 dB) would not be expected to eclipse the bottom echo.

On the Roslin glacier in Greenland, J.L. Davis and Halliday (private communication) observed a weakening of about 10 dB in the strength of the bottom echo at 440 MHz during the daytime when a film of water was visible on the glacier surface. Putting  $2.4 f t = 5$  dB

attenuation in each direction, a layer only 5 mm thick is required at this frequency. The maximum attenuation is still 11 dB but several such layers could each contribute an average of 5 dB to the total one-way loss. Since the water layer has such a high relative permittivity we might consider the error in the measured depth due to an unsuspected melt layer. The ratio of the velocities in ice and water is  $\sqrt{3.2/80} \approx 1/5$ . Thus the echo time delay in 1 m water is equal to that in 5 m ice. Since such pools are in general less than a metre deep this effect may be neglected. Having established the rather surprising result that the attenuation in the water is not very great, we will consider the possibility of the layer 'ringing' and hence extending the length of the echo from the surface. Referring to figure 3.2.3 the loss on transmission through an air/water interface is 4.4 dB and the loss on reflection at a water/ice interface is 3.5 dB. Thus the first transit of the pulse through the water and back to the receiver is attenuated by 12.3 dB. Subsequent double reflections are attenuated by 1.9 dB at the water/air interface and by 3.5 dB at the water/ice interface. The total attenuation of an emerging ray due to these factors is therefore  $(12.3 + 5.4 n)$  where  $n$  is the number of double reflections. If we have a system performance of 160 dB, an aerial gain of 1.6, and a frequency of 35 MHz, then in equation (12) the sensitivity in hand is 95 dB if the height of the aircraft is 1000 m.

A value of  $n = 15$  would reduce this to zero dB, so that a maximum of fifteen double reflections might be detected. If the pool is 0.5 metres thick, the path length in water would be 15 metres; corresponding to about 75 metres of ice. This might be detectable but notice that we have ignored the diverging of the pulse in the water, and also the attenuation by absorption. In practice a melt pool sufficiently parallel for this phenomenon to occur would not be found. The only manifestation of this effect might be a slight lengthening of the trailing edge of the surface echo. This has not been conclusively observed in practice.

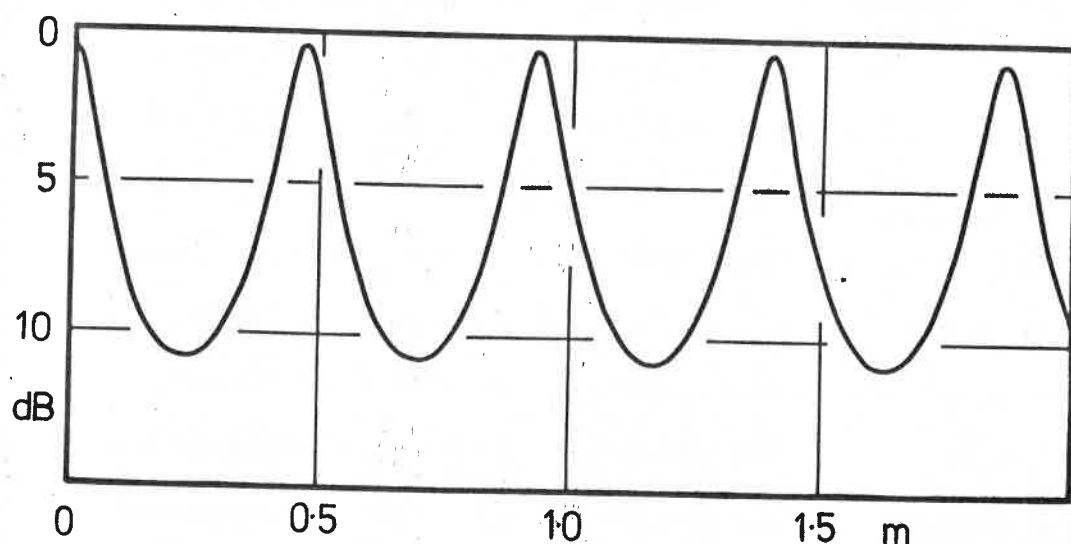


Figure 3.4.1

The attenuation in dB of a 35 MHz wave passing through a layer of melt water ( $\sigma = 2 \cdot 10^{-4} \text{ ohm}^{-1} \text{ m}^{-1}$ ) lying between air and solid ice, as a function of layer thickness in metres. In practice such a layer is traversed twice and the total attenuation of the echo is twice the ordinate value.

### 3.5 Brine percolation layer

Figure 3.5.1 shows the computed power transmission coefficient for a 35 MHz wave passing through a highly conducting water layer. In this case the principal attenuation is due to absorption rather than reflection. Curve (a) refers to a layer of sea water ( $\sigma = 2.9 \text{ ohm}^{-1} \text{ m}^{-1}$ ) lying within an almost solid ice medium ( $\rho = 0.8 \text{ Mg m}^{-3}$ ). It may be seen that a layer 0.1 m thick would give an attenuation of 30 dB in each direction, and is a function of radio frequency. It is not very likely that such a situation would be found in nature. In ice shelves it has often been suggested that in some places sea water percolates horizontally through porous layers at about sea level from rifts or from the ice front (Dubrovin 1962, Heine 1968, Swithinbank 1970). The phenomenon has been observed in the McMurdo, Brunt and Lazarev ice shelves, but may be inferred from radio echo records obtained by the author on the Wordie and Larsen ice shelves and Wilkins Sound. In all of these places reflecting surfaces occasionally appear near sea level with the absence of a bottom echo. An example is shown in figure 3.5.2. Curve (b) on figure 3.5.1 shows the attenuation on passing through a layer of brine-soaked firn as a function of layer thickness. The first and third media are firn of density  $0.8 \text{ Mg m}^{-3}$  and the layer is assumed to consist of the same firn but with all air pockets filled with brine ( $\sigma = 2.9 \text{ ohm}^{-1} \text{ m}^{-1}$ ) according to equations (18) and (19).

In this case the attenuation is less but it is still predominantly absorption, and therefore insensitive to frequency. A layer 1 m thick would cause 38 dB attenuation in each direction. A total of 76 dB additional attenuation would invariably extinguish the bottom echo.



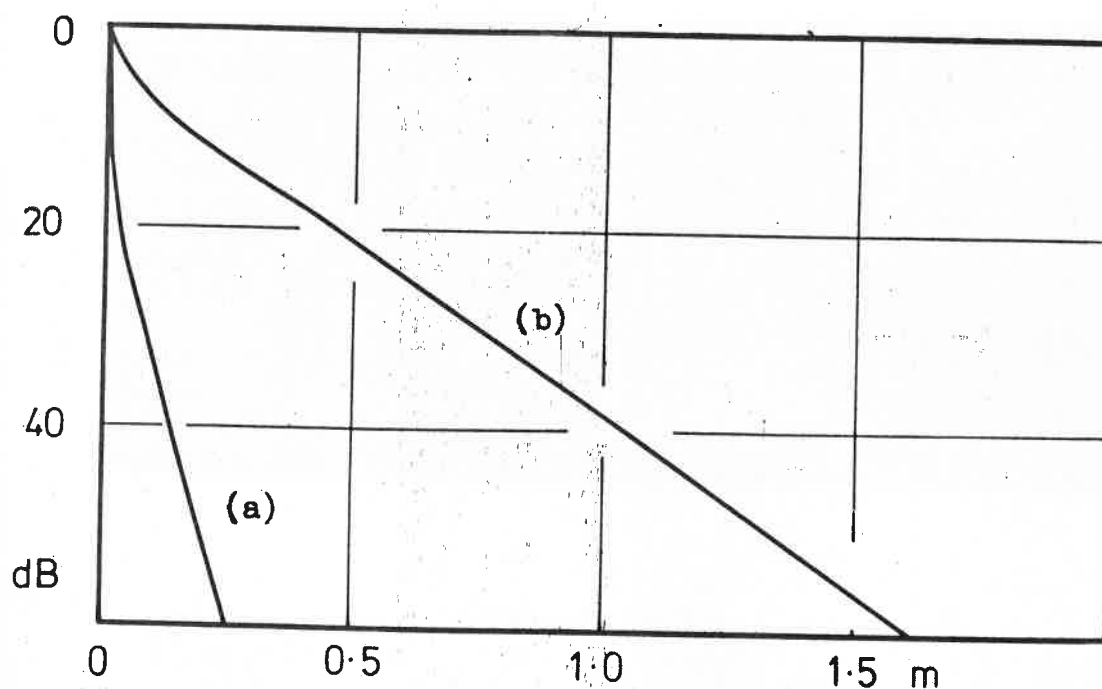


Figure 3.5.1

(a) The attenuation in dB of a 35 MHz wave passing through a layer of brine ( $\sigma = 2.9 \text{ ohm}^{-1} \text{ m}^{-1}$ ) lying within a firn medium ( $\rho = 0.8 \text{ Mg m}^{-3}$ ), as a function of layer thickness in metres.

(b) The upper curve shows the attenuation in the same circumstances except that the layer consists of brine-soaked firn instead of pure brine.

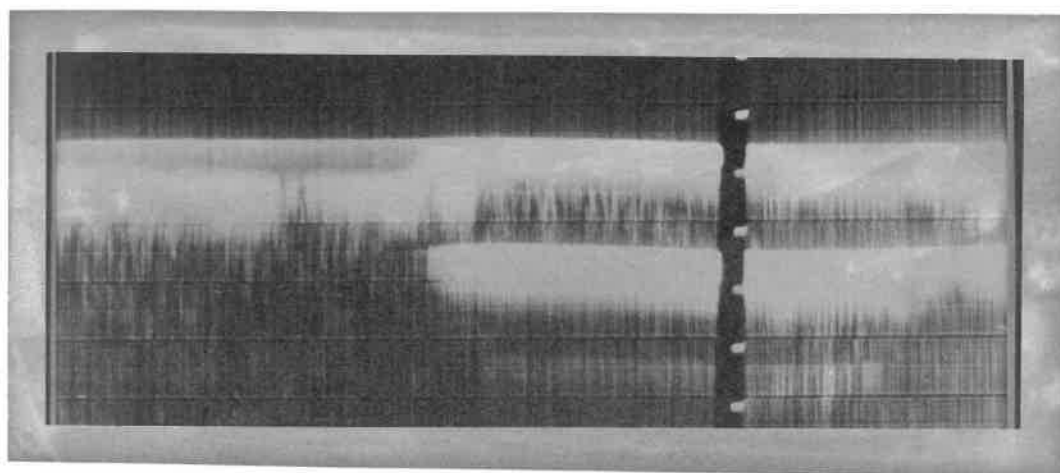


Figure 3.5.2

A section of a radio echo record obtained on the Larsen Ice Shelf (lat. 68°S long. 60°W). The range calibration marks are at  $1\mu\text{S}$  intervals and on the right of the photograph, echoes from the surface and bottom of the ice show it to be 150 m thick. On the left of the photograph there is a reflecting layer at about 45 m below the ice surface and the bottom echo is extinguished. Since the surface is flat, it is supposed that brine has percolated horizontally through the porous upper layers from one of the nearby rifts which contain sea water. .

### 3.6 Rain soaking of firm

The conductivity of rain water is two or three orders of magnitude lower than that of sea water. Since rain often falls on temperate glaciers we will consider the effect of soaking part of the permeable layers of a glacier with rain water. Figure 3.6.1 shows the attenuation of a 35 MHz wave passing through a rain-soaked layer, as a function of layer thickness. A rain water conductivity of  $4 \cdot 10^{-3} \text{ ohm}^{-1} \text{ m}^{-1}$  has been used. This value typifies measurements made in the vicinity of Norwegian glaciers (Egner and Eriksson 1955). The upper curve assumes firm of density  $0.8 \text{ Mg m}^{-3}$  and the lower curve assumes firm of density  $0.5 \text{ Mg m}^{-3}$ . The attenuation is greater in the less dense firm, there being more water present, but even 50 m of soaking contribute only 16 dB to the attenuation in each direction. In practice it is unlikely that low density snow would be 50 m thick. The general trend of the curves is due to absorption, while the cyclic structure is due to interference by reflection. The latter is more marked in the low density example because the discontinuity in permittivity is greater. At other radio frequencies the horizontal scale of the periodicities would be changed but the asymptotic gradient would remain the same. The attenuations which are calculated on figure 3.6.1 cannot explain the difficulties encountered in echo sounding temperate glaciers. One possibility is that rain soaking actually occurs in several quite thin layers. This could be the case if the rain water settles

on to annual layers or other horizons within the ice. In this way five such layers each contributing 2 dB would cause a total attenuation of 10 dB in each direction. The effect of a substantial water content on the velocity of propagation must also be considered. The worst case will be the low density example (  $\rho = 0.5 \text{ Mg m}^{-3}$  ) since that has the greatest water content. Using equation (18) the relative permittivity of the soaked firn is 15.2 which gives a velocity ratio of soaked firn to solid ice which is  $\sqrt{3.2/15.2}$  or 1/2.3. If 50 metres of firn were soaked in this way it would appear the same as 115 metres of ice, an error of 65 metres.

G. de Q. Robin has suggested that variations in bottom echo delay time with season could provide information about the variation of water content in the glacier.

It is perhaps more likely that rain-soaked layers settling on to annual strata in the firn would result in a series of firn/ice/firn bands within the glacier and it is this example which we will consider next.

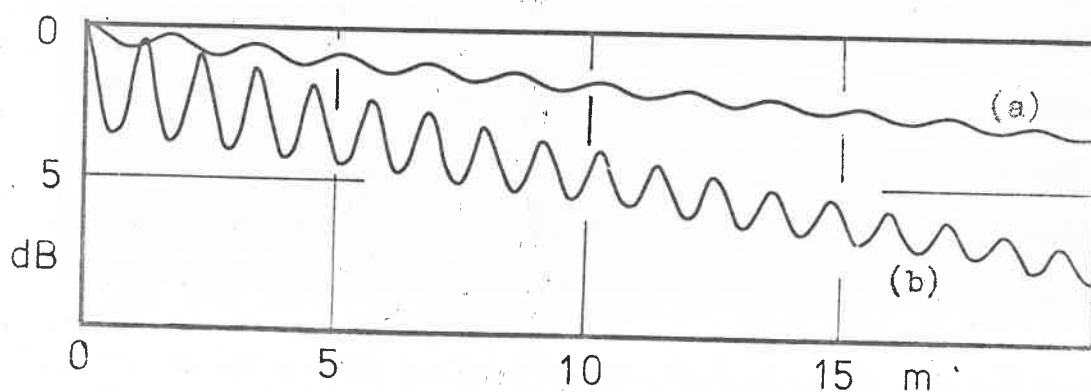


Figure 3.6.1

The attenuation of a 35 MHz wave passing through firn having a layer of rain soaking ( $\sigma$  [rain] =  $4 \cdot 10^{-3}$  ohm $^{-1}$  m $^{-1}$ ) as a function of layer thickness. The upper trace (a) applies to firn of density  $0.8 \text{ Mg m}^{-3}$ , and the lower trace (b) to firn of density  $0.5 \text{ Mg m}^{-3}$ .

### 3.7 Solid ice layering within firm

Layers of ice within less dense firm have often been observed, see for example Müller (1963 p 31). These are usually interpreted as marking the occurrence of summer melting of the firm and re-freezing as solid ice during the winter. Figure 3.7.1 shows the attenuation of a 35 MHz wave by one such layer as a function of thickness. The two curves represent solid ice within firm of density  $0.5 \text{ Mg m}^{-3}$  and firm of density of  $0.8 \text{ Mg m}^{-3}$ . In the high density example, the discontinuity in impedance is so slight that almost no interference due to reflection is visible. Some interference is apparent in the low density example but both tend to about 5 dB per 100 m for a thick layer. A layer of ice 1 m thick causes an attenuation of about 0.3 dB in the low density firm, so that 10 such layers would cause a total attenuation of about 6 dB. This is an extreme example, but notice that the same effect would be produced by layers only 100 mm thick at 350 MHz.

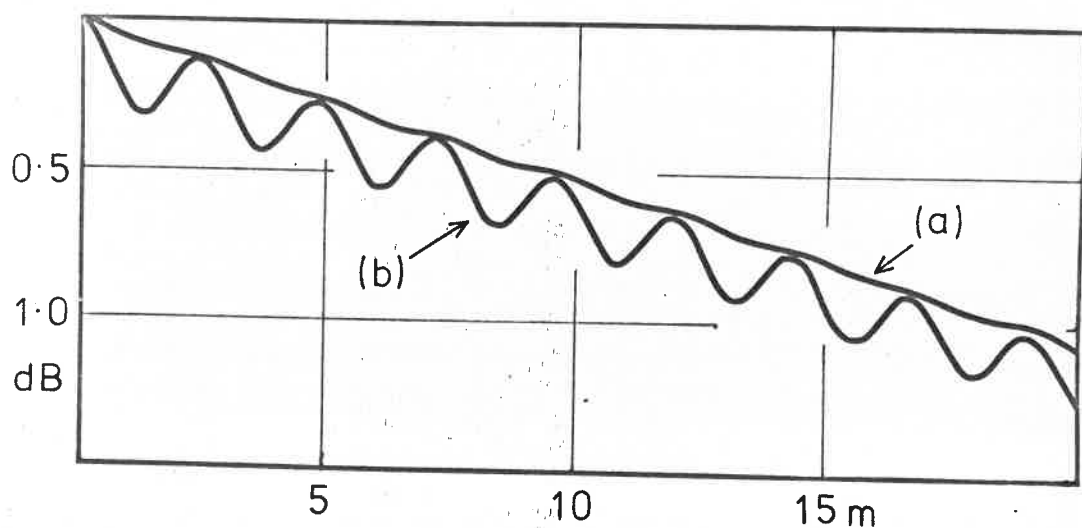


Figure 3.7.1

The attenuation in dB of a 35 MHz wave passing through a layer of solid ice embedded in firn, as a function of layer thickness. Curve (a) applies to firn of density  $0.8 \text{ Mg m}^{-3}$ , and curve (b) applies to firn of density  $0.5 \text{ Mg m}^{-3}$ .

### 3.8 Scattering losses

We have so far only considered laminar irregularities in the ice. On the microscopic scale we have said nothing about the dimensions of inhomogeneities in our models for the electrical properties of snow, rain soaking, etc. It is clear, however, that inhomogeneities of a finite size will scatter power out of the forward wave. For simplicity of analysis consider spheres of one medium, embedded in a uniform second medium. This will provide an order of magnitude solution from which we may infer the effect of changing the scale of the irregularities.

An isolated dielectric sphere of radius  $b$  and permittivity  $\epsilon_1 \epsilon_0$  embedded in a medium of permittivity  $\epsilon_2 \epsilon_0$ , with an incident wave of amplitude  $\mathcal{E}_0$  becomes an electric dipole of moment:

$$4 \pi b^3 \epsilon_2 \epsilon_0 \left( \frac{\epsilon_1 - \epsilon_2}{\epsilon_1 + 2 \epsilon_2} \right) \mathcal{E}_0 \quad (31)$$

(Stratton 1941 p 572)

Substituting the power radiated by a dipole (Stratton 1941 p 437) and the power flow in the incident wave  $P_i$  using equation (6), we find the scattered power  $P_s$  from a single spherical inhomogeneity to be:

$$P_s = \frac{8}{3} \pi \omega^4 b^6 (\mu_0 \epsilon_2 \epsilon_0)^2 \left( \frac{\epsilon_1 - \epsilon_2}{\epsilon_1 + 2 \epsilon_2} \right)^2 P_i \quad (32)$$



If there are  $m$  similar spheres per cubic metre, then the fraction of the power lost from the forward wave per metre path through the medium is:

$$\delta = \frac{8\pi}{3} m b^6 \left( \frac{2\pi}{\lambda_0} \right)^4 \left[ \frac{\epsilon_2 (\epsilon_1 - \epsilon_2)}{\epsilon_1 + 2\epsilon_2} \right]^2 \quad (33)$$

The attenuation is:  $10^3 \log_{10} (1 - \delta)$  dB per 100 m.

If  $\delta \ll 1$  this becomes:  $434 \delta$  dB per 100 m.

We will now consider three possible inhomogeneities in snow of density  $0.5 \text{ Mg m}^{-3}$ .

Suppose that the snow is an ice matrix containing spherical air bubbles. Then  $\epsilon_1 = 1$  and  $\epsilon_2 = 3.2$

Using the relation:  $\frac{4}{3} \pi b^3 m = 1 - 0.5/0.92$

we find that  $m b^3 = 10^{-1}$ . If the bubbles of air have a characteristic radius of 1 mm then  $m b^6 = 10^{-10}$ . Using equation (33) we find that the attenuation is:

$$\frac{5 \cdot 10^{-4}}{\lambda_0^4} \quad \text{dB per 100 m} \quad (34)$$

This attenuation is clearly negligible for metric wavelengths.

We now consider soaked snow having all available space occupied by spheres of water. In this case  $\epsilon_2 = 3.2$  and  $\epsilon_1 \gg \epsilon_2$ . The value of  $m b^6$  is  $10^{-10}$  as before. The attenuation is then:

$$\frac{5 \cdot 10^{-3}}{\lambda_0^4} \quad \text{dB per 100 m} \quad (35)$$

Again this may be neglected for metric wavelengths, rising to only 10 dB per 100 m for a free space wavelength of 0.15 m.

Finally we consider the effect of larger spheres of ice embedded in the less dense snow. Such ice lenses are observed although they usually have a somewhat flattened shape, being larger horizontally than vertically. Figure 3.8.1 shows an example of spheres 50 mm radius separated 250 mm between centres. Then  $m b^6 = 10^{-6}$ ,  $\epsilon_1 = 3.2$  and  $\epsilon_2 = 2.0$ . The attenuation in this example is given by:

$$\frac{7 \cdot 10^{-1}}{\lambda_0^4} \quad \text{dB per 100 m} \quad (36)$$

For this dense system of irregularities, our assumption that multiple scattering is unimportant may not apply. It does however provide an upper limit since an increasingly dense arrangement of

ice lenses would soon tend to become more homogeneous. In practice the lenses would probably extend further in the horizontal plane, and would tend towards the three layer example.

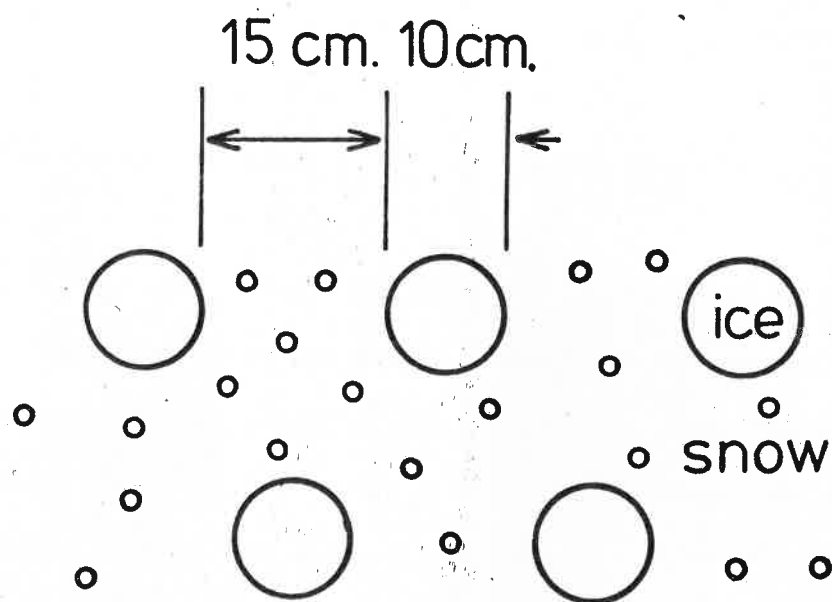


Figure 3.8.1

To illustrate spherical ice 'lenses' of radius  
50 mm, spaced 250 mm between centres, in firn.

### 3.9 Background signal due to scatter echoes

At frequencies below 500 MHz ( $\lambda_0 = 0.67 \text{ m}$ ) none of the mechanisms so far considered should normally reduce the strength of the bottom echo to below the receiver sensitivity. There is one further consideration; the signal to noise ratio of bottom echo to scattered echo.

The product of the transmitter pulse duration and the velocity of propagation in the medium defines a pulse length  $\ell$  metres. At any instant scattered echoes are returning from a shell of thickness  $\ell/2$  at range  $r$ . If the transmitter aerial has a gain  $G$  then the area being illuminated is  $4\pi r^2/G$  and the volume illuminated is  $2\pi\ell r^2/G$ . If there are  $m$  scattering spheres per cubic metre then at any instant power is received from a number of spheres defined by:

$$n = m \ 2\pi\ell r^2/G \quad (37)$$

If we assume that each scattering centre has a backwards scattering gain of 1.6 (being an elementary dipole), and the receiver aerial has a cross sectional area of  $G\lambda_0^2/4\pi$  from equation (1) then the power received from each dipole is:

$$P_r = P_s \ 1.6 \ \frac{G\lambda_0^2}{(4\pi r)^2}$$

where  $P_s$  is defined by equation (32).

The total power received from the scattering shell is therefore:

$$P_r = \frac{1.6}{3} m l \lambda_o^2 \omega^4 b^6 (\mu_o \epsilon_2 \epsilon_o)^2 \left( \frac{\epsilon_1 - \epsilon_2}{\epsilon_1 + 2 \epsilon_2} \right)^2 P_i \quad (38)$$

where  $P_i$  is the incident power on the shell and is given by:

$$P_i = P_t \frac{G}{4\pi r^2} \quad (39)$$

Substituting this in the above expression we find that the total power received as a fraction of that transmitted is given by:

$$\frac{P_r}{P_t} = \frac{64 \pi^3 G l}{30 r^2 \lambda_o^2} \left( \frac{\epsilon_2 (\epsilon_1 - \epsilon_2)}{\epsilon_1 + 2 \epsilon_2} \right)^2 m b^6 \quad (40)$$

We must now compare the power received from a plane reflector at the same range, having a power reflection coefficient  $R$ . Using equation (12), remembering that  $\rho$  is the amplitude reflection coefficient, we have:

$$\frac{P_r}{P_t} = \left( \frac{G \lambda}{8 \pi r} \right)^2 R \quad (41)$$

Both echoes are attenuated by absorption in the medium, but the attenuation will be the same for both, so the signal to noise ratio is independent of range and is given by:

$$\frac{P_r \text{ (plane)}}{P_r \text{ (scattered)}} = \left\{ \frac{6 \cdot 10^{-6} G \lambda_o^4}{l} \right\} \left\{ \frac{R}{\pi b^6} \left( \frac{\epsilon_1 + 2 \epsilon_2}{\epsilon_2 (\epsilon_1 - \epsilon_2)} \right)^2 \right\} \quad (42)$$

Notice that the expression has been divided into two parts; the first contains all the factors that characterize the equipment and which can, in principle, be changed; the second contains all the factors which are characteristic of the glacier. Using the parameters of the Mark 4 equipment:  $\lambda_o = 8.6 \text{ m}$ ;  $G \approx 2$ ; and

$l = 40 \text{ m}$ ; we find that the first factor is equal to -28 dB.

If we take a value of -20 dB for the power reflection coefficient at the base of the glacier, then the example of rain-filled bubbles in equation (35) makes the second factor 70 dB, and for the ice-lens model of equation (36) it is 49 dB. In both cases the signal is stronger than the noise, but this result depends strongly on wavelength ( $\lambda^4$ ) and on bubble radius ( $b^6$ ). An increase in the system performance will not improve this situation, since the scattered power will increase by the same factor as the wanted signal. A change in frequency would normally be accompanied by a change in the aerial gain and pulse length so that the wavelength

dependence might not be quite as strong as suggested by equation (42), in practice. For a constant physical size of aerial  $G \lambda_o^2$  will be approximately constant, and one might expect to change  $\ell$  proportionally with  $\lambda_o$ . So that the practical wavelength dependence is more likely to be  $\lambda$  to the first power. It might at first be thought that the scattered echo power would decrease rapidly at ranges greater than the bottom, but figure 3.9.1 illustrates why this is not necessarily the case. Figure 3.9.2 shows a radio echo record obtained by the author on Adelaide Island, Antarctica, using the 35 MHz Mark 4 equipment in an aircraft. Although the bottom echo is 40 dB above the receiver sensitivity it is lost in the centre of the picture at a depth of 150 m. Summer melting in this area might be expected to produce ice lenses of large horizontal extent. Figure 3.9.3 shows a radio echo record obtained by the author on the Jostedalsgreen, Norway, using a sledge-mounted Mark 2 echo sounder. Here again the echo is 40 dB over noise, but it is lost in the scattered echoes at about 150 m. Figure 3.9.4 shows a radio echo record obtained on the Hardangerjøkul, Norway, by S. Evans using a Mark 3 radio echo sounder on a frequency of 480 MHz. The echo disappears into scattered echoes at a depth of about 100 m.

It is difficult to see how this obstruction to the sounding of temperate glaciers might be overcome. The use of lower carrier frequencies involves an unfortunate loss of resolution and causes



problems with sky noise, ionospheric interference and indeed frequency allocation. In addition aerial problems at long wavelengths become more acute. Nevertheless in some cases this might be the only way of obtaining a useable signal to noise ratio.

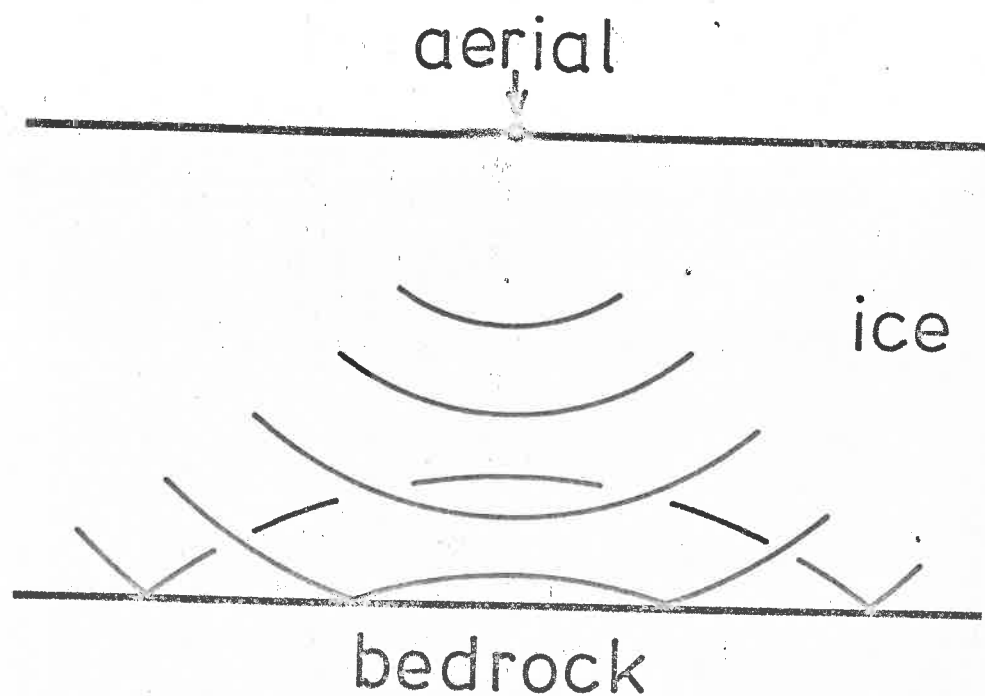


Figure 3.9.1

To illustrate the way in which scatter echoes may be received from a 'shell' of radius greater than the ice depth.

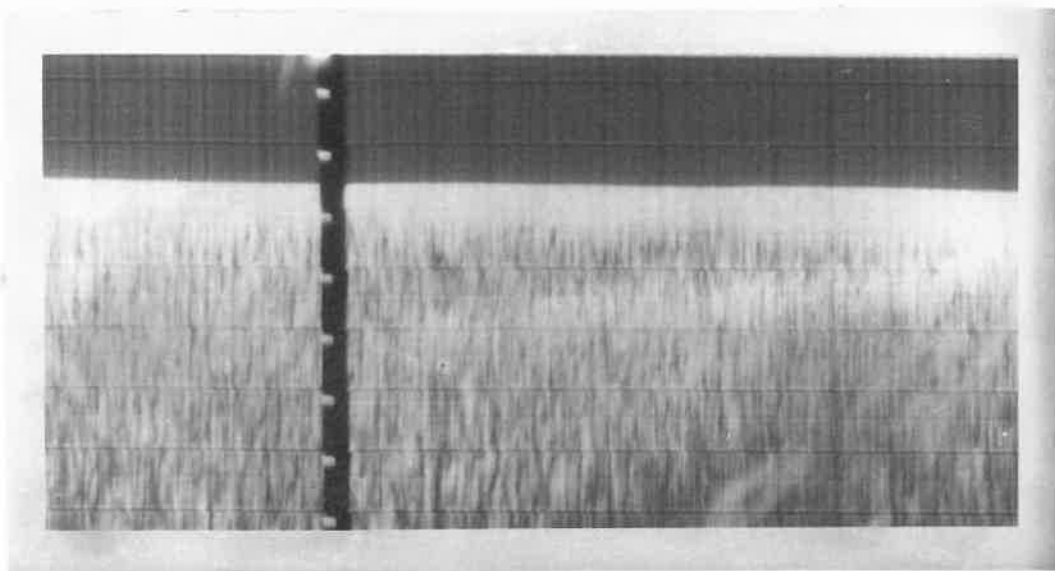


Figure 3.9.2

A radio echo record obtained on the Fuchs Ice Piedmont, Adelaide Island, Antarctica using the Mark 4 sounder in an aircraft. The scatter echoes are probably due to ice lenses within the firn. The bottom echo is 40 dB above the receiver noise level but is lost in the scatter echoes at 150 m depth.

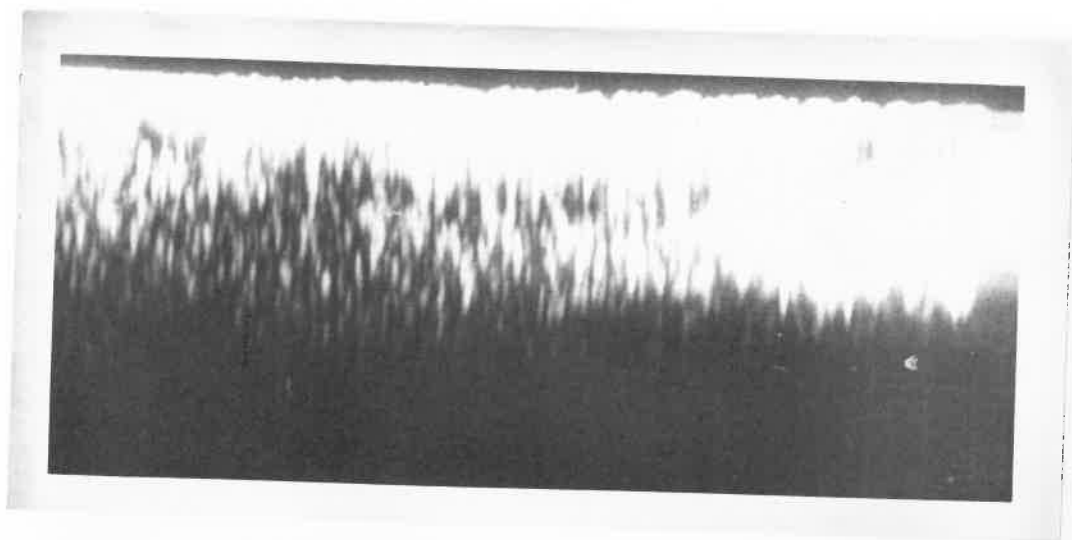


Figure 3.9.3

Radio echo record obtained on the Jøstedalsbreen, Norway, using a sledge mounted Mark 2 sounder. The bottom echo is 40 dB over noise but it is lost in the scattered echoes at a depth of about 150 m .

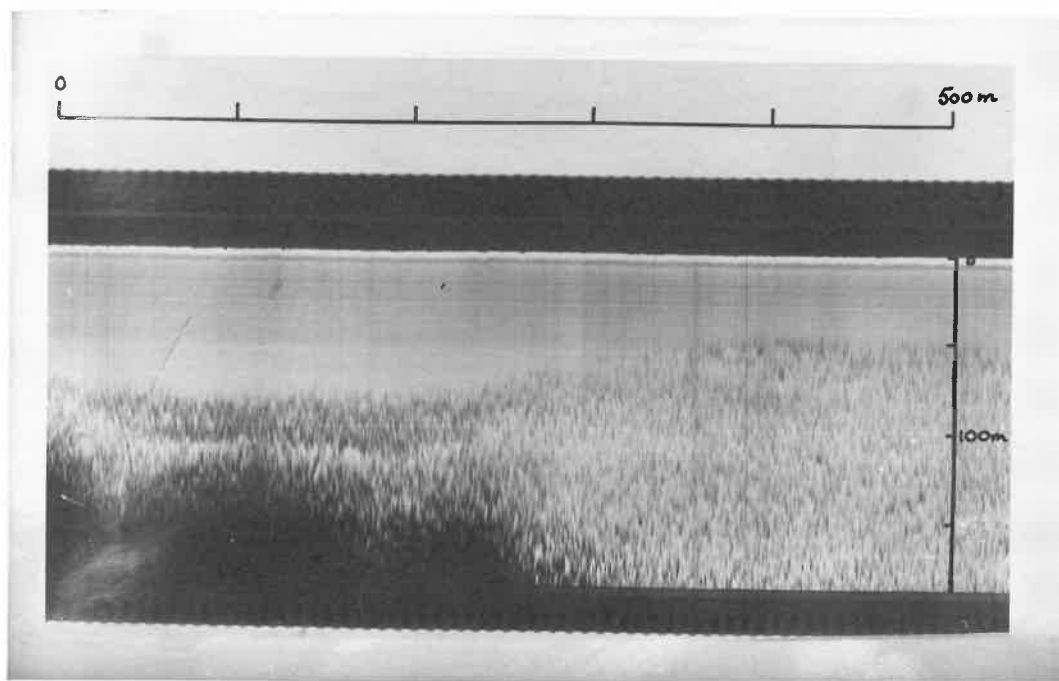


Figure 3.9.4

Radio echo record obtained on the Hardangerjøkul, Norway, by S. Evans using a 480 MHz sounder on the surface. The bottom echo on the left is at a depth of 100 m and is lost in the scatter echoes to the right.

## CHAPTER 4

Field work4.1 Radio echo sounding of the Antarctic ice sheet, 1967

Applications of the principle of radio echo sounding as a method of measuring ice thickness, are catalogued by Evans (1966). References to more recent work may be found in the symposium by Evans et al (1969).

Following successful radio echo soundings during an oversnow vehicle traverse in north-west Greenland in 1964, reported by Bailey, Evans and Robin (1964), and the first continuously recording airborne soundings in Ellesmere Island in 1966, reported by Evans and Robin (1966), the group at the Scott Polar Research Institute were invited to co-operate with the United States National Science Foundation and undertake sounding of the Antarctic ice sheet from long range aircraft of the U.S. Navy Air Development Squadron Six. This programme was carried out on a trial basis in December 1967 over a wide range of conditions of the Antarctic ice sheet. Prior to this, the British Antarctic Survey, using an SPRI Mark 2 system, carried out a successful survey in light aircraft around the southern part of the Antarctic Peninsula in December 1966 to February 1967 as reported by Swithinbank (1968) and referred to in section 4.4.

The equipment was installed in a Lockheed C121-J Super Constellation and preliminary trials were carried out in Christ-

church, New Zealand with the help of my supervisor, S. Evans. The field programme was carried out by G. de Q. Robin, C.W.M. Swithinbank, and the author, who was responsible for the equipment in the field.

Two complete Mark 2 echo sounders were installed in the aircraft together with two SFIM flight recorders (see chapter 5). Figure 4.1.1 shows the console of equipment inside the aircraft. The aerial system consisted of two 6 m folded terminated dipoles which were suspended a quarter wavelength ( $\approx 2$  m) beneath the horizontal stabilizer. A balanced feeder connected the aerial to a balun and impedance matching unit inside the aircraft skin, and a coaxial cable led from there to the radio echo console. Figure 4.1.2 shows a view of the aerial system. This aerial exhibited very good electrical characteristics. The impedance bandwidth was such that the transmitted pulse was not visibly distorted and ringing in the cables did not occur. The absolute gain of the aerial was measured by reflection from a calm sea when flying at a known height. The polar diagram was evaluated by flying at a variety of bank angles. This was only possible in the rolling plane, pitching could not be maintained at large enough angles. Figure 4.1.3 shows the polar diagram measured in the rolling plane when using both aerials in parallel for transmission and reception. Also shown, normalized to the same absolute gain, is the polar diagram of the single terminated dipole

used in the Antarctic Peninsula on a different aircraft (see section 4.4). The favourable electrical characteristics of this aerial system were offset by the poor mechanical behaviour. In order to achieve a narrow beam width in the rolling plane, to facilitate deconvolution as described in chapter 1, the dipoles were mounted transversely and, unfortunately, in the slip-stream of the engines. The stresses on the aerial caused frequent breakages. Fortunately, since there were two aerials, radio echo sounding continued using only one when a break occurred. Nevertheless, much time was wasted in repairing the aerial system. The mechanical properties of subsequent installations have been improved, but it has not been possible to repeat the electrical properties on other aircraft, probably because the construction of the aircraft has not permitted the dipoles to be mounted a quarter of a wavelength below a plane reflector.

The problems of receiver saturation mentioned in chapter 1, frequently made it necessary to suppress the receiver during the period of the returning strong surface echo to avoid loss of sensitivity to the bottom echo. The terrain clearance was then found using a microwave radio altimeter. The signal from this was recorded on the SFIM flight recorder and the data subsequently collated with the radio echo data.



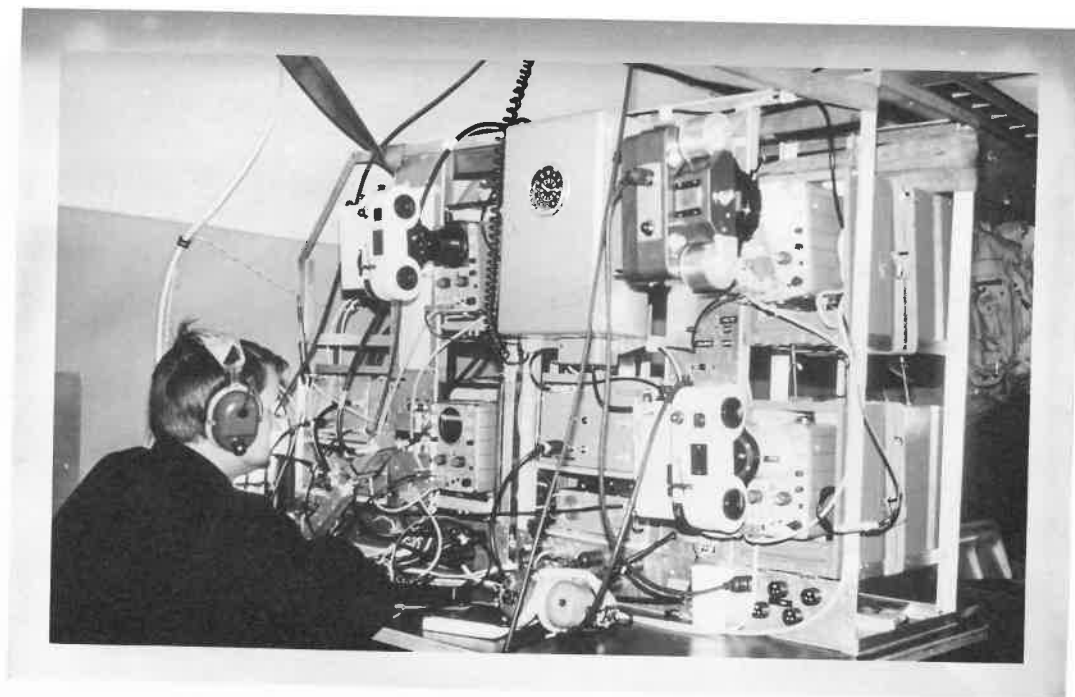


Figure 4.1.1

The installation of two Mark 2 radio echo sounders in the cabin of a Lockheed C121-J Super Constellation aircraft.



Figure 4.1.2

Two terminated dipoles mounted beneath the horizontal stabilizer of the Super Constellation aircraft.

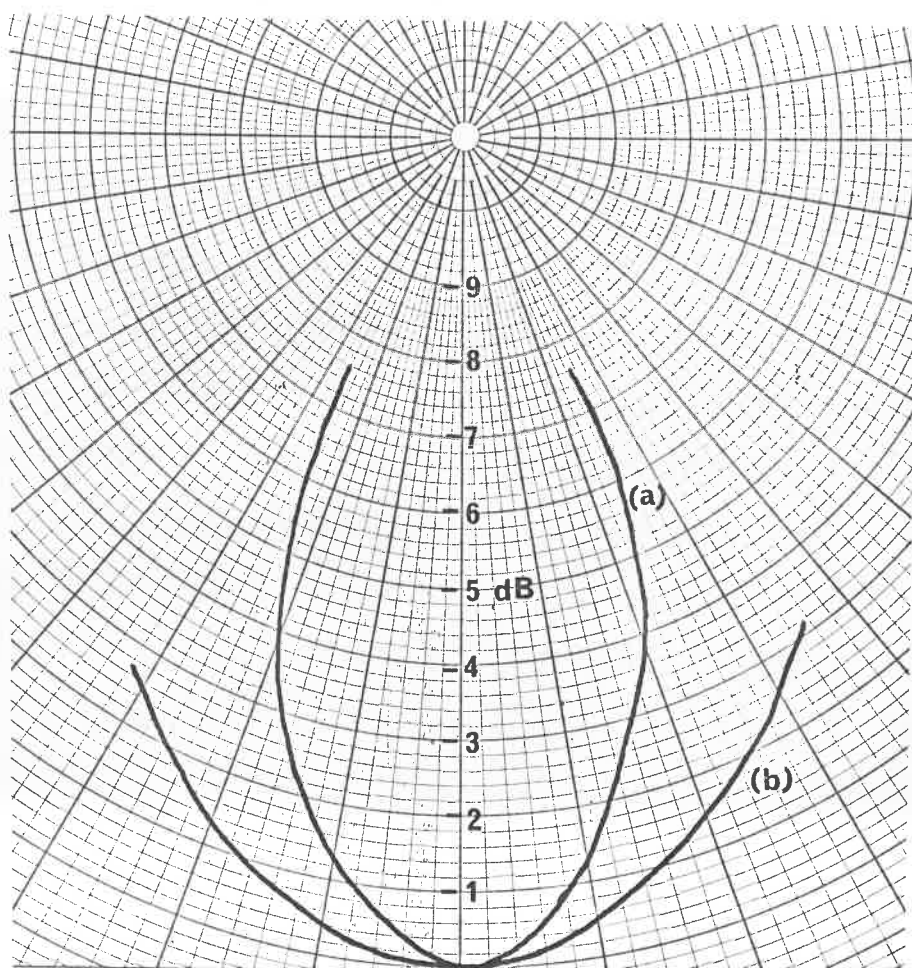


Figure 4.1.3

The normalized polar diagram in the Velling plane.

(a) The aerial pair on the C121-J (  $G_o = +4.5$  dB)

(b) The single aerial on the DHC-6 (  $G_o = -8.5$  dB)

#### 4.2 Results of the 1967 Antarctic season

The flying programme in December 1967 was intended primarily to assess the performance of the system under a wide variety of conditions in the Antarctic. The Super Constellation was not equipped with skis and could only use the sea ice runway at McMurdo Station (latitude  $77^{\circ}51'$  S, longitude  $166^{\circ}40'$  E). It was not possible to land at any other station, so that all flights began and ended at McMurdo. The aircraft was fitted with an internal fuel tank which permitted flights to last more than 12 hours (more than 4000 km). The map in figure 4.2.1 shows the flight lines which total about 36,000 km.

Measurements of ice thickness were compared with previous measurements using seismic techniques wherever possible. The errors in navigation made precise comparison impossible.

Measurements made over the Ross Ice Shelf agreed with those of Crary et al (1962). Thickness increased rapidly from approximately 200 m at the ice front to about 300 m at 10 km from the ice front. Thereafter depths of 300 to 500 m were found over much of the main area of the ice shelf. A contour map of ice thickness, based on the radio echo measurements using Cole's algorithm (see chapter 6), is shown in figure 4.2.2. It may be inferred from the contour map that Western Byrd Land contributes more ice to the shelf than the glaciers of the Transantarctic Mountains. Towards the south eastern corner thickness increased

to a maximum of 1300 m. Roosevelt Island (latitude  $80^{\circ}$  S longitude  $163^{\circ}$  W) is an ice rise in the Ross Ice Shelf that rests on rock which is below sea level. Ice thickness exceeded 800 m in the centre of the island. In general, the ice between Roosevelt Island and western Byrd Land was thicker than in the rest of the ice shelf. There were no difficulties in obtaining strong bottom echoes over most of the Ross Ice Shelf, the only exception being near to the mouths of some of the glaciers through the Transantarctic Mountains. Collins and Swithinbank (1969) have described in detail the rifts at the foot of the Beardmore Glacier where brine is able to well up and contaminate the ice. Contamination by brine is the probable cause of the loss of bottom echo.

Radio echo measurements in western Byrd Land show ice which has a high bottom reflection coefficient (suggesting water at the base) and a smooth surface (suggesting that it is afloat). The surface elevations found, are too high for the ice to be floating on the sea, and Robin, Swithinbank and Smith (1969) have suggested the existence of a pseudo ice shelf which is floating on water not connected to the sea.

At Byrd Station (latitude  $80^{\circ}1'$  S  $119^{\circ}32'$  W) measurements in the vicinity of the station were between 2104 m and 2224 m which should be compared to the depth of 2164 m found by drilling to bedrock (Gow et al 1968).

At Vostok Station (latitude  $78^{\circ}27'$  S longitude  $106^{\circ}40'$  E),

a seismic depth of 3700 m (Kapitza 1960) compares with a radio echo depth of between 3760 and 3810 m. At Sovetskaya, west of Vostok, we measured 4200 m of ice (the greatest depth measured). An earlier seismic measurement gave a value of 1830 m which may be a misinterpretation of an intermediate echo.

Radio echo records obtained by the author in 1967 frequently show echoes from internal layering, particularly in areas of thick ice. These usually follow the pattern of the bedrock suggesting a laminar flow of the ice over its base. The reflections are caused by some discontinuity of intrinsic impedance which may be due to density variations or perhaps different crystal orientations.

Robin, Swithinbank, and Smith (1969) have compared the observed echo attenuation with the attenuation predicted from assumed equilibrium temperature gradients within the ice. The agreement indicates that the assumed temperature gradients are approximately correct and therefore the ice is in equilibrium. The paper also interprets vertical lines which are sometimes seen amongst horizontal layering as evidence of deep seated shearing. Harrison (1971) has shown that vertical features in nature could not produce a vertical line on the radio echo record but that focussing by gently curved horizontal layers could produce the apparently vertical lines.

During the 1969-70 season, while the author was working in the Antarctic Peninsula, the cooperation between the Scott Polar Research Institute and the U.S. National Science Foundation continued with

radio echo sounding from a C 130 Hercules aircraft as reported by Evans and Smith (1970). A total of 330 hours flying time was devoted to this project and the results are presently under investigation.

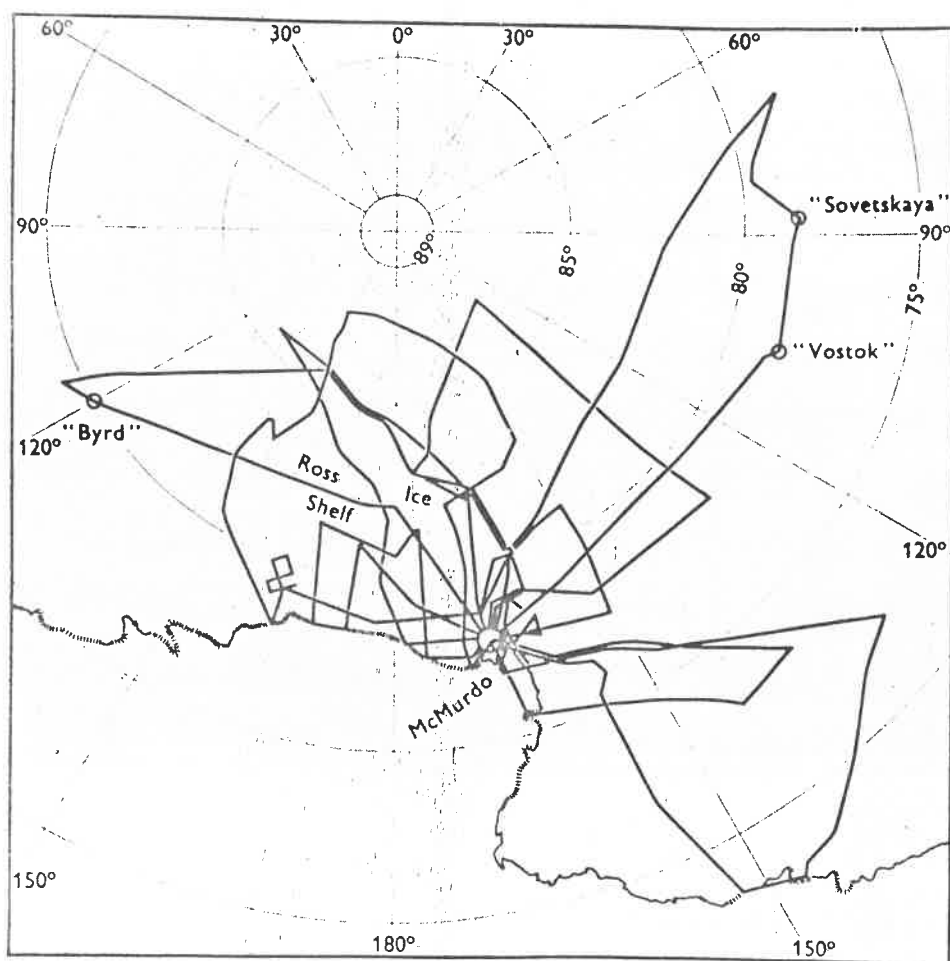


Figure 4.2.1

Flight lines of radio echo sounding missions, 1967.



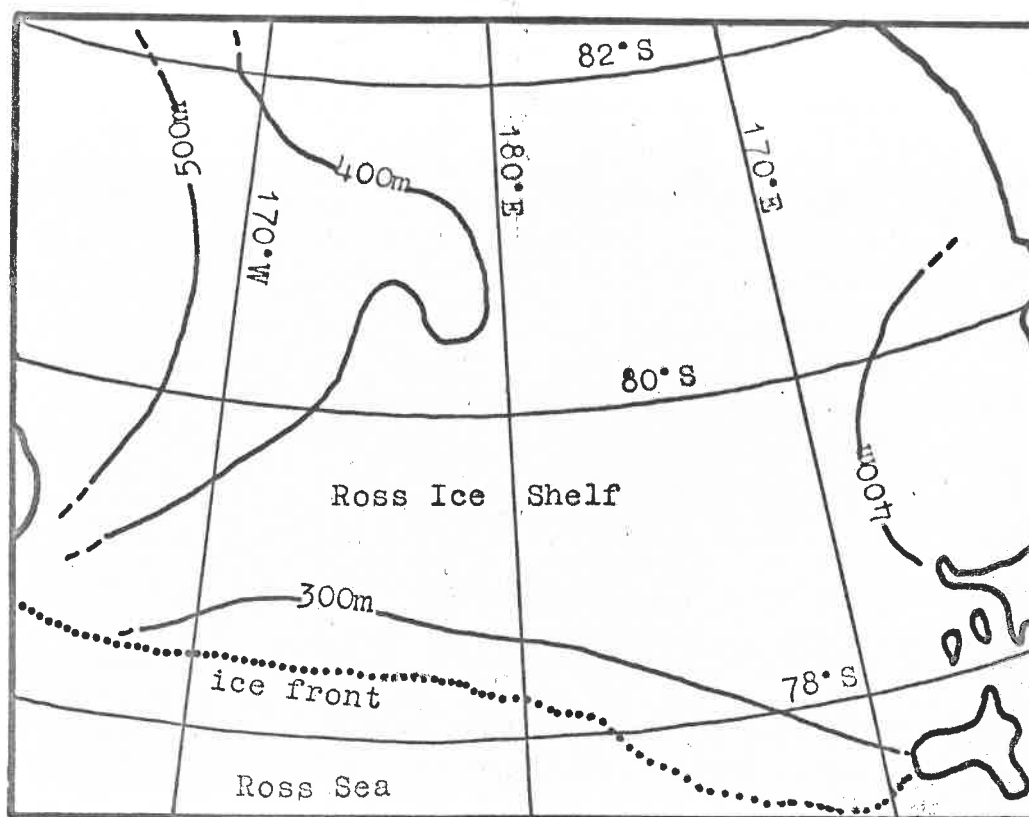


Figure 4.2.2

Ice thickness contours for part of the Ross Ice Shelf from measurements by the author in 1967. The interpolation was made using Cole's algorithm. (Ch.6)

#### 4.3 Temperate glacier experiments

The Mark 2 equipment described in chapter 1 was intended primarily for use in polar regions. Temperate glaciers in other regions are likely to have somewhat different properties from glaciers in the Arctic and Antarctic. For this reason, T.M. Randall and the author conducted some investigations on temperate glaciers in Norway with a view to designing a modified radio echo sounder (designated Mark 3) which would be specially adapted to temperate glacier measurements.

In chapter 3 we considered some of the factors which affect the strength of the received echo. During the period spent in Norway, we were most aware of the problems of absorption at high ice temperatures and interference from surface features. Using a 35 MHz echo sounder it is difficult to produce a narrow beam aerial which is easily portable, and we were aware that on glaciers only a kilometre wide, there would be strong echoes from adjacent rock exposures and other features.

Jostedalsbreen (latitude  $61^{\circ}30'$  N longitude  $7^{\circ}$  E) was chosen for preliminary experiments in May 1968. The experiments were conducted with the cooperation of G. Østrem and the Norwegian Water Resources and Electricity Board. The equipment was airlifted on to the glacier and mounted on two small sledges. One sledge carried the radio echo sounder and the transmitting aerial, and the other sledge carried the receiving aerial. Both aerials were

of the terminated folded dipolar type, as described in chapter 1. The aerials were mounted in-line in an attempt to reduce the coupling between them to a minimum. Figure 4.3.1 shows the equipment in position. A lead-acid accumulator provided power for the equipment, and a 'Ski Doo' motor toboggan was available to pull the sledges. It is unfortunate that the sledges were too small to allow an operator to watch the oscilloscope monitor while travelling. When the equipment was stationary, echoes were visible at plausible ranges but when the film record was processed and studied, it could be seen that the echoes were in a random pattern, and a continuous bottom echo could not be discerned. Figure 3.9.3 shows an example of the records obtained. A few echoes were interpreted as coming from the bedrock, but nowhere were these beyond doubt. At the time, the significance of scattered echoes from within the body of the ice was not realized, and oblique echoes from surface features were blamed for the failure to distinguish bottom echoes. Echoes which were received from bedrock were attenuated by an amount characteristic of ice at the melting point, so that at the time another mechanism was not sought to explain the problems.

After the somewhat inconclusive results obtained on the surface of Jostedalsbreen, it was decided to attempt measurement from the air, and a convenient glacier for this was Folgefonni (latitude  $60^{\circ}$  N longitude  $6^{\circ}30'$  E). The echo sounder was mounted

in a Cessna 185 aircraft, obtaining power from the aircraft supply. The aerial was a terminated folded dipole as before, but only one could be fitted, and this was used for transmission and reception. It was rather close to the fuselage and wings, so that the impedance match was probably poor. Since attenuation was not the over-riding cause of failure on the surface, a 3 dB fixed attenuator was included in the aerial cable to improve the impedance match - to suppress ringing in the cables. This attenuator reduced the system performance by 6 dB. Measurements of echo strength over the sea indicated that the aerial gain was usable, but a precise measurement could not be made because an accurate measure of height was not available. The author obtained a large number of profiles over the ice cap, but none show definitely a bottom echo clear of random echoes. The geometry of the ice cap is such that oblique echoes from nearby rock outcrops could be ignored, but nevertheless random echoes prevented the bottom echo from being distinguished. It is now clear from the calculations in chapter 3 that scattering from inhomogeneities within the ice probably give rise to these undesirable echoes, but at the time oblique echoes from a rough surface were held to be the cause.

The Mark 3 equipment was built using a carrier frequency of 480 MHz but was otherwise similar to the Mark 2 version. The new equipment was tested the following season on Hardangerjøkull, Norway during the spring of 1969 by S. Evans (private communication).

In spite of an aerial system which should not have given rise to oblique echoes from the surface, the random echoes shown in figure 3.9.4 were obtained. It was then thought that the frequency was too high and absorption was becoming important, so that a change was made to a carrier frequency of 144 MHz. Again, field work by S. Evans in Norway failed to obtain more satisfactory results. In retrospect, it is clear that the difficulties arose from scattered echoes from within the ice and not from oblique surface echoes. The calculations of chapter 3 force us to the conclusion that temperate glaciers having the inhomogeneities which we postulate, can only be successfully sounded by an equipment which illuminates a minimum volume of the ice while retaining a low frequency. At present, these conflicting requirements continue to thwart attempts made by J.L. Davis (private communication) to measure glacier thickness with a version of the Mark 3 equipment using a frequency of 60 MHz and a directional aerial. A frequency as low as 6 MHz with all its disadvantages may yet prove to be the only solution to this problem. Included in the table in figure 1.7.1 is a radio echo sounder which the author suggests should be more successful in sounding temperate glaciers when scattering from inhomogeneities is the reason for undetected bottom echoes. Using a low carrier frequency ( 6 MHz ) and a bandwidth of 1 MHz, a pulse length of  $1 \mu$  S may be obtained. If the aerial is no better than an elementary dipole, the 'scattering index' defined in chapter 1 is very much

improved compared to the Mark 3 echo sounders which have yet been devised. Although the terrestrial noise levels in this frequency band are very high, the noise will not be coherent with the transmitted pulse and it should be possible to integrate the received signal for a time long enough to distinguish the bottom echo.



Figure 4.3.1

The Mark 2 radio echo sounder mounted on a light sledge used by the author on the Jøstedalsbreen, Norway.

#### 4.4 Antarctic Peninsula radio echo sounding - 1969-70

Earlier airborne sounding in the Antarctic Peninsula in 1966-67 using a Mark 2 radio echo sounder was described by Swithinbank (1968). The 1969-70 season was the first in which a Mark 4 radio echo sounder was used and, in addition, the author used improved navigational instrumentation as described in chapter 5.

There was no successful sounding from the surface during this season because of adverse travelling conditions in George VI Sound where it was hoped to conduct a local survey. The equipment was installed in a DHC-6 Twin Otter aircraft (No 152) at Adelaide Station (latitude  $67^{\circ}46'$  S longitude  $68^{\circ}54'$  W) during December 1969. The equipment console occupied the space of one passenger seat on the right of the cabin in figure 4.4.1. On the left of the cabin there was an auxiliary fuel tank used to increase the range of the aircraft. The console consisted of the radio echo sounder together with the recording and monitoring oscilloscopes and beneath the console the SFIM flight recorder which was used to record flight parameters for track plotting. The aerial system was a single 6 m long folded terminated dipole, centred on an impedance matching unit fixed to the belly of the aircraft. The impedance matching unit contained a network that allowed the aerial to be fed from a 50 ohm coaxial cable, and also the terminating load resistor. Nylon cord joined the ends of the dipole to the tips of two 1 m steel aerial masts which were supplied by DeHavilland Aircraft of



Canada and which extended down from the wing tips as shown in figure 4.4.2. There was no discernable drop in aircraft performance with this arrangement and the system was mechanically reliable. The 3 dB beamwidth of the aerial was 30 degrees in the rolling plane. The polar diagram is shown in figure 4.1.3. Directivity in the pitching plane was not measured. The gain of the aerial measured by reflection from a calm sea surface was about -10 dB. This rather low figure may be explained by the proximity of the skis and airframe. A conducting surface contains an antiphase image which opposes radiation from an aerial which is less than a quarter wavelength away; consequently more power is dissipated in the terminating resistor at the expense of the radiated wave. Breakages occurred when this type of aerial was used on a Lockheed Super Constellation in 1967 as reported in section 4.1, but there were no problems with the slower Twin Otter aircraft. Electrical power for the equipment (28 volts, 4 amps DC) was obtained from the aircraft's 28 volt DC electrical system. The pitot and static air pressure signals for the SFIM flight recorder were obtained from the standard aircraft pitot tube by means of Tee-pieces supplied by DeHavilland. The air temperature was measured by means of a sensing element fitted by DeHavilland in the belly of the aircraft. Directional information was provided by a gyro stabilized magnetic compass giving a synchro output signal. The output was converted to a signal suitable for the flight recorder by means of an SE

Laboratories synchro-DC converter. The terrain clearance height of the aircraft was obtained from the radio echo record. An intercom system was installed to allow all three crew members (pilot, glaciologist/navigator and radio echo operator) to converse freely.

Flight lines were planned in advance, but the absence of weather data for places away from occupied stations usually necessitated in-flight revision. The flight duration was generally limited by factors such as the uncertainty of terminal weather or of communications rather than by the endurance of the aircraft. Depending upon loading and altitude, the maximum endurance was about five hours. Most flights lasted between two and four hours, representing a maximum range of about 900 km.

It was usual to fly at 1000 m above terrain, this altitude being a good compromise between loss of surface echo when the aircraft was low and loss of bottom echo due to confusion with echoes from distant oblique surface features when the aircraft was high. The surface echo was lost if the transient signals caused by the transmitted pulse had not decayed to a sufficiently low level by the time that the surface echo returned. The critical level depended upon the receiver gain in use. When bottom echoes were strong then the receiver gain would be reduced to make it insensitive to the transient signals. This allowed the surface to be resolved if the aircraft was flying at 500 m terrain clearance. In general

the lower terrain clearance was only required when the surface was rough or badly crevassed and oblique echoes from the surface obscured the bottom echo. When conditions were favourable, as they were over smooth ice shelves, it was possible to fly at 2500 m in the interests of fuel economy.

One of the duties of the glaciologist/navigator was to note, whenever possible, the position of the aircraft on a map, using visual recognition of features close to the track of the aircraft. At the same time a mark was made on the flight recorder trace to allow collation with flight parameters and the radio echo record. Maps published by the Directorate of Overseas Surveys at scales of 1:200 000 and 1:500 000 were used. The accuracy of the available sheets was very variable and in un-surveyed areas positions may be in error by up to 15 km. The track obtained was therefore correct only in relation to the available mapping. The misclosure of the dead reckoning track was due to a combination of wind drift and errors in measurement of the flight parameters. The absolute distance depended on the time between fixes, but expressed as a rate of drift the misclosure was typically  $5 \text{ m sec}^{-1}$ . The magnitude of the error in the corrected track depended upon the frequency of fixes, which in turn depended upon the abundance of mapped surface features. In areas such as the centre of the Antarctic Peninsula plateau and the centre of the Larsen Ice Shelf which lack mapped surface features, the computed track may be in

error by more than 10 km. In well mapped areas such as George VI Sound, the computed track may be expected to be within 1 km of the actual track as it would appear on the available mapping. The photographic records produced by the radio echo sounder (35 mm film) and the flight recorder (60 mm paper) were processed at Adelaide Station.



Figure 4.4.1

The interior of the Twin Otter aircraft, looking towards the cockpit. On the right of the cabin is the radio echo console, on the left an auxiliary fuel tank.



Figure 4.4.2

The exterior of the Twin Otter aircraft, showing one of the 1 m aerial support poles beneath the end of the wing. From the bottom of the pole, part of the aerial may be seen leading to the impedance matching unit beneath the fuselage.

#### 4.5 Results of the 1969-70 Antarctic Peninsula season

Flights were made from both Adelaide Station and Fossil Bluff (latitude  $71^{\circ}20'$  S longitude  $68^{\circ}17'$  W). They extended over all accessible areas between latitudes  $66^{\circ}$ S and  $74^{\circ}$ S and between longitude  $60^{\circ}$ W and  $75^{\circ}$ W. Figure 4.5.1 shows flights made during the work reported here together with those on which bottom echoes were obtained by Swithinbank during the 1966-67 season. It can be seen that tracks included the Larsen Ice Shelf, a large iceberg in the Weddell Sea, the Wordie Ice Shelf (where some detail is omitted in figure 4.5.1), Wilkins Sound, George VI Sound, the Fuchs Ice Piedmont, the mainland plateau region, and the ice covered Biscoe Islands.

On figure 4.5.2 an ice rise is mapped to the east of the Hollick-Kenyon Peninsula in  $68^{\circ}30'$  S  $61^{\circ}$ W. This is an ice covered island which was sounded and appears similar to Hearst Island to the south. Wilkins (1929, p.374) reported seeing an ice covered island somewhere in this area during one of his early flights, but he was uncertain of his position at the time. Ronne (1948, p.366) flew over the area in good visibility in order to check Wilkins' observation but he failed to see it and must have flown to the south. He suggested that Wilkins was deceived by a low cloud formation on the ice shelf but the radio echo profile of the ice rise in figure 4.5.3 shows that Wilkins was correct.

Soundings were most successful on ice shelves. On the Larsen

Ice Shelf, soundings were almost continuous except for a few scattered areas where echoes were not obtained. These areas were invariably in the vicinity of rifts in the ice shelf and usually coincided with a reflecting layer at about sea level. An example is shown in figure 3.5.2. This situation predominated south of latitude  $68^{\circ}30'$  S. Our considerations in section 3.5 suggest that quite thin layers of brine infiltration in the porous firm layers at sea level, will explain these observations. In these areas, only a very large increase in the attenuation index (system performance) will yield bottom echoes.

The surface of the Wordie Ice Shelf was very disturbed. Severe crevassing often prevented successful sounding because oblique echoes from the surface obscured the bottom echo, but some measurements were possible and thicknesses from 150 m to more than 400 m were in good agreement with those found by Swithinbank and Petrie who studied this Ice Shelf in more detail. No normal bottom echoes were obtained on the Wordie Ice Shelf west of longitude  $67^{\circ}50'$  W either by the author or by Swithinbank. It appears that this meridian divides the crevassed eastern part from the rifted western part. The distinction between rifts and crevasses is that rifts extend to the bottom of an ice shelf and allow brine to well up and infiltrate the ice at sea level, thus preventing sounding to the bottom, whereas crevasses do not.

On Wilkins Sound, bottom echoes were obtained in relatively



few places. Elsewhere, a reflecting layer at sea level appeared and no bottom echo was received. The apparent thickness changed so abruptly from about 200 m to about 50 m without any detectable change in surface elevation that, if the ice is in hydrostatic equilibrium, the thickness change cannot be real and once again it must be supposed that brine has infiltrated at sea level.

In spite of extensive surface meltwater pools on George VI Sound, no difficulty was encountered in measuring thicknesses over the whole ice shelf up to a maximum of almost 500 m near latitude  $73^{\circ}\text{S}$  longitude  $70^{\circ}\text{W}$ . As we saw in section 3.4, melt water layers 0.5 m deep contribute only 10 dB to the attenuation of the bottom echo and this extra loss would not normally prevent detection of the bottom echo on a floating ice shelf. Measurements of the received echo strength indicated an attenuation of 3.8 dB per 100 m in latitude  $70^{\circ}15' \text{ S}$  longitude  $68^{\circ}30' \text{ W}$  and 2.9 dB per 100 m in latitude  $73^{\circ}\text{W}$  longitude  $70^{\circ}\text{W}$ . These measurements are characteristic of an average ice temperature of about  $-5^{\circ}\text{C}$  in the north and  $-10^{\circ}\text{C}$  in the south (Robin, Evans and Bailey 1969, p. 476).

The relatively high mean annual temperature of the Fuchs Ice Piedmont on Adelaide Island and the probable existence of ice lenses, explain the difficulty in measuring ice thickness there. The only reliable measurements obtained were within a few kilometres of the southern end of the island in the vicinity of Adelaide Station as shown in figure 3.9.2. Here measurements up to 250 m

indicated that the bedrock inland from the station was close to sea level for at least 5 km. The echo strengths obtained indicated an attenuation of 4.8 dB per 100 m path in ice, corresponding to an average ice temperature of about  $-2^{\circ}\text{C}$ . The mean annual air temperature at this point is about  $-6^{\circ}\text{C}$ . The 10 m temperature is likely to be higher than the mean annual temperature because of some surface melting and the bottom of the ice is probably at the melting point.

The Biscoe Islands can be expected to have similar properties to the Fuchs Ice Piedmont, and a similar difficulty was experienced in receiving bottom echoes. Nevertheless thicknesses up to 270 m were recorded on the largest member of the group, Renaud Island.

Linton (1964) suggests that the subglacial topography of the Antarctic Peninsula plateau is essentially the pre-glacial surface having 'smooth aspect and modest relief' uplifted to about 1200 metres above sea level. Radio echo measurements indicate that this figure of 1200 metres above sea level is typical for the bedrock beneath the plateau. However, there appears to be somewhat more relief than Linton expected as shown in figure 4.5.4. Either the residual relief of the pene-plain from which the plateau was derived was greater than the 300 - 500 m that Linton suggests, or subsequent erosion has had more effect on the plateau region than he supposed. The greatest reliable ice thickness measured was 1630 m in latitude  $70^{\circ}\text{S}$  longitude  $67^{\circ}\text{W}$ .

The data obtained by the author together with the measurements by Swithinbank in 1966-67, are to be published in full by Ewensmith (1971). In addition, contours of ice thickness have been deduced from the data for George VI Sound (figure 4.5.5), Wordie Ice Shelf (figure 4.5.6) and Larsen Ice Shelf (figure 4.5.7). Contours were obtained using the author's algorithm described in chapter 6. Reference to the chart of the data points will indicate the reliability of the contours.

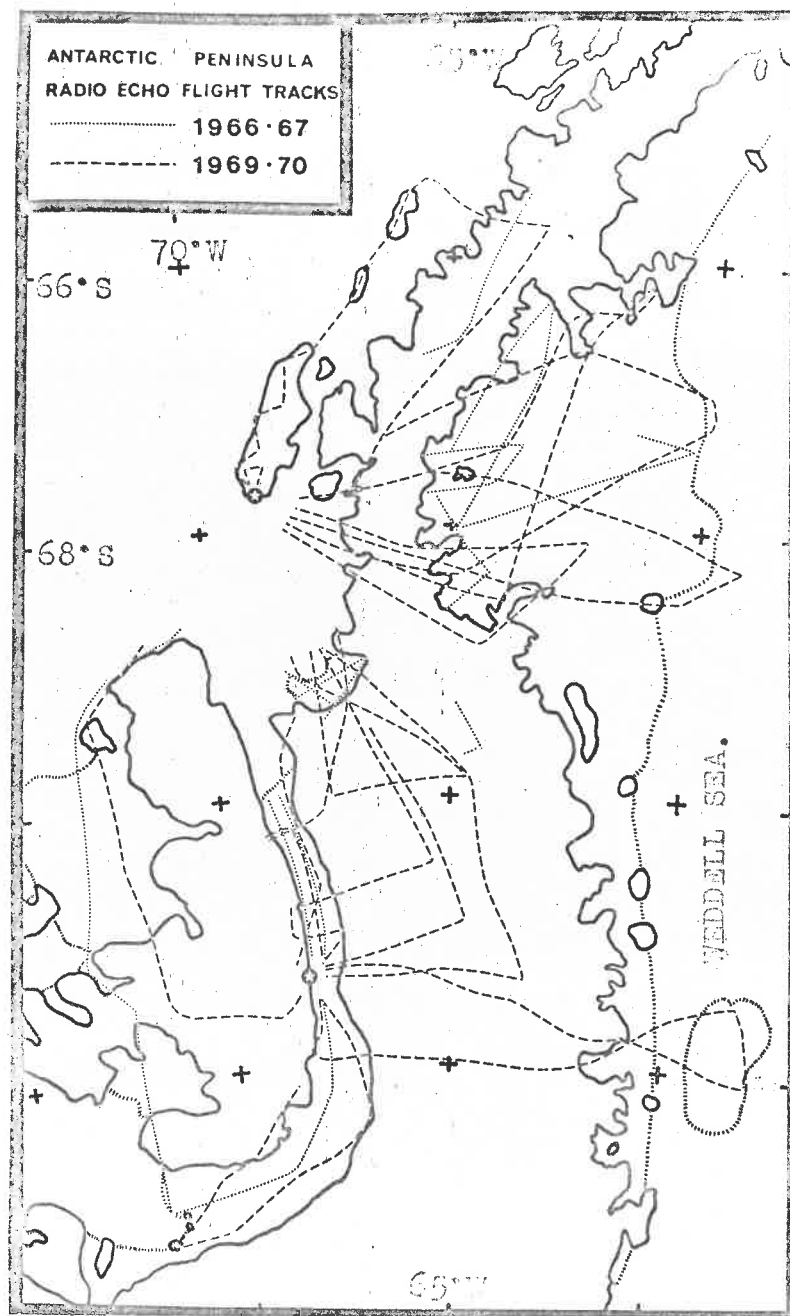


Figure 4.5.1

Flight lines of radio echo sounding missions in the Antarctic Peninsula, 1969-70. Also shown are parts of the 1966-67 flight lines on which echoes were obtained.

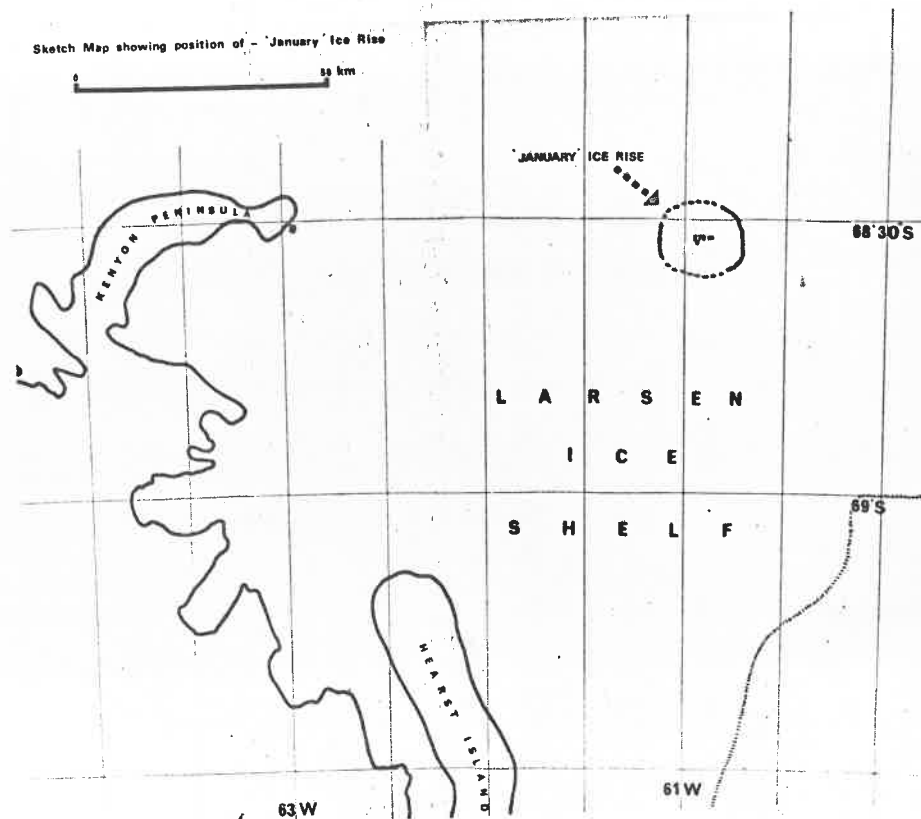


Figure 4.5.2

Sketch map showing the position of 'January' Ice Rise, an ice rise of  $200 \text{ km}^2$  found by the author.

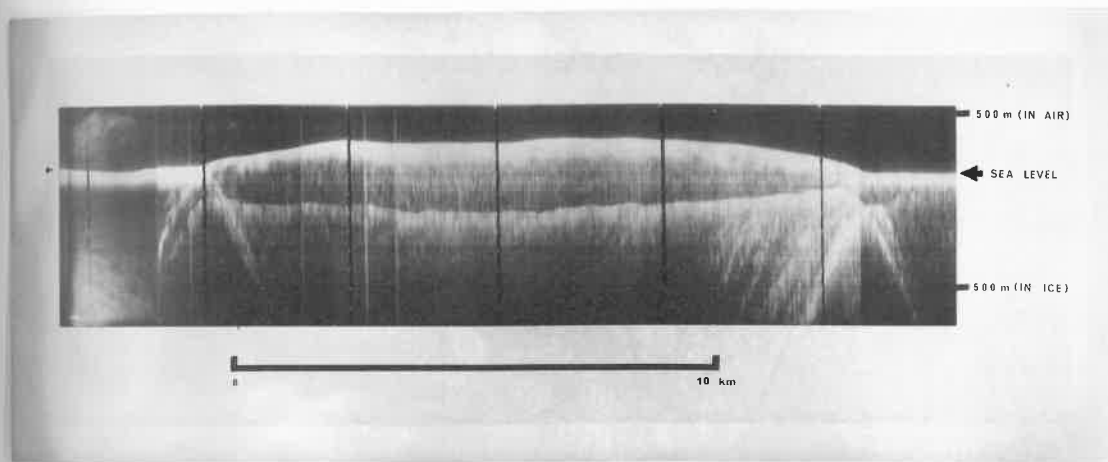


Figure 4.5.3

An east-west cross sectional profile of the 'January' ice rise (lat.68°30'S. long.61°W). The surface elevation rises to about 270 m above sea level and the maximum ice thickness is about 320 m.

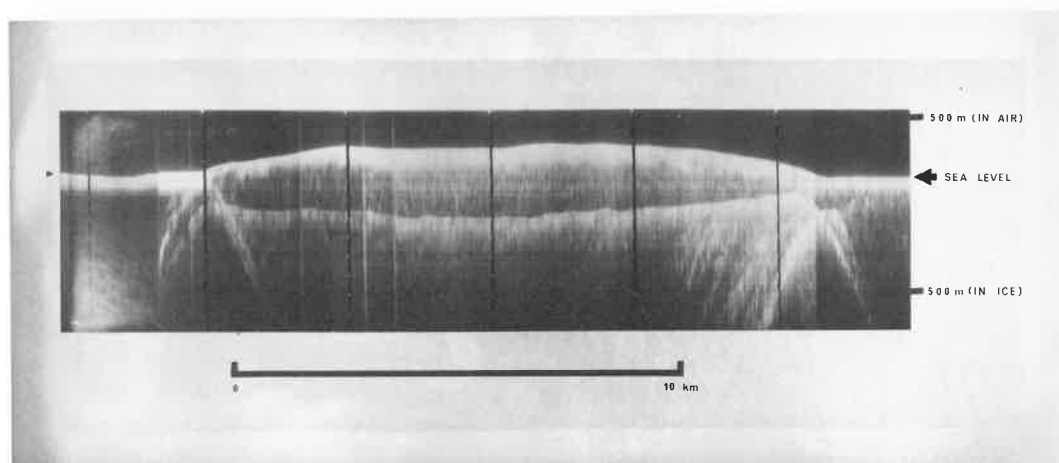


Figure 4.5.3

An east-west cross sectional profile of the 'January' ice rise (lat.  $68^{\circ}30'S$ . long.  $61^{\circ}W$ ). The surface elevation rises to about 270 m above sea level and the maximum ice thickness is about 320 m.

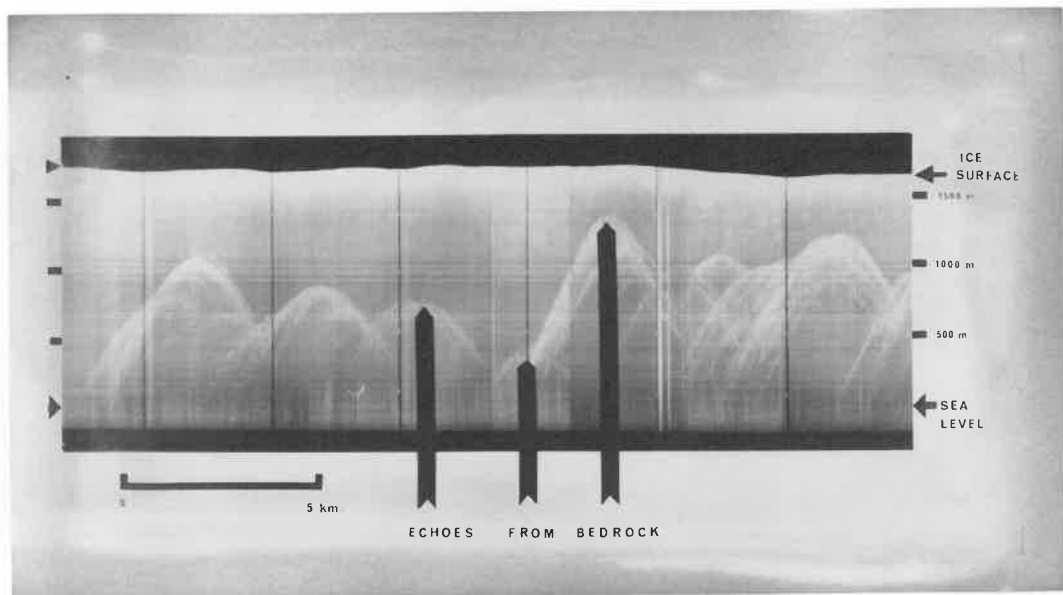


Figure 4.5.4

An example of a radio echo record obtained in latitude  $70^{\circ}\text{S}$ , longitude  $66^{\circ}\text{W}$ . Bedrock elevations may be seen to vary from 400 to 1300 m above sea level. The shape of the topography is not represented exactly because of the wide beam aerial, but the relief is almost 1000 m.



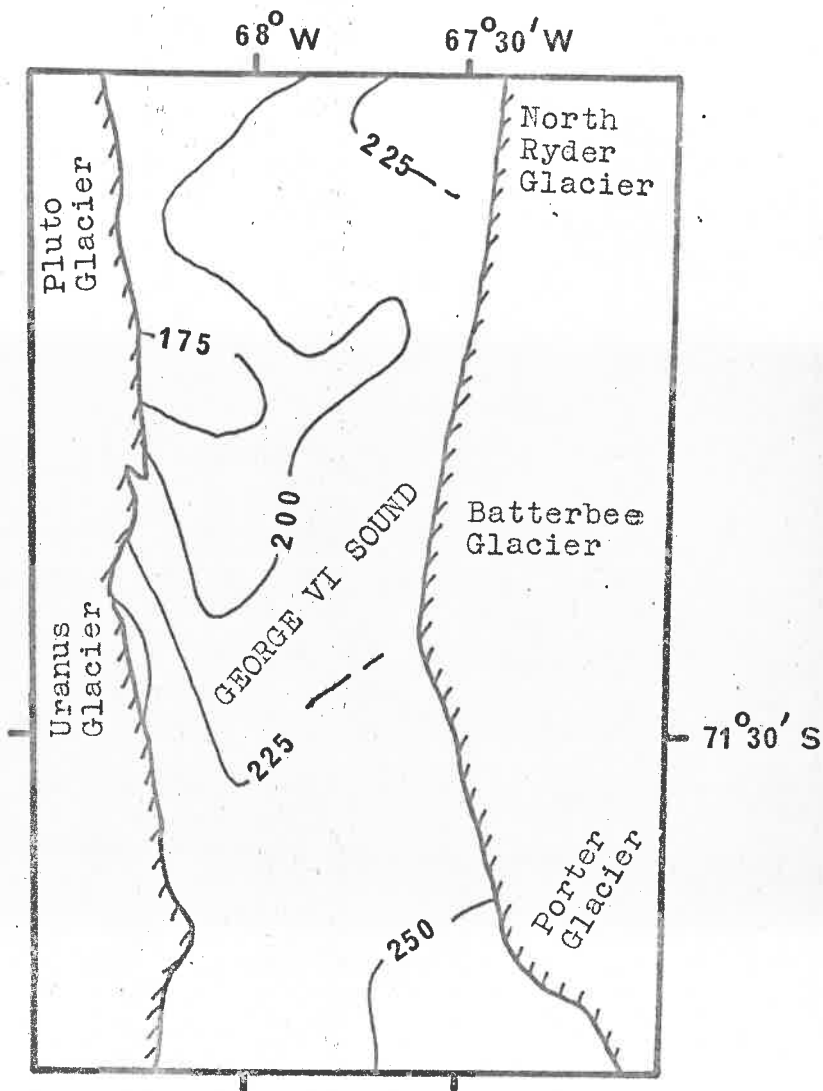


Figure 4.5.5

Contours of ice thickness in the Fossil Bluff region of George VI Sound. The contour interval is 25 metres.

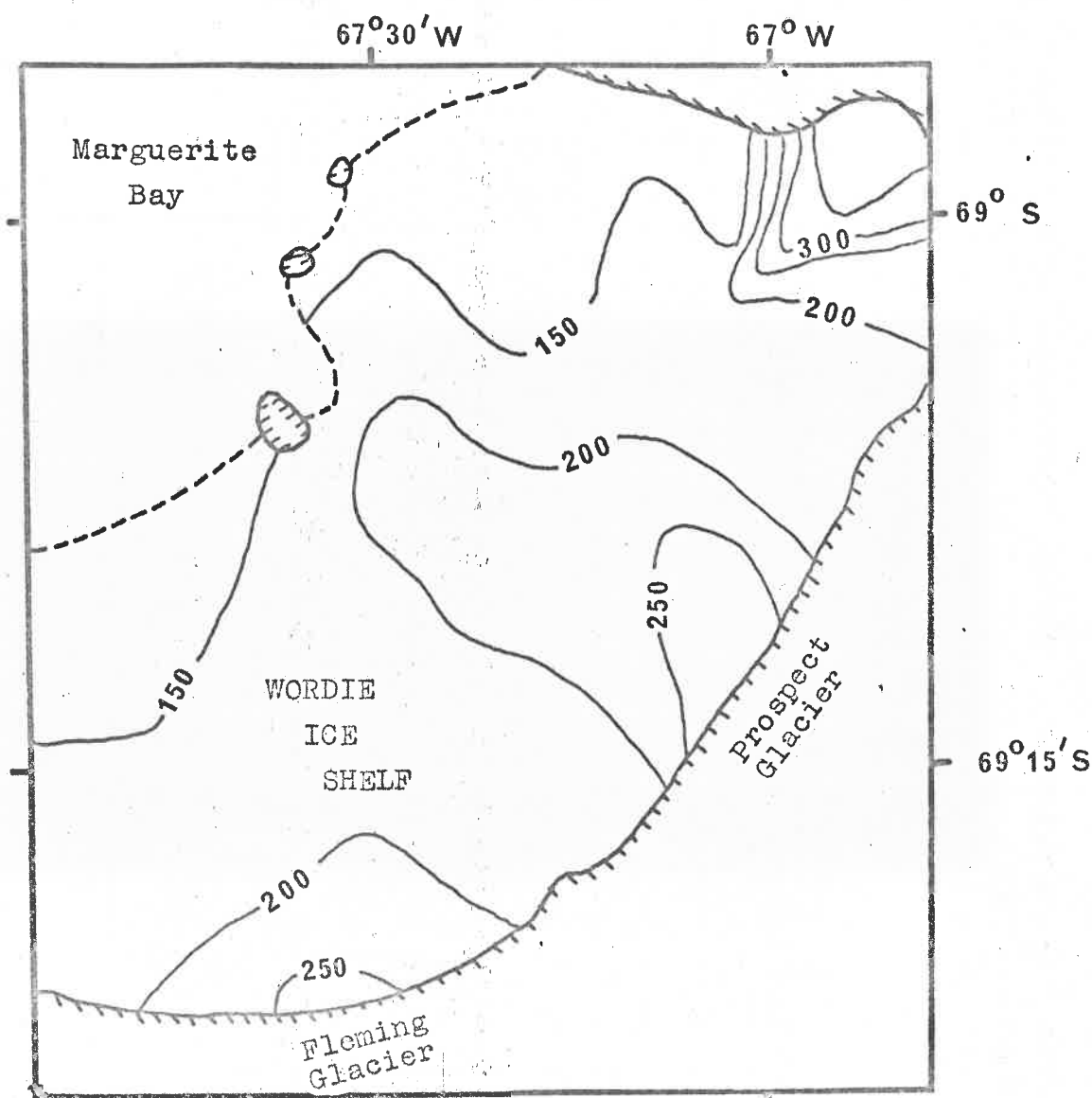


Figure 4.5.6

Contours of ice thickness on the Wordie Ice Shelf. The contour interval is 50 metres. The effects on ice thickness of the Fleming and Prospect Glaciers may be clearly seen. The thickening in the north-east corner is due to the Hariot Glacier.

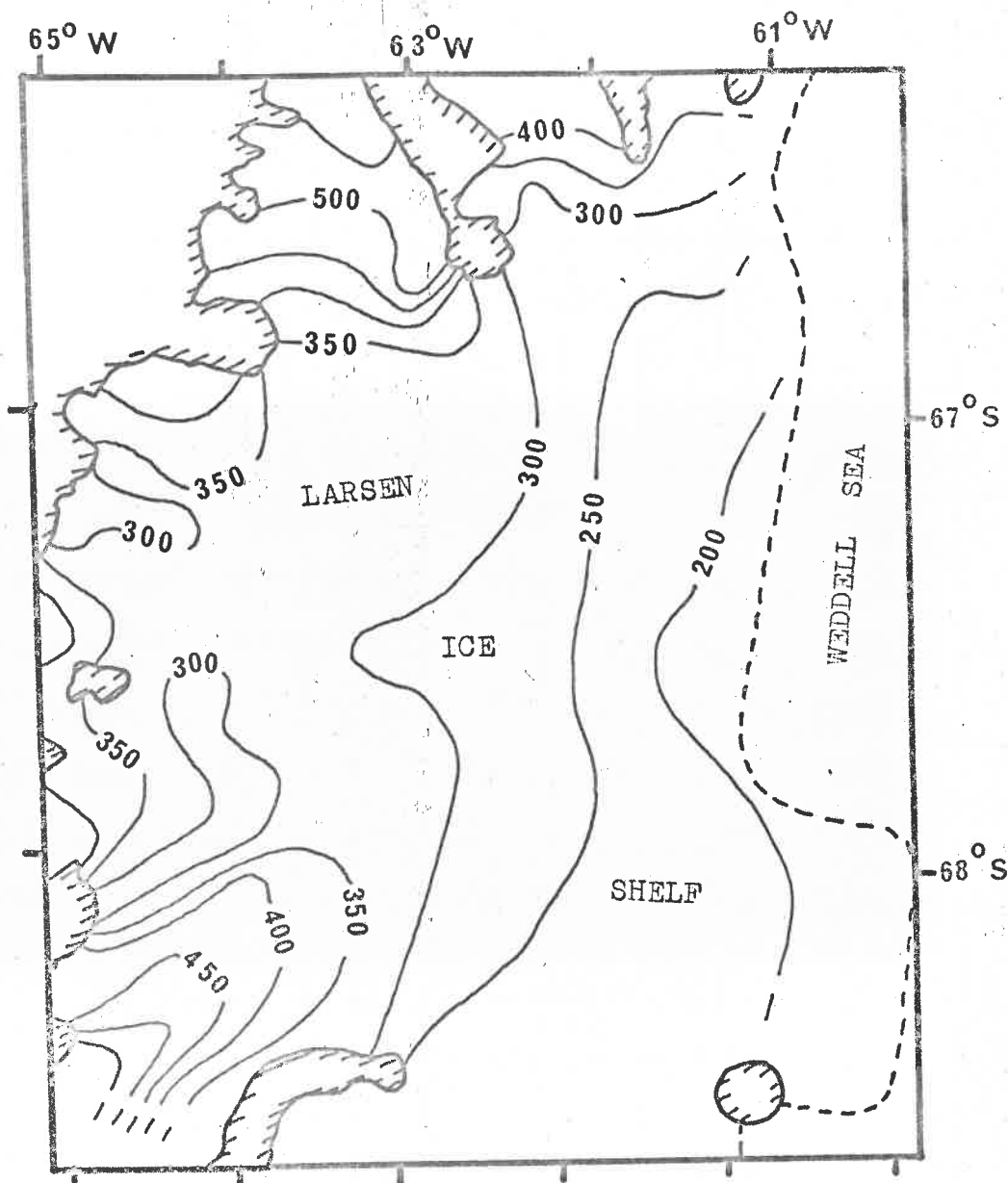


Figure 4.5.7

Contours of ice thickness on the Larsen Ice Shelf. The contour interval is 50 metres. Several glaciers have a pronounced effect on ice thickness, the most conspicuous being the ice from the Mercator Ice Piedmont in the south-west corner. It may be this ice stream which causes the bulge in the Larsen Ice Front in latitude 68°S being constrained in the south by the ice rise.

#### 4.6 Note regarding iceberg '1967-A'

Two giant icebergs in the Weddell Sea have been visible on ESSA satellite photographs since October 1967 when they were just off the coast in longitude 70°W. Swithinbank (1969) traced their progress to longitude 40°W and suggested their origin in the tongue of the Amery Ice Shelf that calved in December 1963 from a position in longitude 73°E and was sighted at intervals up to spring 1966, when it divided into two parts while in longitude 45°E. The mean velocity since its calving was about 13 mm s<sup>-1</sup>.

If the two icebergs seen on satellite photographs are the same as the two parts which separated in longitude 45°E, then the mean velocity between December 1965 and October 1967 would have to be 23 mm s<sup>-1</sup>. Between October 1967 and September 1968 the mean velocity as measured on satellite photographs was about 40 mm s<sup>-1</sup> so that it is quite possible that the icebergs averaged 23 mm s<sup>-1</sup> during the preceding two years. By January 1970 the larger of the two icebergs ('1967-A') was on the west side of the Weddell Sea in latitude 72°S longitude 59°W and was radio echo sounded during a flight from Fossil Bluff. Figure 4.6.1 shows the position of the iceberg and the track of the aircraft. Ice thicknesses were between 200 and 250 m which agree with estimates of the thickness of the Amery Ice Shelf (personal communication from W. Budd, 10 March 1970). More interesting is the attenuation of the bottom echo, which was between 6 and 10 dB per 100 m path in ice. This

is too high for pure ice even at  $0^{\circ}\text{C}$  but agrees with Budd's measurement of 7.5 dB per 100 m made on the Amery Ice Shelf. There is no evidence on the radio echo record of a brine layer close to sea level which could explain the high attenuation, but it might be explained by the origin of the Amery Ice Shelf itself. It is fed by the fast moving Lambert Glacier which is very disturbed where it enters the ice shelf. It is possible that brine is able to well up in rifts in such a way as to soak the bulk of the ice which then consolidates to form a smooth ice shelf while retaining its brine contamination. The rates of movement and snow accumulation over the Amery Ice Shelf as reported by Budd (1966) are such that ice which originated in the Lambert Glacier might be expected to represent a substantial proportion of the ice shelf thickness at the ice front. This could explain the high attenuation observed in the ice shelf, and the same attenuation found in the iceberg lends support to the theory of its origin.

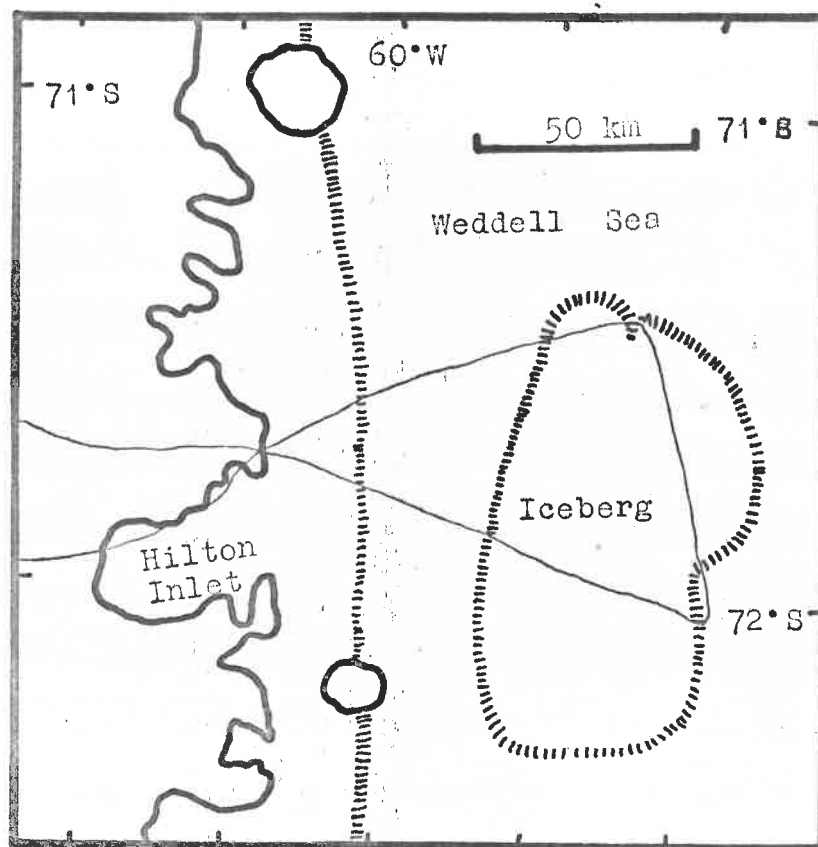


Figure 4.6.1

Showing the position of iceberg '1967-A' in the Weddell Sea when it was radio echo sounded, January 1970.

## CHAPTER 5

Navigational methods5.1 Available data

In this chapter we will consider the methods that have been used to determine the position of airborne radio echo sounding measurements. We will consider the installations in a Lockheed C121 Super Constellation aircraft operating from McMurdo Sound, Antarctica, during the 1967-68 season (chapter 4); in a twin-engined DeHavilland Otter operating in the Antarctic Peninsula during the 1969-70 season (chapter 4); and in a Lockheed C130 Hercules aircraft operating from McMurdo Sound, Antarctica, during the 1969-70 season (a sequel to the 1967-68 season).

For surveying purposes, positional information is usually obtained from a combination of a position-fixing system, by which positions are periodically determined without reference to the dynamic history of the aircraft, and a dead-reckoning system, by which such positions are extrapolated to future time. A consideration of most dead-reckoning and position-fixing systems has been published by Kayton and Freid (1969). In the Antarctic, the problems of maintenance, as well as economics, have limited the navigational systems to the most basic. It is likely that future survey work of this kind, will make use of more accurate techniques. Nevertheless, the general results obtained in this chapter will be applicable to position-fixing and dead-reckoning systems which are more precise.

All three aircraft were equipped with an SFIM flight recorder that was used to record, in an analogue form, all flight parameters of navigational importance. The medium of recording is photographic paper, 60 mm wide. It has the advantage of relative simplicity, but requires photographic processing. The parameters which have been monitored are as follows:

The static air pressure was measured by means of an aneroid transducer in the flight recorder, to an accuracy of about 0.1 mbar.

The pitot air pressure (stagnation pressure) was measured to the same accuracy by a similar transducer.

The outside air temperature was recorded using a resistive thermometer in a bridge circuit. This could be read to about 1°C, but its calibration depends upon aircraft velocity.

Heading information was recorded by converting a suitable synchro signal to a DC signal using a proprietary converter (SE Laboratories Ltd.). The Twin Otter aircraft operating at some distance from the magnetic pole, used a gyro-stabilized magnetic compass, while the two larger aircraft used free gyros to provide heading information.

The terrain clearance of the larger aircraft was measured by a microwave radar altimeter. On the Twin Otter, the only record of terrain clearance was contained on the radio echo film.

The C130 Hercules was equipped with a doppler system, and the velocity components along-track and across-track were recorded on



the SFIM flight recorder.

The principal disadvantage of an analogue recording medium is that it has to be digitized before the information can be used in a computer. Figure 5.1.1 shows a section of the flight recorder trace. The two air pressure signals are represented as two traces each, one coarse trace, and one vernier trace. Methods of automatic digitizing were considered but none were implemented. Perhaps the most promising solution would be to use a television camera linked to a digital computer, in such a way that the coordinates of the lines could be found rapidly. The author is of the opinion that it would be possible for such a computer to distinguish the many traces by means of their statistical properties. It has not been possible to explore this further. Instead a proprietary semi-automatic trace reader (PCD Ltd.) has been used to digitize all the SFIM traces. This instrument requires a cursor to be manually positioned over the required point, so that the coordinates of the cursor may be reproduced on punched paper tape. This is used in subsequent computer analysis. Tests made with this instrument indicate that the standard deviation in each coordinate is about 0.3 mm. This figure is partly due to the instrument resolution, and partly due to operator inaccuracy. Two methods of reading the information on the SFIM have been used. The 1967-68 records were read in the simplest way: the Y co-

ordinates of all traces being measured at each time interval. The intervals were chosen to represent adequately any change in a parameter. The minimum interval used was 5 seconds, the maximum interval was 60 seconds. A total of 95 hours flight data were digitized in this way. The 1969-70 records were digitized in a more rapid manner, requiring a more sophisticated computer program. In successive 'epochs' (usually 15 minutes) of record, each trace was digitized as a series of points which were linked by the computer program with straight lines. The value of each parameter was then computed at 6 second intervals. By this means, only a few points were necessary to define an approximately straight trace, while rapidly changing traces were digitized at closer intervals. With the earlier method, all traces were read frequently, if only one was fluctuating. By either method, the information contained on the SFIM record was converted into a computer compatible punched paper tape.

In addition to the flight recorder, the two larger aircraft were equipped with trimetrogon cameras. These are large mapping cameras producing nine inch square negatives. Three such cameras are used together; one vertical, one left oblique, and one right oblique. The fields of view overlap so that complete coverage is obtained as the aircraft proceeds. The Twin Otter aircraft carried a hand-held 35 mm camera which was also used for terrain photography. The photographs produced by these cameras were

used in the computation of position.

The two larger aircraft were equipped with sextants to permit celestial observations to be made. These were used in navigation, and they were also used to obtain azimuth information to correct the free-gyro compasses which were otherwise liable to drift.

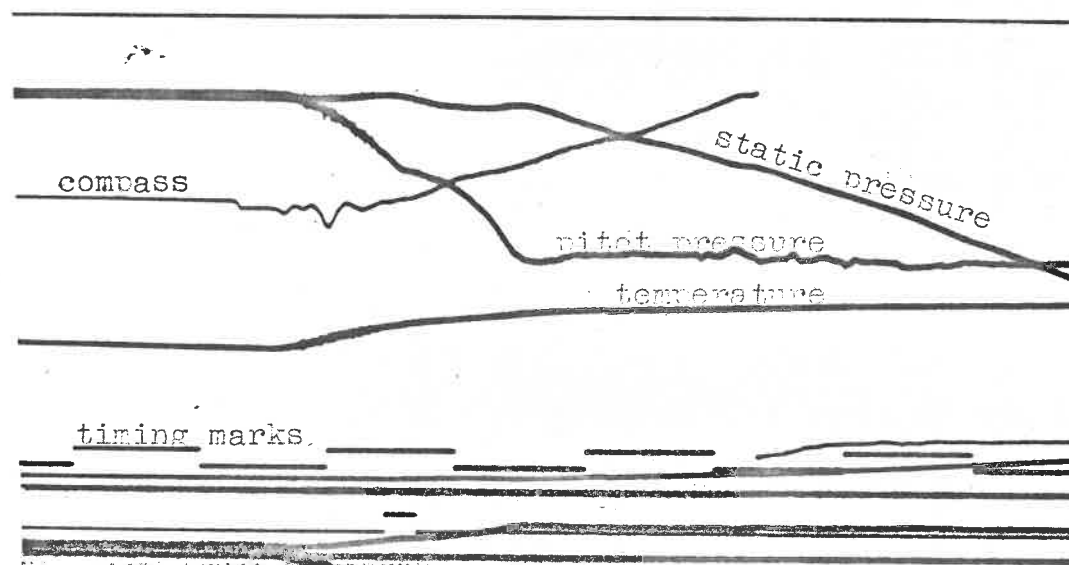


Figure 5.1.1

Showing part of the S.F.I.M. flight recorder chart.

## 5.2 Dead reckoning methods

The principal dead-reckoning system relied on air data for speed information. The pitot and static air pressures and the air temperature were obtained from the SFIM flight recorder data. The measured air temperature ( $T_m$ ) is a function of aircraft speed. Thermodynamic considerations yield the relationship:

$$T_m = T_s \left[ 1 + \frac{\gamma-1}{2} \eta Ma^2 \right] \quad (1)$$

(Kayton and Freid 1969 p.448)

where  $\gamma$  is the specific heat ratio,  $Ma$  is the Mach number, and  $\eta$  is the recovery factor of the probe. For our purposes, the temperature transducers have been calibrated at the normal cruising speed of the aircraft using tables which take account of the effect of aircraft structures etc. The true air speed ( $V$ ) is obtained from the pitot ( $P_t$ ) and static ( $P_s$ ) pressures and temperature ( $T$ ) using the relationship:

$$\frac{P_t}{P_s} = \left( 1 + \frac{\gamma-1}{2} \frac{V^2}{2RT} \right)^{\frac{\gamma}{\gamma-1}} \quad (2)$$

where  $R$  is the gas constant for air (Kayton and Freid 1969 p.447)

The true air speed together with the heading information provides a velocity vector which is the basis of the dead-reckoning integration. The doppler system in the Hercules aircraft was only intermittently available, but when operating, it was used in preference to air data, to provide a velocity vector for dead-reckoning.

The way in which the velocity vector was integrated has varied. Both the Super Constellation and the Hercules used free gyros for heading information, and these were aligned with the South Polar Grid. This is a rectangular grid which is parallel to the Greenwich meridian on a Polar Equidistant projection. The size of one grid degree is the same as the size of one degree of latitude at the point where the grid intersects the quadrant meridians. Grid heading and true heading differ by the value of the local longitude.

The dead-reckoning integration of the 1967-68 data was performed in the grid plane. The velocity vectors in grid units were summed, assuming movement in a rectangular plane. This is obviously an incorrect assumption but required minimum programming effort since the heading information was in the grid system. In fact, within  $20^\circ$  latitude of the Pole, grid lines differ only slightly from great circles. For example, consider the line joining McMurdo Station ( $77^\circ 51'S$   $166^\circ 37'E$ ) and Byrd Station ( $80^\circ 1'S$ ,  $119^\circ 32'W$ ). Solving the spherical triangle we find that the Grid azimuth of the great circle from McMurdo to Byrd is  $59^\circ 30' 6''W$  and the length of the arc is  $13^\circ 21' 28''$ . In the Grid plane, the azimuth is  $59^\circ 2' 12'' W$  and the length of the arc is  $13^\circ 24' 34''$ . The difference in azimuth is less than 30 seconds of arc, and the difference in distance is less than 0.5%.

With improved programming expertise, integration of velocity vectors on the spheroid was no longer a problem, and the 1969-70

data of both the Twin Otter and the Hercules aircraft were analysed in this way. The Twin Otter used a gyro stabilized magnetic compass so that knowledge of the magnetic variation was required. Examination of the few measurements of magnetic variation which were available showed that in the area of the Antarctic Peninsula, the following first-order two-dimensional polynomial could be used to relate magnetic variation to position:

$$\text{Variation (east)} = 0.57 (\text{Latitude}) + 0.71 (\text{Longitude}) - 65.6$$

(3)

All units are degrees. The form of the equation indicates that lines of constant variation are parallel straight lines on a Plate Carée projection (similar to Mercator near to the equator). The true heading of the Hercules was obtained from its grid heading by adding westerly longitude. Both are therefore position dependant. This means that an error in the dead-reckoning system, causing an incorrect DR position to be arrived at, has a second order error in that the directional information used for subsequent integration is slightly in error. In the case of the Hercules, this is not a problem since an error in position, even close to the pole where longitude changes rapidly, is still integrated to produce the same shape of track in the grid plane, and we have seen that the error in this is not large. The area covered by flights of the Twin Otter is small enough for the problem to be neglected. If the

problem were serious, an iterative solution would be to use the corrected track (see section 5.4) to derive an improved version of the magnetic variation which would then be used to re-compute the dead-reckoning track. The process could be repeated as many times as are necessary.



### 5.3 Position fixing methods

Three large stations, McMurdo, Byrd, and Amundsen-Scott Base at the south pole, were equipped with TACAN beacons. Both the Super Constellation and the Hercules aircraft were able to use the beacons. Unfortunately the range of these facilities is only about 100 km at low altitudes. At higher altitudes the range is greater but the error in position due to the limited accuracy of the azimuth measurement may be as much as 20 km at a range of 200 km. Flights from these stations frequently ranged out to 1500 km and for this reason, TACAN was only useful as a terminal navigation aid. Apart from TACAN no radio navigational aid was available. Often the only method of position fixing was visual identification or (what amounts to the same thing) identification on the aircraft radar or later identification on the trimetrogon photographs. The methods required the region to be mapped in advance and in many areas of the Antarctic, conspicuous surface features are absent. The aircraft radar (not available on the Twin Otter) extended the useful range of visual identification but with a correspondingly greater error. Within visual range of mapped surface features, the trimetrogon cameras were regularly used to permit later resection of position.

One method of photographic resection which we have used, entailed using the semi-automatic coordinate reader to measure the positions on oblique aerial photographs, of known control points.

The angles subtended by such control points could then be computed. Figure 5.3.1 shows the geometry of two points, A and B, and the lens L, and principal point P. The angle between feature A and the centre line of the photograph at A' is given by:

$$\phi_1 = \arctan \left( \frac{AA'}{\sqrt{LP^2 + PA'^2}} \right) \quad (4)$$

Similarly for feature B:

$$\phi_2 = \arctan \left( \frac{BB'}{\sqrt{LP^2 + PB'^2}} \right) \quad (5)$$

We have made the simplifying assumption that the angle in the horizontal plane, subtended by the two features at the lens is:

$\phi_1 + \phi_2$ . This angle is incorrect by a factor equal to the cosine of the angle by which the observed features depart from the horizontal plane through the aircraft. Even at 100 km range the contribution from the earth's curvature is only about  $1^\circ$  and therefore the largest error in this assumption is usually due to the different altitudes of the aircraft and the control points. A difference from the horizontal of  $5^\circ$  would introduce an error of 0.5% in the calculated angle.

Subtended angles have also been measured with a perspective

overlay. On a horizontal surface one may construct radials from the nadir, and project these into the focal plane of the photograph. Vertical planes passing through the observer's vertical intersect the plane of the photograph in straight lines, therefore the projection of horizontal angles is unaffected either by earth curvature or by the height of the observer above the control points.\* However the projection of radials is affected by the inclination of the optic axis of the camera: a change of  $5^\circ$  from the nominal inclination of  $30^\circ$  for trimetrogon obliques, introduces an error of 5% in the measured angle subtended by control points near the horizontal. In the case of camera swing, both the graphical and geometrical methods need to use the apparent horizon to define the vertical through the optic axis (unless there is separate information about the aircraft pitch).

Given the geographic positions of the chosen control points, it is possible to compute the theoretical angles in the horizontal plane, subtended at any assumed position. An iterative computer program has been written which adjusts the assumed position to one having a least-squared difference between observed and computed

\* Footnote

This is not true of the 'Canadian Grid' overlay which is used to measure distances between features in the photograph - clearly scale depends directly on the height of the observer.

overlay. On a horizontal surface one may construct radials from the nadir, and project these into the focal plane of the photograph. Vertical planes passing through the observer's vertical intersect the plane of the photograph in straight lines, therefore the projection of horizontal angles is unaffected either by earth curvature or by the height of the observer above the control points.\* However the projection of radials is affected by the inclination of the optic axis of the camera: a change of  $5^\circ$  from the nominal inclination of  $30^\circ$  for trimetrogon obliques, introduces an error of 5% in the measured angle subtended by control points near the horizontal. In the case of camera swing, both the graphical and geometrical methods need to use the apparent horizon to define the vertical through the optic axis (unless there is separate information about the aircraft pitch).

Given the geographic positions of the chosen control points, it is possible to compute the theoretical angles in the horizontal plane, subtended at any assumed position. An iterative computer program has been written which adjusts the assumed position to one having a least-squared difference between observed and computed

\* Footnote

This is not true of the 'Canadian Grid' overlay which is used to measure distances between features in the photograph - clearly scale depends directly on the height of the observer.

angles for a number of control points. Three control points are required for a unique position; using more than three points, the probable error in the position obtained is reduced. The restriction that applies to a conventional resection, namely that the control points must not lie on a circle through the position occupied, applies to this method. Position fixes have been obtained by this method at distances as great as 100 km from mapped surface features which were visible on oblique aerial photographs. The uncertainty in the positions obtained by this method has been found to be a few percent of the distance of the control points. Figure 5.3.2 shows a track plot using numerous fixes obtained from oblique aerial photographs. Some fixes have been rejected because the magnitude of the minimum residual obtained, suggested an error in control point identification.

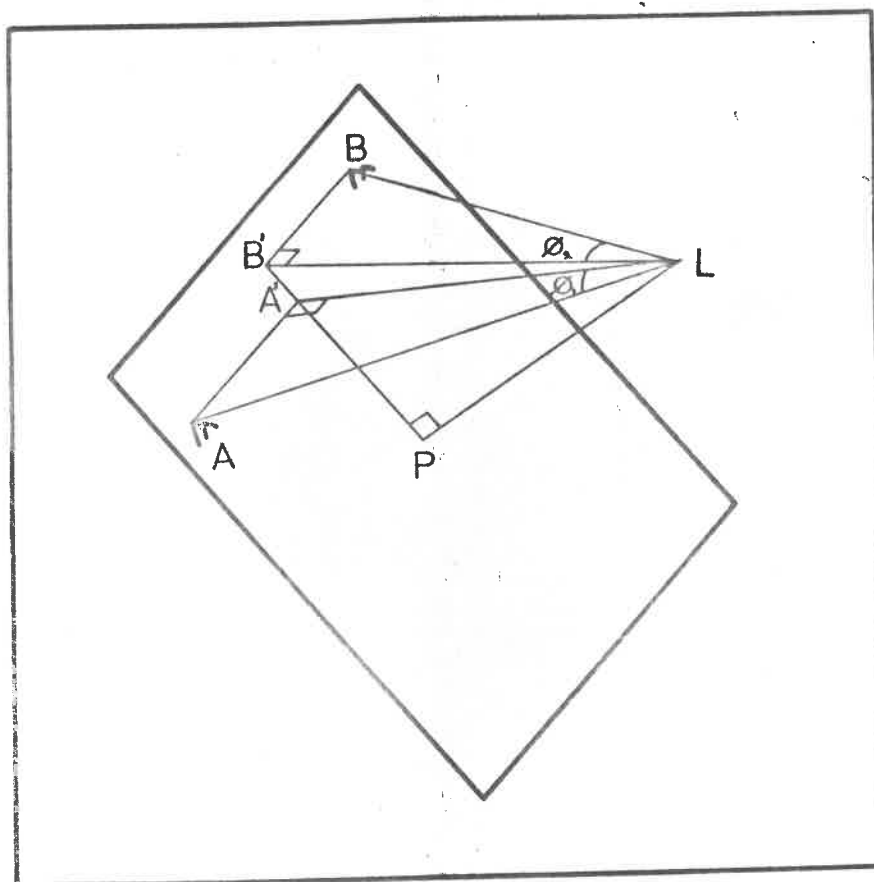
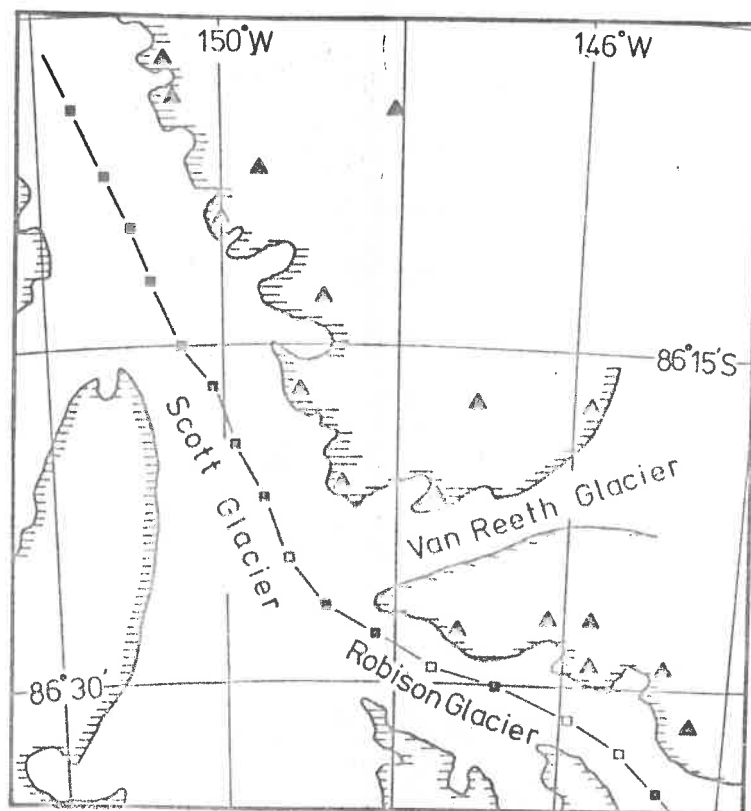


Figure 5.3.1

Showing the geometry of an oblique aerial photograph.







- |   |  |
|---|--|
|  rock          |  photo fix          |
|  control point |  rejected photo fix |

Figure 5.3.2

Showing part of a flight track which has been computed using position fixes obtained from oblique aerial photographs.

#### 5.4 Navigational accuracy in general terms

In general there is a probable error in both the position-fixing system and the dead-reckoning system. The nature and magnitude of these errors have been discussed by Kayton and Freid (1969). Ramsayer (1969) has proposed a method by which the important systematic errors in the dead-reckoning system are determined by least squares adjustment, and corrected for during flight; the process requires the use of an airborne computer. In the case of geophysical surveying, the track may be determined more accurately in retrospect knowing the point of arrival as well as the point of departure.

Consider a position fix  $(X_{fix}, Y_{fix})$ , and a dead-reckoning position at the fix  $(X_{dr}, Y_{dr})$ , having variances of  $\sigma_{fix}^2$  and  $\sigma_{dr}^2$  respectively. A weighted mean position may be expressed thus:

$$\hat{X} = w_{dr} X_{dr} + w_{fix} X_{fix} \quad (6)$$

$$\hat{Y} = w_{dr} Y_{dr} + w_{fix} Y_{fix} \quad (7)$$

where the weights are related thus:

$$w_{dr} + w_{fix} = 1$$



This weighted-mean position has a variance in  $X$  of:

$$\sigma^2(\hat{x}) = w_{fix}^2 \sigma_{fix}^2 + w_{dr}^2 \sigma_{dr}^2 \quad (8)$$

The variance is minimized by setting  $\frac{\partial \sigma^2(\hat{x})}{\partial w_{fix}}$  and  $\frac{\partial \sigma^2(\hat{x})}{\partial w_{dr}}$  to zero. In this way the weights for an optimum weighted-mean position are found:

$$w_{dr} = \frac{\sigma_{fix}^2}{\sigma_{fix}^2 + \sigma_{dr}^2} ; w_{fix} = \frac{\sigma_{dr}^2}{\sigma_{fix}^2 + \sigma_{dr}^2} \quad (9)$$

In the case of a position line, we may consider it to be a position fix but with a variance of  $\infty$  in the direction parallel to the position line, and a variance of  $\sigma_{pl}^2$  perpendicular to the position line. If the dead-reckoning position is  $(X_{dr}, Y_{dr})$  with variance  $\sigma_{dr}^2$  and the position line is given by  $Y = mX + c$ , then the foot of the perpendicular from the dead-reckoning position on to the position line is the point  $(X_{fix}, Y_{fix})$  where:

$$X_{fix} = \frac{X_{dr} + mY_{dr} - mc}{m^2 + 1} \quad (10)$$

$$Y_{fix} = mX_{fix} + c \quad (11)$$

The position having minimum variance is given by:

$$\hat{X} = \frac{\sigma_{pl}^2}{\sigma_{pl}^2 + \sigma_{dr}^2} X_{dr} + \frac{\sigma_{dr}^2}{\sigma_{pl}^2 + \sigma_{dr}^2} X_{fix} \quad (12)$$

$$\hat{Y} = \frac{\sigma_{pl}^2}{\sigma_{pl}^2 + \sigma_{dr}^2} Y_{dr} + \frac{\sigma_{dr}^2}{\sigma_{pl}^2 + \sigma_{dr}^2} Y_{fix} \quad (13)$$

The variance of this point is  $\sigma_{dr}^2$  in the direction parallel to the position line, and  $\frac{\sigma_{pl}^2 \sigma_{dr}^2}{\sigma_{pl}^2 + \sigma_{dr}^2}$  perpendicular to the position line.

Having thus obtained the optimum position at a fix, we extrapolate the position to future time by means of a dead-reckoning system. In general the variance of the dead-reckoning system degrades with time. However, unlike the in-flight case dealt with by Ramsayer, the point of arrival at a new fix may be used to improve a post flight track. At each new fix a similar optimum position may be found by application of the above expressions. In practice the accuracy of a fix has been much greater than the accuracy of the dead-reckoning position and the computer program has therefore been written to use the fix position and ignore the dead-reckoning position. The dead-reckoning track is then adjusted linearly with time (see next section) to fit the fixes. This produces a corrected track plot which passes through the fixes, but

The position having minimum variance is given by:

$$\hat{X} = \frac{\sigma_{pl}^2}{\sigma_{pl}^2 + \sigma_{dr}^2} X_{dr} + \frac{\sigma_{dr}^2}{\sigma_{pl}^2 + \sigma_{dr}^2} X_{fix} \quad (12)$$

$$\hat{Y} = \frac{\sigma_{pl}^2}{\sigma_{pl}^2 + \sigma_{dr}^2} Y_{dr} + \frac{\sigma_{dr}^2}{\sigma_{pl}^2 + \sigma_{dr}^2} Y_{fix} \quad (13)$$

The variance of this point is  $\sigma_{dr}^2$  in the direction parallel to the position line, and  $\frac{\sigma_{pl}^2 \sigma_{dr}^2}{\sigma_{pl}^2 + \sigma_{dr}^2}$  perpendicular to the position line.

Having thus obtained the optimum position at a fix, we extrapolate the position to future time by means of a dead-reckoning system. In general the variance of the dead-reckoning system degrades with time. However, unlike the in-flight case dealt with by Ramsayer, the point of arrival at a new fix may be used to improve a post flight track. At each new fix a similar optimum position may be found by application of the above expressions. In practice the accuracy of a fix has been much greater than the accuracy of the dead-reckoning position and the computer program has therefore been written to use the fix position and ignore the dead-reckoning position. The dead-reckoning track is then adjusted linearly with time (see next section) to fit the fixes. This produces a corrected track plot which passes through the fixes, but

is controlled between them by the dead-reckoning information. Figure 5.4.1 shows graphically the relation between fixes, dead-reckoning, and ice thickness measurement in the production of the (X, Y, Z) data. The methods of presenting these data are described in the next chapter. Deconvolution refers to the process of reconstructing the true bedrock profile from the distorted profile which is obtained using a wide beam aerial (see chapter 1). We have assumed that this process is not required, and that the parameter of interest is the range of the nearest reflecting surface, rather than the vertical ice thickness at any point. The difference between the dead-reckoning position and the fix position has been found to be typically 10 metres per second of dead-reckoning time using air data, and 2 metres per second of dead-reckoning time using the doppler information.

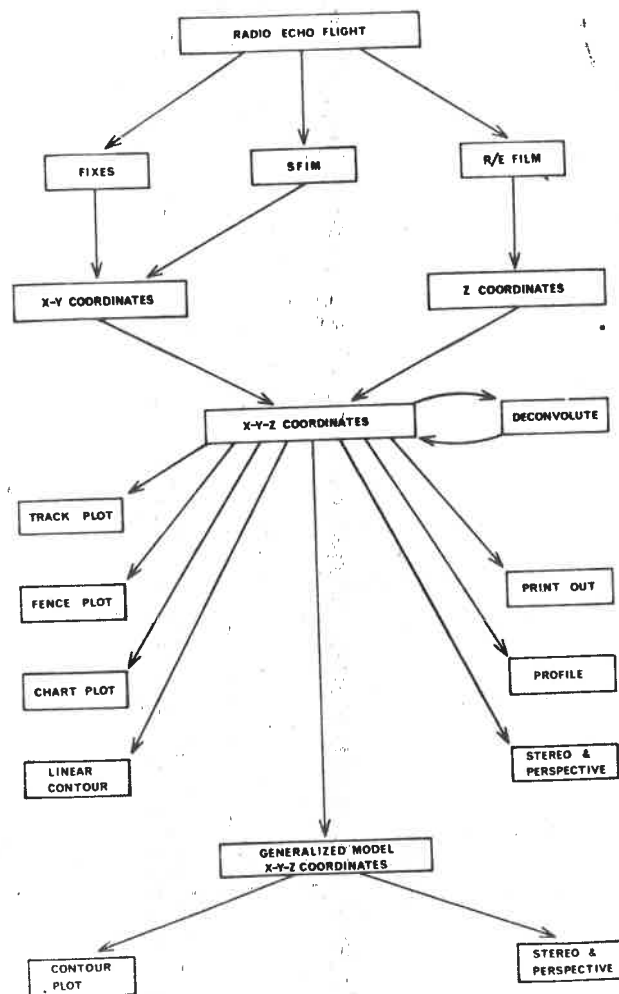


Figure 5.4.1

Showing the relation between the positional information and the ice thickness measurement, in producing the (X,Y,Z) coordinates which specify each measurement.

### 5.5 Random errors in dead-reckoning

We will now consider random errors in the dead-reckoning system and neglect for the moment errors in the fixes. Suppose that the departure of the dead-reckoning track from the actual track is formally the same as a Brownian motion in both directions  $X$  and  $Y$ . This will be the case if the dead-reckoning system integrates velocity signals having gaussian noise but no systematic error in them. If the root mean square velocity of departure in one dimension is  $V_{rms}$ , the probability distribution of departure  $x$  after a time  $t$  is normal with variance  $V_{rms}^2 t$ .

$$P(x, t) = \frac{1}{V_{rms} \sqrt{2\pi t}} \exp \left[ \frac{-x^2}{2 V_{rms}^2 t} \right] \quad (14)$$

If at some time  $t$  the departure is known to be  $x$ , then at some later time  $T$  the departure  $X$  will be distributed according to:

$$P(X, T/x, t) = \frac{1}{V_{rms} \sqrt{2\pi(T-t)}} \exp \left[ \frac{-(X-x)^2}{2 V_{rms}^2 (T-t)} \right] \quad (15)$$

It may be shown that the probability distribution of departure  $x$  after time  $t$ , given the departure  $X$  after time  $T$ , is:

$$p(x, t/X, T) = p(X, T/x, t) \frac{p(x, t)}{p(X, T)} \quad (16)$$

Hence knowing the departure  $X$  after time  $T$  by means of a position fixing system, the departure  $x$  after some lesser time  $t$  is distributed thus:

$$p(x, t/X, T) = \frac{1}{V_{rms} \sqrt{2\pi t(1-\frac{t}{T})}} \exp \left[ \frac{-(x - \frac{t}{T}X)^2}{2V_{rms}^2 t(1-\frac{t}{T})} \right] \quad (17)$$

This is a normal distribution centred on  $(t/T) X$  with standard deviation  $V_{rms} \sqrt{t(1-t/T)}$ . Hence we have obtained the well known result that the probable error in the track can be minimized by making  $(x - (t/T)X)$  the corrected track. The root mean square value of  $X$  is  $V_{rms} \sqrt{T}$  and the ratio of  $x_{rms}$  to  $X_{rms}$  is:

$$\sqrt{\frac{t(1-\frac{t}{T})}{T}} \quad (18)$$

This has a maximum value (when  $t = T/2$ ) of 0.5. Thus the adjusted track may be in error by half the root mean square observed departure at a new fix.

### 5.6 Systematic errors in dead-reckoning

We will now consider the effect of certain systematic errors in the dead-reckoning system, and again neglect errors in the fixes. Define the following vector positions:

- $A(t)$       The actual track between ideal fixes
- $B(t)$       The track obtained by dead reckoning
- $C(t)$       The corrected track

and the following vector velocities:

- $V(t)$       The true velocity vector
- $W(t)$       The velocity vector used by the dead-reckoning system

For simplicity in assessing these errors assume that navigation is in a plane. If at time  $t = 0$  the vector position is known to be  $P$ , then we can write the expressions:

$$A(t) = P + \int_0^t V(\tau) d\tau \quad (19)$$

and

$$B(t) = P + \int_0^t W(\tau) d\tau \quad (20)$$

Then the departure of the dead-reckoning track from the true track is:

$$B(t) - A(t) = \int_0^t W(\tau) - V(\tau) d\tau \quad (21)$$



If at time  $T$  the true vector position is known (an ideal fix) then the value of  $B(T) - A(T)$  is observed and the corrected track is obtained by adjusting the dead-reckoning track in accordance with the rule derived for a random departure, i.e. linearly with time.

$$C(t) = B(t) - (t/T) \{ B(T) - A(T) \}$$

which is:

$$C(t) = P + \int_0^t W(\tau) d\tau - (t/T) \int_0^T [W(\tau) - V(\tau)] d\tau \quad (22)$$

From this we obtain the difference between the true track and the corrected track:

$$C(t) - A(t) = \int_0^t [W(\tau) - V(\tau)] d\tau - (t/T) \int_0^T [W(\tau) - V(\tau)] d\tau \quad (23)$$

It may be seen that this is identically zero at times  $t = 0$  and  $t = T$ , that is the corrected track is constrained to pass through the initial and final fixes regardless of any error in the dead-reckoning system. At other times, the difference between the corrected track and the true track depends upon  $W(t) - V(t)$  that is errors in the dead-reckoning system.

The propagation of errors in doppler and inertial navigators

used as 'open loop' dead-reckoning systems is a much-studied subject. We will substitute some (likely) systematic errors in these systems into equation (23) above, and evaluate their effect on the corrected track.

1) A systematic error in the scale factor of velocity might be the result of miscalibration of the dead-reckoning system or for example mis-alignment of a doppler beam. We may then write:

$$W(t) = (1 + \delta) V(t) \quad (24)$$

Equation (23) above reduces to:

$$C(t) - A(t) = \int_0^t \delta V(\tau) d\tau - (t/T) \int_0^T \delta V(\tau) d\tau \quad (25)$$

This is only zero (the corrected track identical to the true track)

if  $\int_0^t V(\tau) d\tau \propto t$  which is true if  $V(t)$  is a constant.

Otherwise the error in the corrected track at any instant is equal to  $\delta$  multiplied by the distance between the actual position and the position interpolated along a straight line between the fixes.

Clearly the more nearly straight the actual track, the more accurate the corrected track.

2) A systematic velocity offset might be due to miscalibration of the dead-reckoning system or to some bias in a doppler navigator frequency tracker. Note that a constant wind vector is formally the same as this in the case of a dead-reckoning system which relies upon air data. We may then write:

$$W(t) = K(t) + V(t) \quad (26)$$

Equation (23) then becomes:

$$C(t) - A(t) = \int_0^t K(\tau) d\tau - (t/T) \int_0^T K(\tau) d\tau \quad (27)$$

which for a constant  $K(t)$  is identically zero. Thus a constant error in velocity does not cause an error in the corrected track. If the velocity offset is due to some bias in the frequency tracker of a doppler navigator, the  $K(t)$  is only constant if  $V(t)$  is also constant. If  $V(t)$  is not constant then  $K(t)$  will vary and the corrected track will be in error. In the case of an air data dead-reckoning system, the wind vector  $K(t)$  is most likely not to be constant and again the corrected track is in error.

3) A constant error in the heading information may be caused by incorrect alignment of the compass gyro or, in the case of a magnetic compass, by incorrect magnetic variation information.

In this case if we write:

$$W(t) = V' \exp(j \Theta) \quad (28)$$

$$V(t) = V' \exp(j \phi) \quad (29)$$

where  $V'$  is a scalar speed, and the heading error  $\delta$  is equal to:

$$\delta = \Theta - \phi$$

Equation (23) reduces to:

$$C(t) - A(t) = \{\exp(j\delta) - 1\} \left\{ \int_0^t V(\tau) d\tau - (t/T) \int_0^T V(\tau) d\tau \right\} \quad (30)$$

Once again we see that if  $V(t)$  is constant this is identically zero and the corrected track is the true track.

4) A constant rate of change of heading error is not infrequently a property of an imperfect gyro. In this case we write:

$$W(t) = V' \exp [j(\phi + \delta t)] \quad (31)$$

$$V(t) = V' \exp [j\phi] \quad (32)$$

If  $V(t)$  is a constant, then expression (23) becomes:

$$\frac{V e^{j\phi}}{j\delta} \left\{ (e^{j\delta t} - 1) - \frac{t}{T} (e^{j\delta T} - 1) \right\} \quad (33)$$

If  $\delta T$  is small this reduces to:

$$V e^{j\phi} \frac{j\delta}{2} t (T-t) \quad (34)$$

The magnitude of the difference is an extremum when:  $t = T/2$ , the same as for the other systematic errors, and it is equal to:

$$\frac{V \delta T^2}{8} \quad (35)$$

For example: Consider a gyro drift of 0.01 radians per hour.

If the time between fixes is 1 hour and the distance covered in an hour is 500 km, the maximum error in the corrected track would

be: 0.6 km.

It is clear from the above illustrations that the corrected track most closely approximates to the true track if the velocity vector is constant; that is the aircraft flies at a constant speed in a constant direction between fixes.

To illustrate the accuracy of a corrected track, figure 5.6.1 shows the process of fitting the dead-reckoning track to the fixes applied to a flight in the Antarctic Peninsula. The portion of the flight shown covers about 400 km and has been fitted to four fixes. Four other fixes which were not used to correct the track are shown, together with the corresponding dead-reckoning position. Air data was used to compute the dead-reckoning track and it may be seen that the track has a number of direction changes. On a portion between fixes of about 200 km the average error at the unused fixes is about 4 km or 2% of the interfix distance.

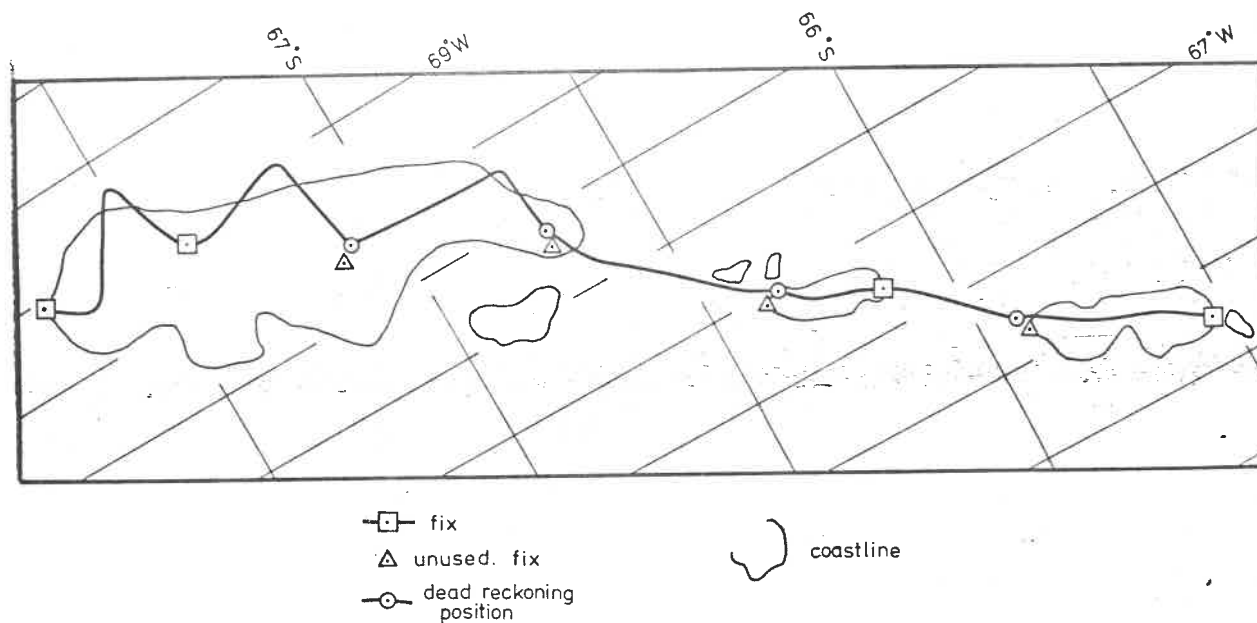


Figure 5.6.1

Showing part of a flight track over the west coast of the Antarctic Peninsula. Some fixes which were not used in the computation, are shown relative to the positions obtained for the corrected track.

### 5.7 Information gained

In general, neither the measured property  $Z(X,Y)$  nor the position  $(X,Y)$  is known exactly. We suppose throughout this section that it is the relation of  $Z$  to  $(X,Y)$  which is desired. As suggested earlier there are some investigations where the relationship of two properties  $Z_1$  and  $Z_2$  is sufficient in itself without precise knowledge of  $(X,Y)$ . The information,  $J$ , gained in a particular measurement  $(Z,X,Y)$  is defined as the binary logarithm of the ratio of the probability that the property has a measured value after measurement, to the probability before measurement.

$$J = \log_2 \left\{ \frac{\text{Probability after}}{\text{Probability before}} \right\} \quad \text{bits} \quad (36)$$

The probability distribution of the property 'before' measurement may be estimated from measurements of  $Z$  along the track without reference to the absolute  $(X,Y)$  position, provided that relative positions are known accurately and the statistical properties of  $Z$  are isotropic. Alternatively some a priori assumption may be made about the statistical properties of  $Z$ . The probability of the property having the measured value, call it  $Z_m$ , before measurement is therefore estimated. After measurement the property is distributed about the measured value, and the width of the distribution is related to the resolution of the measuring



instrument, and the accuracy of positional information. Suppose that the  $Z$ , insofar as it is known before measurement, is normally distributed about a mean value  $\langle Z \rangle$  with standard deviation  $\sigma_1$ . After measurement  $Z$  has a probability distribution which is normal about the observed value  $Z_m$  with standard deviation  $\sigma_2$  as illustrated in figure 5.7.1.

Before measurement the probability distribution of  $Z$  is:

$$p(z) dz = \frac{1}{\sigma_1 \sqrt{2\pi}} \exp \left[ \frac{-(z - \langle z \rangle)^2}{2 \sigma_1^2} \right] \quad (37)$$

After measurement the probability distribution of  $Z$  is:

$$p(z) dz = \frac{1}{\sigma_2 \sqrt{2\pi}} \exp \left[ \frac{-(z - z_m)^2}{2 \sigma_2^2} \right] \quad (38)$$

Then before measurement

$$P(Z=Z_m) dz = \frac{1}{\sigma_1 \sqrt{2\pi}} e^{-\frac{(z_m - \langle z \rangle)^2}{2 \sigma_1^2}} \quad (39)$$

and after measurement

$$P(Z=Z_m) dz = \frac{1}{\sigma_2 \sqrt{2\pi}} \quad (40)$$

The new information contained in the statement 'Z has the value  $Z_m$  at the point (X,Y)' is given by:

$$J = \log_2 \left\{ \frac{\sigma_1}{\sigma_2} \exp \left[ -\frac{(\bar{Z}_m - \langle Z \rangle)^2}{2 \sigma_1^2} \right] \right\} \quad (41)$$

This applies only to a single such statement. If a number of statements are made for points which are close together then the probability distribution 'before' a given statement is made will be modified by the data already given, that is to say,  $\sigma_1$ , is reduced, and the information gained is reduced.

Let us make the additional assumption that the function Z has a normalized auto-correlation function which is gaussian:

$$c(\tau) = e^{-\frac{\tau^2}{T^2}} \quad (42)$$

where  $\tau$  is the separation in the XY plane, and  $T$  is the auto-correlation distance. Figure 5.7.2 shows in one dimension the effect of a difference between the actual position  $X$  and the measured position  $X_m$ . We will assume that  $X - X_m = \xi$  is randomly distributed with variance  $\sigma_p$ , and that there may be a progressive error i.e. the mean value  $\langle \xi \rangle \neq 0$ . We now define an error in the measurement due to limited instrument resolution

as  $\zeta_{res}$ , and an error due to positional error  $\zeta_p$ . Referring to figure 5.7.2 it may be seen that:

$$\zeta_p = \xi \psi_0 \quad (43)$$

where  $\psi_0$  is the instantaneous gradient.

Now  $\zeta_{res}$  and  $\zeta_p$  are independent random variables so that the effective variance of the measurement is:

$$\sigma_z^2 = \sigma_{res}^2 + \sigma_{\zeta_p}^2 \quad (44)$$

Now the contribution to the variance from positional error is:

$$\sigma_{\zeta_p}^2 = \langle (\xi \psi_0)^2 \rangle - \langle \xi \psi_0 \rangle^2 \quad (45)$$

and since  $\xi$  and  $\psi_0$  are independent,

$$\sigma_{\zeta_p}^2 = \langle \xi^2 \rangle \langle \psi_0^2 \rangle - \langle \xi \rangle^2 \langle \psi_0 \rangle^2 \quad (46)$$

The mean gradient  $\langle \psi_0 \rangle$  is zero therefore:

$$\sigma_{\xi_p}^2 = \langle \xi^2 \rangle \langle \psi_0^2 \rangle \quad (47)$$

Now the variance of positional error  $\xi$  is:

$$\sigma_p^2 = \langle \xi^2 \rangle - \langle \xi \rangle^2 \quad (48)$$

so substituting in equation (47) we find:

$$\sigma_{\xi_p}^2 = \langle \psi_0^2 \rangle (\sigma_p^2 + \langle \xi \rangle^2) \quad (49)$$

using equation (44) the effective variance of the measurement is:

$$\sigma_z^2 = \sigma_{res}^2 + \langle \psi_0^2 \rangle (\sigma_p^2 + \langle \xi \rangle^2) \quad (50)$$

If the mean error in position  $\langle \xi \rangle$  is zero, i.e. there are no systematic errors in the corrected position, then equation (50) becomes:

$$\sigma_2^2 = \sigma_{res}^2 + \langle \psi_0^2 \rangle \sigma_P^2 \quad (51)$$

It may be shown that:

$$\langle \psi_0^2 \rangle = \frac{\beta_0^2}{2} \quad \text{where} \quad \tan \beta_0 = \frac{2\sigma_1}{T} \quad (52)$$

(Beckmann and Spizzichino,  
1963, p. 89)

Note  $T$  is defined by equation (42).

For a small mean-square gradient using equation (52) in equation (51) we find the important result that the effective variance in the measurement is:

$$\sigma_2^2 = \sigma_{res}^2 + 2 \sigma_P^2 \frac{\sigma_1^2}{T^2} \quad (53)$$

thus formalizing the intuitive result that to maximize the information gathered we require accurate navigation and precise measurement of the property.

The information  $J$ , gained in a single measurement,

is then:

$$J = \log_2 \left\{ \sigma_i e^{\frac{-(z_m - \langle z \rangle)^2}{2\sigma_i^2}} \right\} - \frac{1}{2} \log_2 \left\{ \sigma_{res}^2 + 2 \frac{\sigma_p^2 \sigma_i^2}{T^2} \right\} \quad (54)$$

As a function of instrument resolution, or positional error,  $J$  has the form  $J = A - B \log(C + x)$  where  $A$ ,  $B$  and  $C$  are constants and  $x$  is  $\sigma_{res}$  or  $\sigma_p$ : this is illustrated in figure 5.7.3. The knee of the curve occurs when the value of  $J$  is reduced equally by the sensor resolution and by the navigational accuracy, which corresponds to:

$$\sigma_{res} = \sqrt{2} \frac{\sigma_p \sigma_i}{T} \quad (55)$$

It is clear from the diagram that improving the sensor resolution beyond  $\sigma_{res} < \sqrt{2} \frac{\sigma_p \sigma_i}{T}$  does not increase the quantity of information gained and conversely it is unprofitable to improve the navigational accuracy more than:

$$\sigma_p < \sigma_{res} T / \sqrt{2} \sigma_i^2$$

As an example, consider the measurement of ice thickness to a resolution of 10 m. The XY auto-correlation distance depends on the area in question, but on a floating ice shelf it may be as much as 50 km. The standard deviation of thickness in such an area is perhaps 100 m. The critical figure for navigational accuracy

is then about 3.5 km in position. However, in an area where the ice is disturbed by underlying rock the autocorrelation distance would be much less, and the demands made upon navigation correspondingly greater. In particular an area where the subglacial topography is mountainous may have an autocorrelation distance of only 5 km and the standard deviation of thickness may be 500 m. In this case the critical navigational accuracy would be about 70 m. If the navigational accuracy were worse than this figure, the quantity of information gained would be accordingly less. For example, if positions were accurate to about 1 km, this would correspond to a resolution in thickness of about 150 m which is considerably worse than the limit imposed by the sensor resolution.

The ice surface of the inland Antarctic plateau is remarkably smooth. Measurements conducted during a radio echo sounding flight in latitude 130°E longitude 73°S indicate an autocorrelation distance of 500 km. The uncertainty in elevation measurement is at least 100 m, using aneroid altimetry with little control, and the standard deviation of the height distribution was 1000 m. These figures indicate that to conduct surface altimetry by this technique the critical uncertainty in position is 20 km.

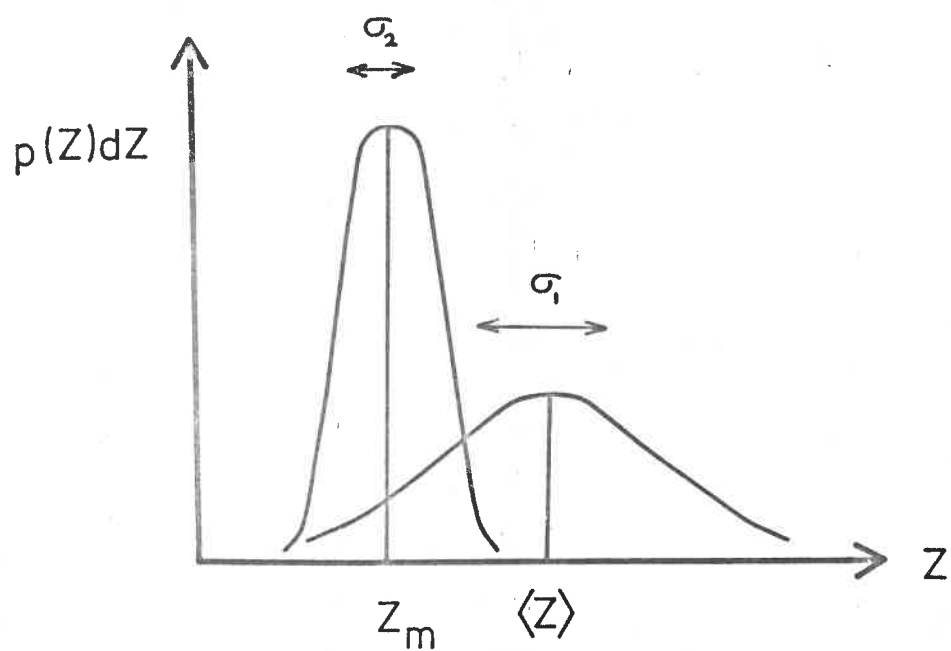


Figure 5.7.1

Showing the probability distribution of  $Z$  value before ( $\sigma_1$ ) and after ( $\sigma_2$ ) measurement.



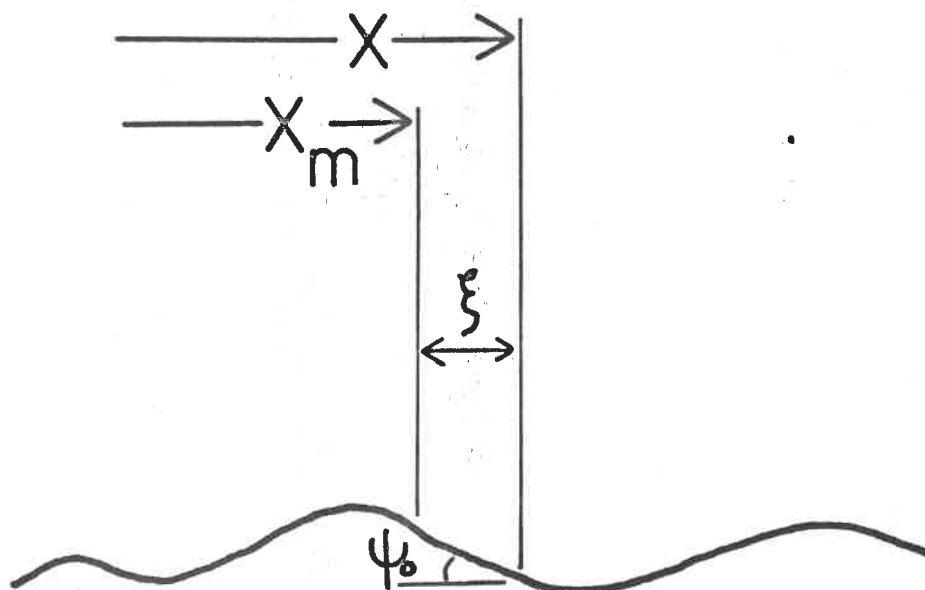


Figure 5.7.2

Showing the effect of an error in position on the instantaneous measured value.

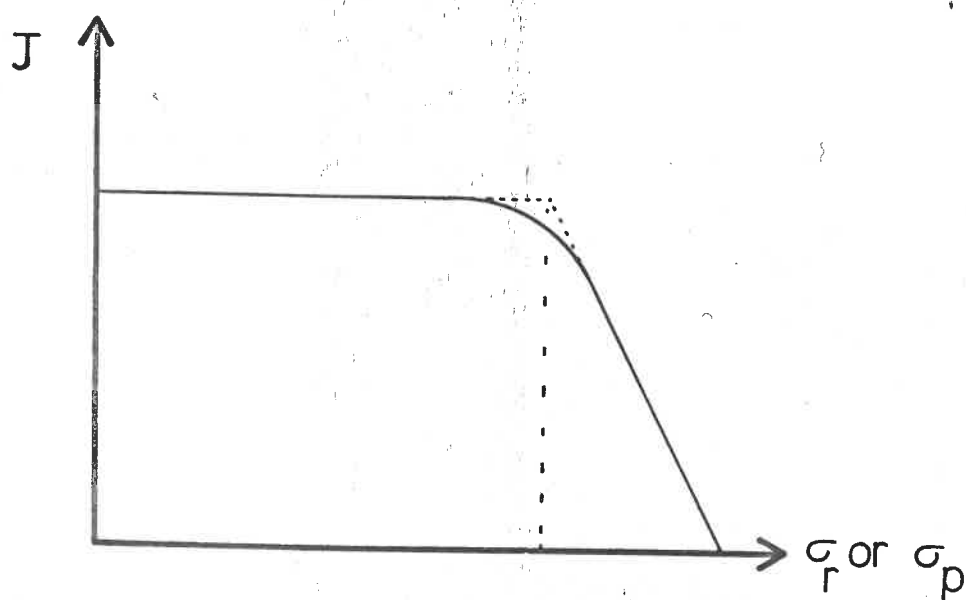


Figure 5.7.3

Showing the way in which  $J$ , the information gained, decreases with increasing uncertainty in position or measurement.

## CHAPTER 6

The presentation of radio echo sounding results6.1 The purpose of presentation and the distribution of the data

The presentation of measured data for publication or study, is the natural conclusion of the process of measurement. Measurements of ice thickness usually form part of a survey, the results of which are of interest to a wide audience. For this reason, a method of presentation must be found which makes the data available in the most useful form. Consideration must be given to the extent to which a method of presentation imparts a clear understanding of the data, as well as to the accuracy of the method.

Measurements made using a radio echo sounder constitute samples of a single valued function of two dimensions. Although ice thickness is the principal measurand, it should be remembered that other information may be obtained. The received echo strength allows the ice conductivity to be deduced. This in turn conveys some information about ice temperature. In the case of airborne echo sounding, surface elevations (and hence bottom elevations) may be determined from the available data. Also there may be several reflecting horizons within the ice, the ranges of which may be measured. There are, therefore, several possible measurands, each being a function of two variables, and all having the same distribution of measurement points.

Radio echo sounding measurements are distributed in the plane

of measurement in a way which is not necessarily similar to other measurements of a function of two variables. Because of the method that is used to record data, measurements are made very rapidly in time, and hence as the observer moves, measurements are made at points which are very close together along the path of the observer. The typical spacing between lines of measurement will usually be much more than the spacing between adjacent data points along the lines, although the lines may cross in some places. We will refer to this distribution of data as 'linearized'. Some functions of two variables are usually measured at random points in the plane of measurement. Barometric pressure, for example, is measured at meteorological stations which are not regularly spaced. However, most functions of two dimensions which are measured by a moving observer, have the linearized distribution of measurement points. The methods of presentation which we will apply to ice thickness may also be applied to these other data. Certain methods of presentation can only be used for linearized data, while others must be adapted to suit this distribution.

Both random and linearized data approach a total knowledge of the function, if the distance between data points is everywhere much less than the auto-correlation distance. However, for the ice thickness measurements so far completed, this is not the case and the data are considered to be linearized.

## 6.2 Notes on the data used to illustrate the methods of presentation

In order to compare the various methods of presentation, a fictitious set of measurements has been devised to illustrate as many features as possible. It represents the results of ice thickness measurement from the air. It was devised by creating a fictional surface by means of contours, defined over a rectangular area. A flight track was then superimposed on the contour map, and values were read off at regular intervals. The original surface consisted of a region of uniform ice thickness ( $\approx 400$  m) in the south-east of the area; a region of uniform ice thickness ( $\approx 600$  m) in the north-west of the area; and, separating the two, a band of thin ice ( $\approx 100$  m) running diagonally from the south-west and curving to the east to meet the easterly edge of the rectangle.

The flight track consists of a relatively straight path from south-east to north-west followed by loops which repeatedly cross the band of thin ice. The resulting pattern contains several points where tracks cross each other, places where the flight track crosses the band of thin ice at right angles and obliquely, and places where the flight track is parallel to the contours. There are also places (the north-east and south-west corners) where the flight track does not visit, and hence where the data is undefined.

### 6.3 Presentation methods applicable to all distributions of data

Any data, randomly scattered or linearized, densely or sparsely distributed, can be tabulated. The coordinates of the measurement and the measured value are printed in a list. Figure 6.3.1 shows such a table representing a part of the example data. Comment seems unnecessary but this method is potentially the most precise. If there are many data points it is difficult to appreciate the data and this method of presentation imparts little information at a glance.

A chart of the data points on which the measured values are written as numbers at the positions of measurement, is another method of presentation which can be used for data in any distribution. It is used on Admiralty charts, with the addition of a few submarine contours. It has some of the advantages of a graphical display, being easier than a table to visualize, and it retains the accuracy of quantified measurement. Figure 6.3.2 shows a chart of the example data. The method has been modified to suit linearized data. A computer program has been written by the author, which plots successive measurements at right angles to the line joining each measurement to the previous one. In this way the numbers are perpendicular to the track so that the values may be read when the track is parallel to the bottom edge of the chart. The method is not feasible if there are many data points and the advantage of accuracy is to some extent outweighed by the perspicuity demanded of the reader.

# ICE THICKNESS MEASUREMENTS

## LATITUDE LONGITUDE THICKNESS

1.217707	1.116810	410
1.217376	1.117440	405
1.217027	1.118068	400
1.216681	1.118659	395
1.216341	1.119277	390
1.216001	1.119856	385
1.215648	1.120445	380
1.215329	1.121094	370
1.215033	1.121670	360
1.214642	1.122408	350
1.214326	1.122973	340
1.213982	1.123699	330
1.213676	1.124334	315
1.213325	1.125048	300
1.213012	1.125707	180
1.212695	1.126428	95
1.212394	1.127130	95
1.212074	1.127848	180
1.211754	1.128494	440
1.211418	1.129174	510
1.211082	1.129844	530
1.210755	1.130548	540
1.210432	1.131154	550
1.210126	1.131857	560
1.209809	1.132487	570
1.209497	1.133179	580
1.209147	1.133859	590
1.208811	1.134203	600
1.208431	1.133893	605
1.208249	1.132909	600
1.208193	1.131842	595
1.208227	1.130767	590
1.208392	1.129721	580
1.208506	1.128825	570
1.208908	1.128025	560
1.209225	1.127322	550

Figure 6.3.1

A table of part of the example data showing the coordinates of each measurement point together with the value of the measurand.

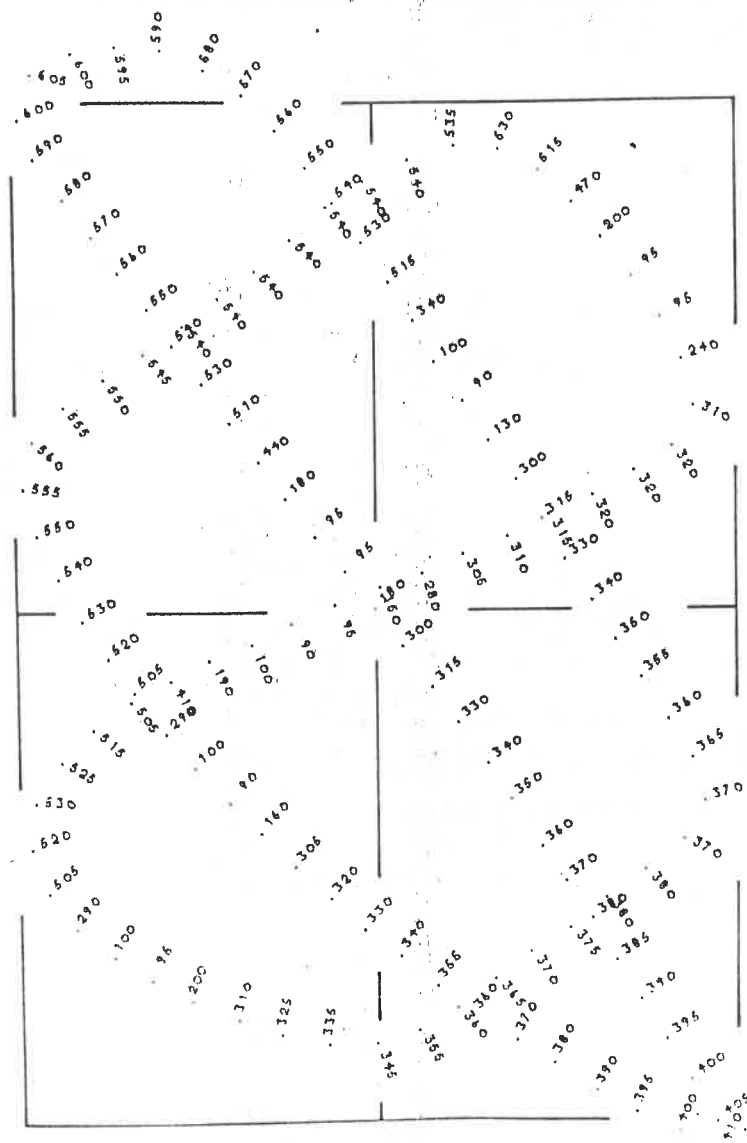


Figure 6.3.2

A chart of the example data with the value of the measurand written at the point of measurement.



#### 6.4 Presentation methods applicable to linearized data

Since the data in which we are interested are measured along the path of the observer, they can be treated as a function of one dimension: movement of the observer. It is then possible to plot the measured value against distance moved and obtain a profile of the data. This is a clear and concise graphical presentation which can be accurately quantified. It is ideal if the lines of measurement are nearly straight. Figure 6.4.1 shows a profile of the initial straight part of the flight track in the example data. It covers approximately the same part of the data as the table in figure 6.3.1. The computer program which produced the profile obtains the abscissa by summing the distances between successive positions of measurement. If the lines of measurement are curved and frequently crossing, a profile is liable to mislead. In the favourable case where many lines are almost parallel, as in a radio astronomy survey, profiles plotted in their correct relative positions in two dimensions give a good perspective impression. This will not usually be applicable to radio echo sounding measurements.

A modification of the simple profile is the 'fence diagram'. In this method the path of measurement is plotted as a track, and at each point along the track a line of length proportional to the measured value is plotted. All these lines are made parallel to induce the impression of perspective. Figure 6.4.2 shows a fence diagram of the example data. If the path of measurement

is almost parallel to the direction chosen for the fence posts then the detail is obscured. Otherwise the method provides a useful impression of the data, which is quantified by defining the scale of the fence posts.

Data points which are a function of one dimension can be plotted on two-dimensional paper. In general, a function of  $n$  dimensions can be plotted on an  $(n+1)$  dimensional surface. Our data points which are a function of two dimensions can be represented as a locus in three-dimensions. Two projections of this locus can be computed which, when viewed stereoscopically, produce the impression that the data points are distributed above the plane of measurement at heights according to their measured value. Figure 6.4.3 shows a stereo-pair of projections for the example data. This method gives a good appreciation of the data but is not easily quantified and not everyone adapts easily to stereo viewing. An alternative method of presenting this three-dimensional locus is possible if a general purpose digital computer and an on-line interactive graphical display terminal are available. Such a facility at the University Computer Laboratory, Cambridge, has been programmed by A.P. Armit of the Laboratory, to produce an isometric projection of a set of data points; the projection can be rotated by means of a joy-stick to give the impression that the points have their correct spatial relationships. This has been used to produce the two projections in figure 6.4.3, and figure 6.4.4

shows one such projection re-drawn with the omission of the hidden lines. The problem of computing a projection with the omission of hidden lines is very much more difficult than the basic projection algorithm, and this has not been undertaken. The result is, however, most pleasing.

Crude contours or height bars can be plotted along the path of measurement and aligned at right angles to it. Only adjacent data points are used to find the position of each contour line by means of linear interpolation and the computer program devised, does not take account of information about gradients perpendicular to the tracks. Figure 6.4.5 shows this method applied to the example data.

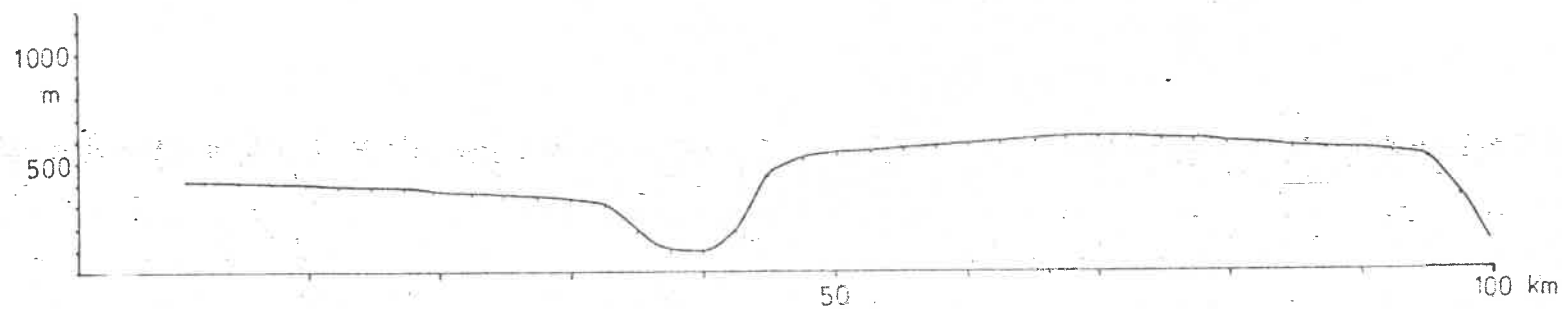


Figure 6.4.1

A profile of the initial linear part of the example data.

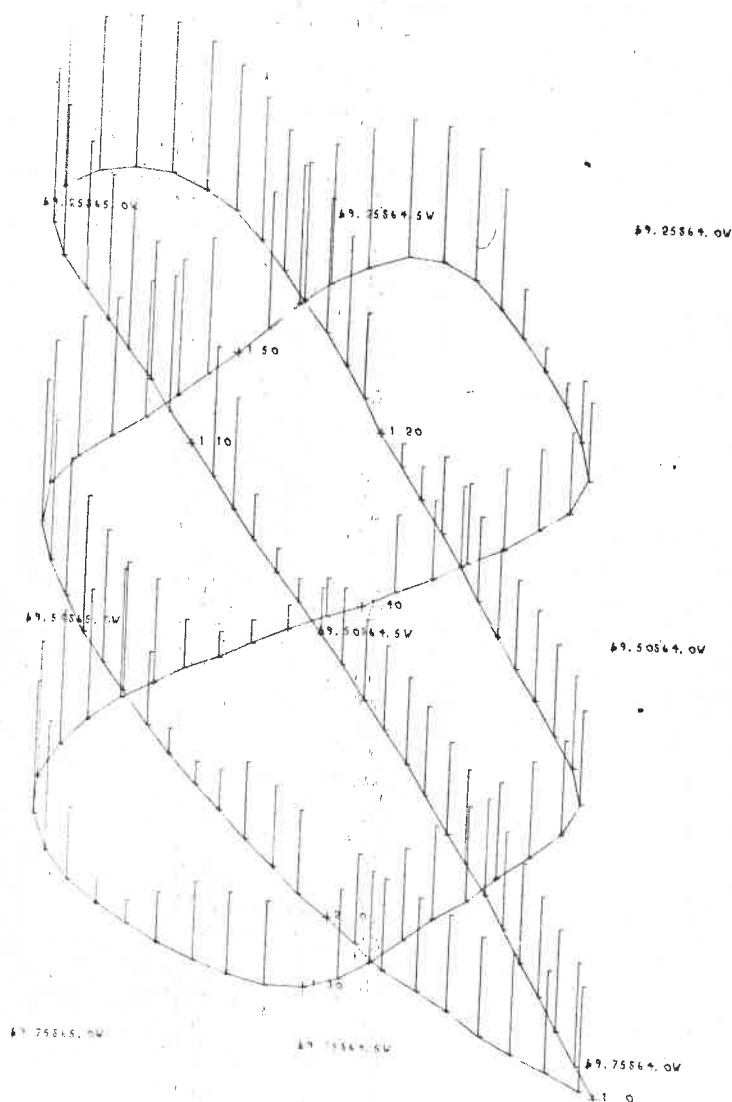


Figure 6.4.2

A fence diagram of the example data. The length of the fence posts is proportional to the size of the measurand.

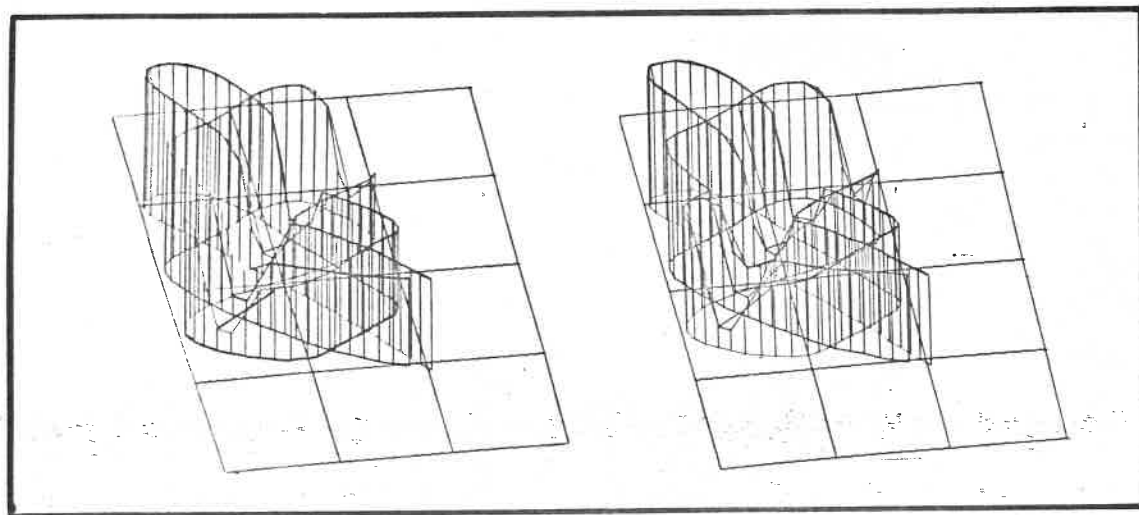


Figure 6.4.3

A stereo pair of isometric projections of the example data.

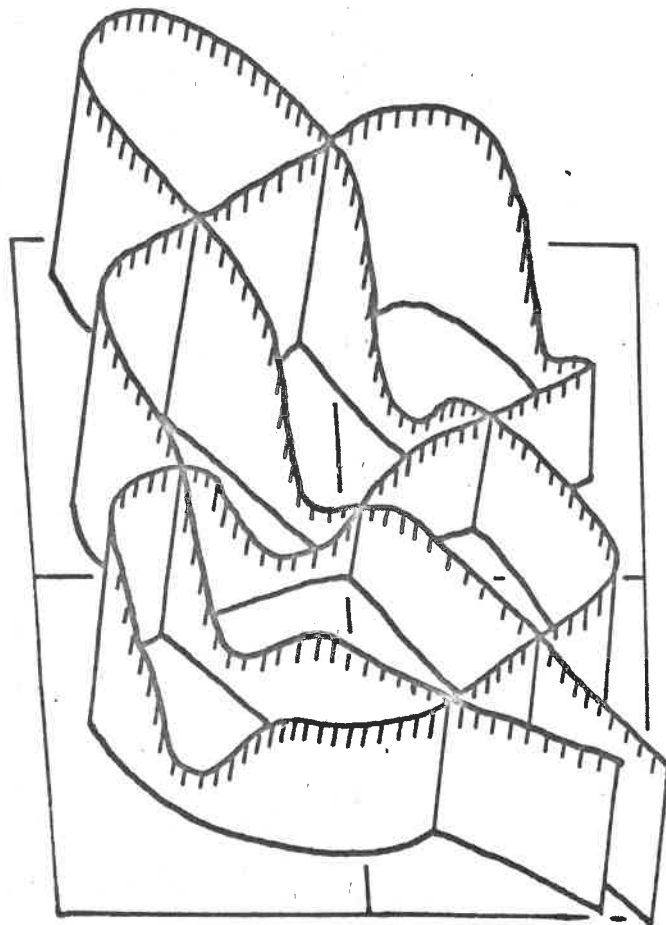


Figure 6.4.4

An isometric projection of the example data,  
re-drawn with the omission of the hidden lines to  
improve the clarity of the presentation.





### 6.5 Generalizing data using polynomials

A contour map is perhaps the commonest method of presenting a function of two variables. It assumes, that the function is defined over the whole area which is to be contoured but in our case, the function is only defined at certain points. When sparse data are manually contoured, some preconceived ideas are employed to interpolate; the process is somewhat subjective and not repeatable. Some criteria should therefore be formulated to allow the process to be accomplished by a digital computer. Standard computing routines after Bengtsson and Nordbeck (1964) exist to contour a rectangular matrix of data points but unless the property has been measured in this way, a generalized surface must be generated from the measurements by means of some interpolation algorithm.

One obvious method of producing a smooth surface which fits the source data, is to use a least squares analysis to derive a best-fit polynomial function. The author has written a computer program that solves the necessary simultaneous equations to obtain the coefficients of a two-dimensional polynomial function of any chosen order, such that the sum of the squares of the residuals, between the measurements and the surface, is a minimum. This process has been applied to the example data for functions up to the fifth order. The fifth order two-dimensional polynomial has 21 terms, including terms in  $x^4y$ ,  $x^3y^2$ ,  $x^2y^3$ ,  $xy^4$  as well as  $y^5$

and the similar lower order terms. The coefficients of these polynomials have no physical significance, although a similar analysis of some other measurements which were expected to conform to a certain polynomial, might yield coefficients with some physical meaning. In general, measurements of ice thickness will not represent a polynomial surface although it is true that  $n$  data points can be fitted exactly by a polynomial of order  $(n-1)$ . Such a polynomial is likely to have bizarre values in areas without data points.

Having obtained a least-squares-fit function, the surface can be defined over the necessary area, and then it may be contoured in the standard manner. As an alternative, a perspective grid of the generalized surface gives a useful impression of the shape of the function. Figures 6.5.1 to 6.5.5 show contour diagrams alongside perspective grids for the two-dimensional least squares polynomials of order 1 to 5 respectively. The source data points are marked on the contour diagrams, and the perspective grids represent the same area as the contour diagram, viewed from the south-west corner, above the plane. The first order surface is simply an inclined plane. With increasing order, the effect of the band of thin ice across the area becomes more apparent. Unfortunately, at the same time, the surface assumes more and more improbable values in the gaps in the data. In the case of the fifth order polynomial, the excursions of the surface in the north-

east and south-west corners necessitated the omission of part of the perspective grid. It appears that two-dimensional least squares polynomials will either omit important information at low orders, or create spurious data at higher orders and we must therefore seek some alternative method of interpolating the data.

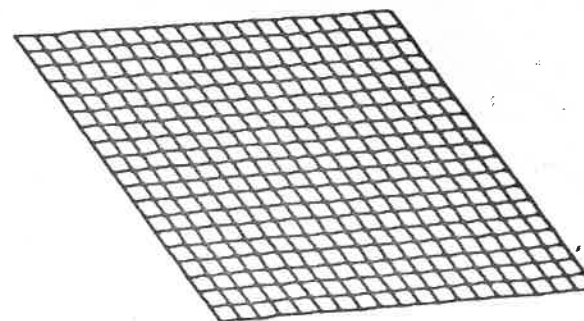
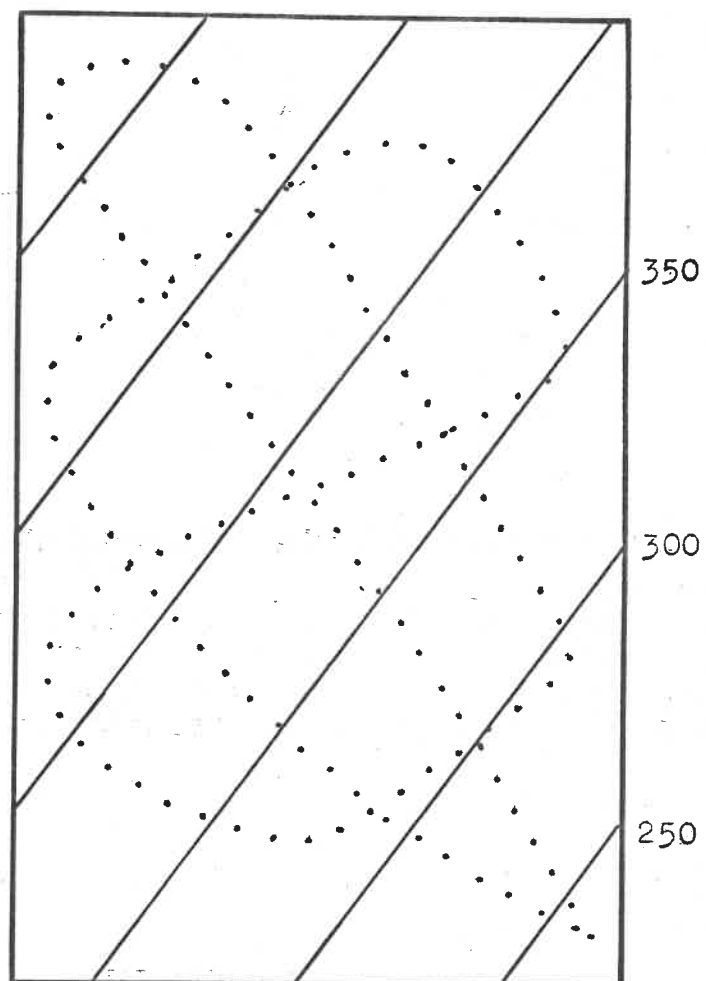


Figure 6.5.1

A first order two-dimensional least-squares polynomial.  
On the left a contour map, on the right a perspective grid.

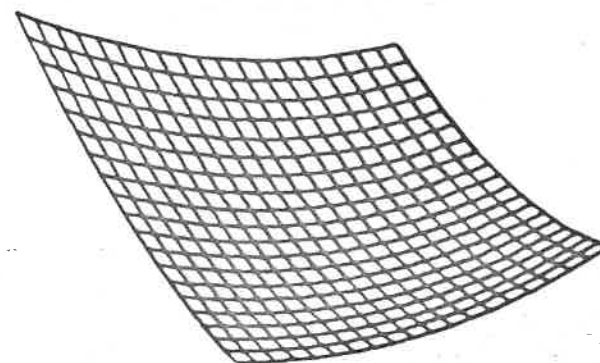
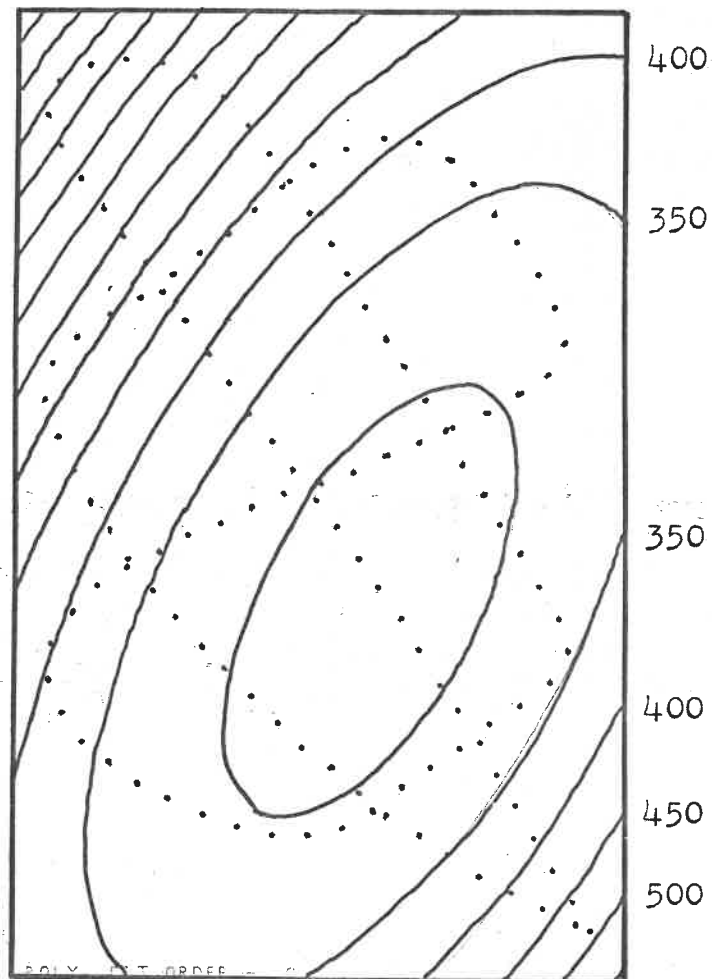


Figure 6.5.2

A second order two-dimensional least-squares polynomial.  
On the left a contour map, on the right a perspective grid.

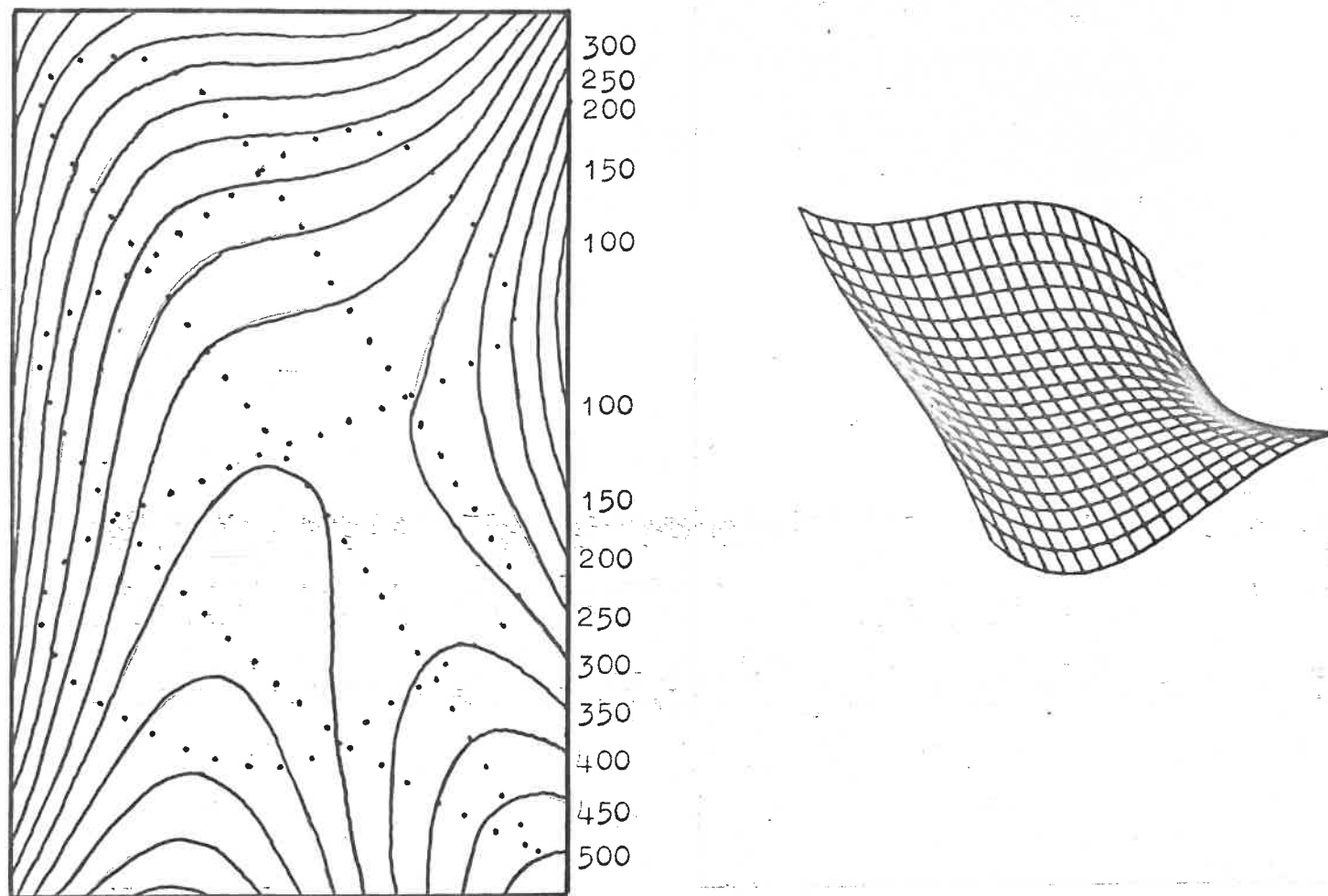


Figure 6.5.3

A third order two-dimensional least-squares polynomial.  
On the left a contour map, on the right a perspective grid.

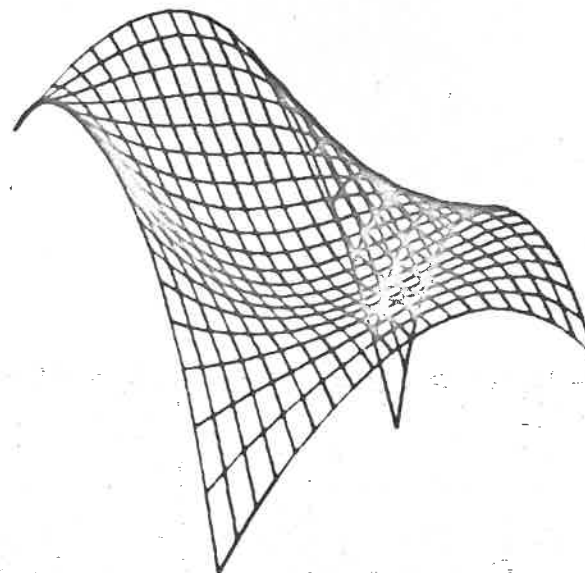
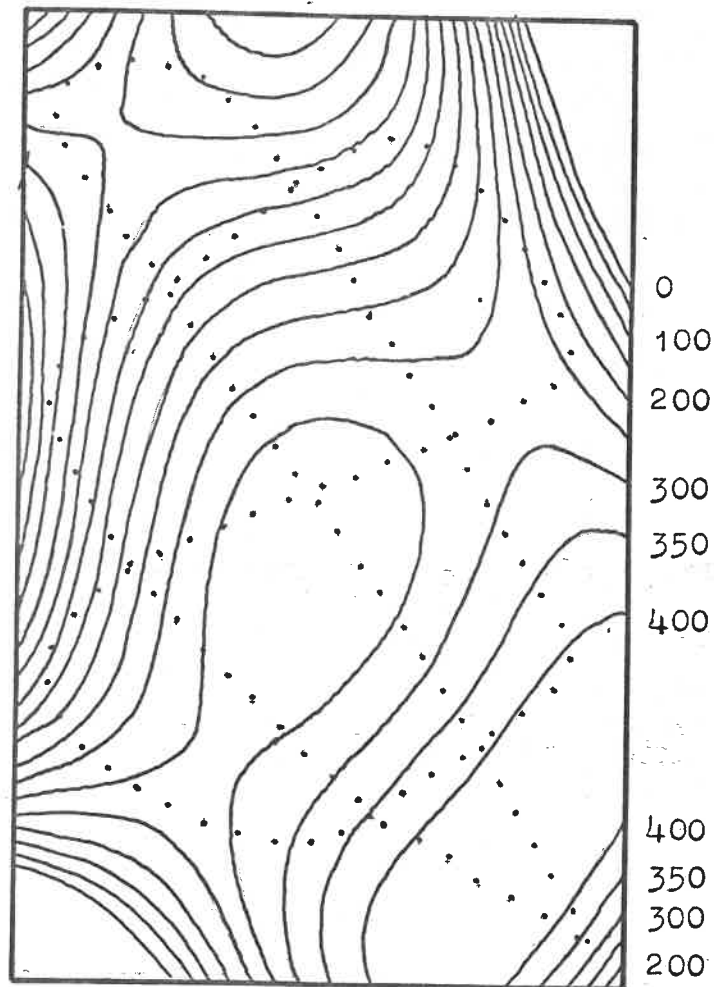


Figure 6.5.4

A fourth order two-dimensional least-squares polynomial.  
On the left a contour map, on the right a perspective grid.

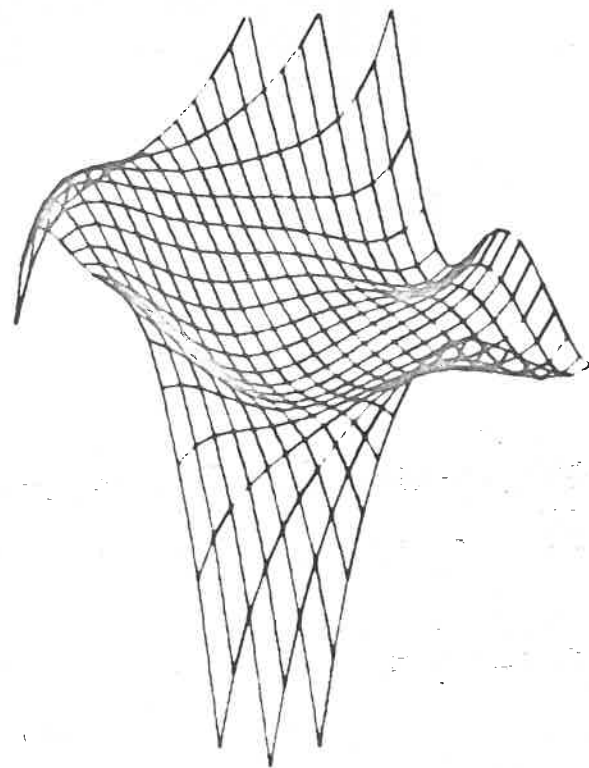
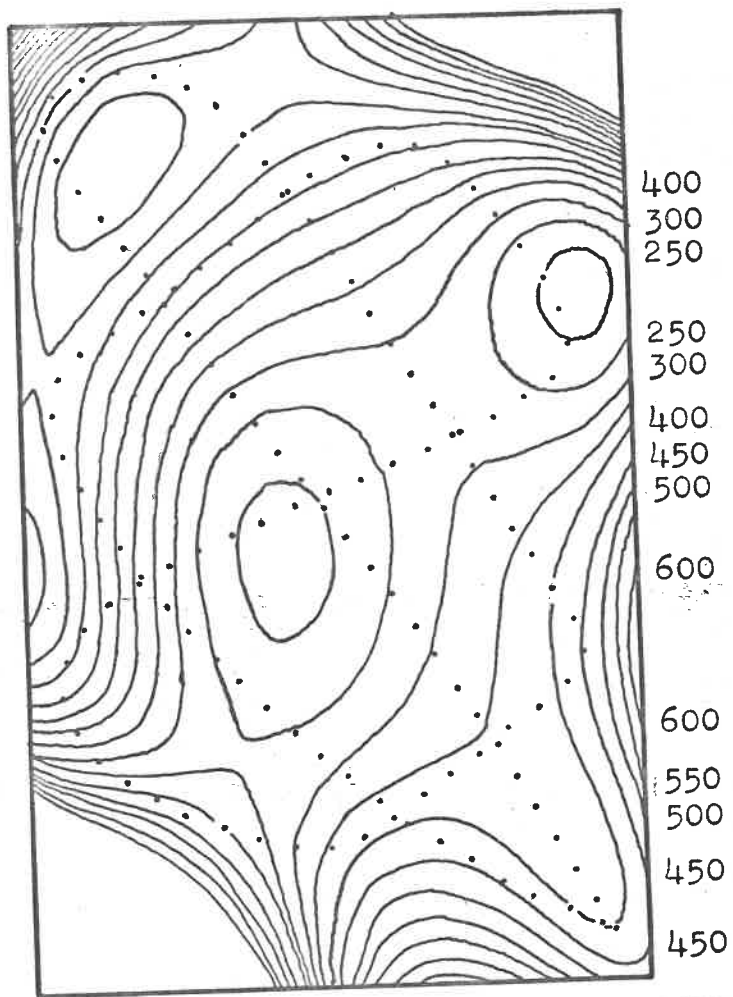


Figure 6.5.5

A fifth order two-dimensional least-squares polynomial.  
 On the left a contour map, on the right a perspective grid.



## 6.6 Generalizing data using other algorithms

Cole (1969) has proposed an algorithm to produce a generalized surface from randomly scattered data points. The surface which he suggests is actually a matrix of values chosen to represent the surface. The initial values of the matrix points are obtained from a least squares two-dimensional polynomial fitted to all the data points. This 'global' surface is usually of second order and is derived in the same way as the surfaces in the previous section. It is then modified by 'local' least squares second order polynomial functions based on the 3 by 3 matrix round each data point. The modified matrix is then smoothed by means of an algorithm which removes discontinuities of gradient between the 'global' and 'local' surfaces but does not affect quadratic surfaces. The algorithm is made iterative by using the matrix obtained, as the new 'global' surface for a repeat of the operation. The net effect of this process is the production of a smooth surface which passes through the data points. For well scattered data, the algorithm is very successful, but when the data points are distributed along lines, improbable results have been obtained. Figure 6.6.1 shows the contour map and perspective grid derived from the example data using Cole's method. In areas where the data are absent, the algorithm tends to extrapolate first and second derivatives. In practice this is not always the most desirable. Imagine a line of measurement points passing over a 'hill' in the measured property.

If the path deviates slightly from a straight line as it crosses the hill, this would be interpreted as a steep slope perpendicular to the track. However, this would not be the subjective evaluation of the data because such steep slopes are not found at any point along the path of measurement. When the source data are linearized, more information about the statistical nature of the surface is available. We have therefore modified Cole's algorithm to improve these two aspects; the extrapolation of first and second derivatives, and the use of the statistical information.

We propose that on a large scale, neither the first nor second derivatives of the measured property can be extrapolated indefinitely. Instead, in areas without data, we tend to expect a horizontal plane. This is true for ice thickness, which is related to topography, but may not be valid for other types of property. Bearing this in mind, the initial matrix of Cole is set equal to the value of the nearest data point. Then a single data point yields a single-valued plane, and at points away from the data, the resultant surface tends to the value of the nearest data point. In this way, improbable cross track gradients are not produced because initially the matrix values at either side of the track are equal to the value on the track, although there will in general be discontinuities between tracks. If the property being contoured has known discontinuities within the area of the matrix, in particular if there is a boundary (e.g. a known coastline, rock

If the path deviates slightly from a straight line as it crosses the hill, this would be interpreted as a steep slope perpendicular to the track. However, this would not be the subjective evaluation of the data because such steep slopes are not found at any point along the path of measurement. When the source data are linearized, more information about the statistical nature of the surface is available. We have therefore modified Cole's algorithm to improve these two aspects; the extrapolation of first and second derivatives, and the use of the statistical information.

We propose that on a large scale, neither the first nor second derivatives of the measured property can be extrapolated indefinitely. Instead, in areas without data, we tend to expect a horizontal plane. This is true for ice thickness, which is related to topography, but may not be valid for other types of property. Bearing this in mind, the initial matrix of Cole is set equal to the value of the nearest data point. Then a single data point yields a single-valued plane, and at points away from the data, the resultant surface tends to the value of the nearest data point. In this way, improbable cross track gradients are not produced because initially the matrix values at either side of the track are equal to the value on the track, although there will in general be discontinuities between tracks. If the property being contoured has known discontinuities within the area of the matrix, in particular if there is a boundary (e.g. a known coastline, rock

exposure, etc.) beyond which contours should not be plotted, then any data from beyond the boundary is omitted (the survey is discontinued at the boundary) and, after contouring, the plane surface which will extend beyond the boundary into the area without data, is ignored. The 'local' quadratic least squares fit of Cole has been retained since on a small scale these extrapolations are permitted. The principal change to Cole's algorithm comes in the smoothing. The computer program scans the source data along the survey lines, and the root mean square gradient between adjacent data points is determined. We now assume that the function which has been measured, has statistical properties which are isotropic. To be more specific, we assume that the mean square gradient observed along the track is the same as that expected across the track. We therefore smooth the matrix by an amount which increases rapidly for gradients greater than the r.m.s. gradient determined along the track. The gradient in the vicinity of each point is found, and the  $Z$  value is changed by an amount proportional to  $(a/1+a)$  in such a way as to reduce the gradient; where  $a$  is the ratio between the local gradient and the r.m.s. measured gradient. Thus a matrix is produced, representing a smooth surface which passes through the data points and has the same statistical properties as the source data. The method is only possible because the data are distributed along lines, and it is not suitable for randomly scattered data. The matrix obtained is then contoured

at some chosen contour interval or presented as a perspective grid, as shown in figure 6.6.2 for the example data. The contour maps in chapter 4 were produced by this method.

\* For comparison, the transparent overlay shows the contours from which the source data were derived.

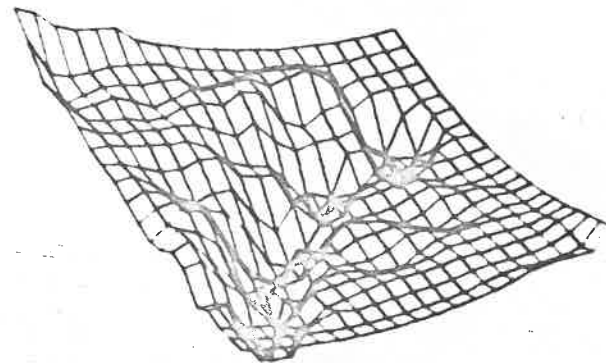
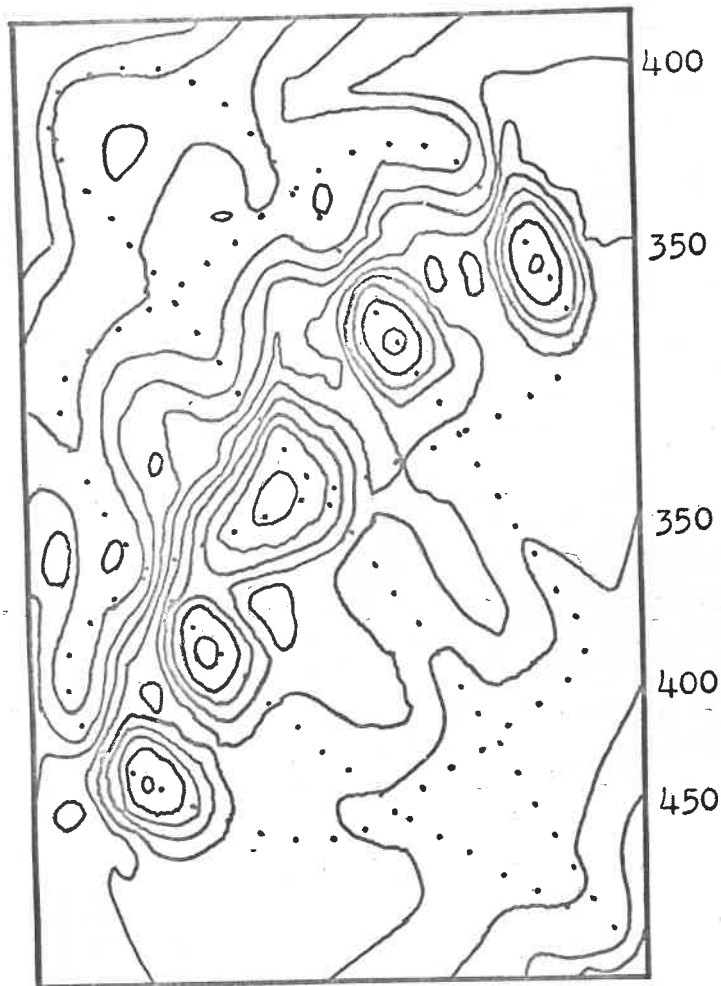


Figure 6.6.1

A contour map and a perspective grid of the example data  
interpolated using Cole's algorithm.\*

\* For comparison, the transparent overlay shows the contours from which the source data were derived.



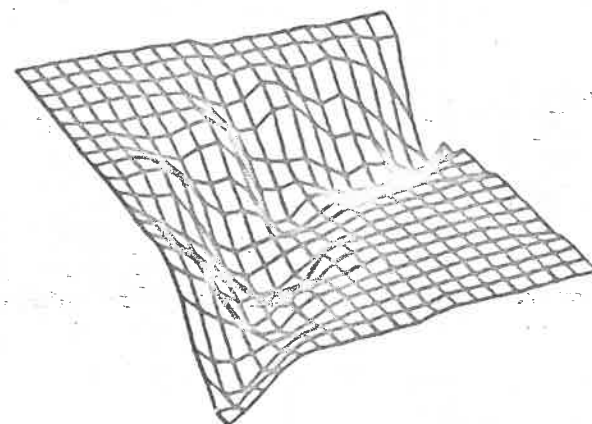
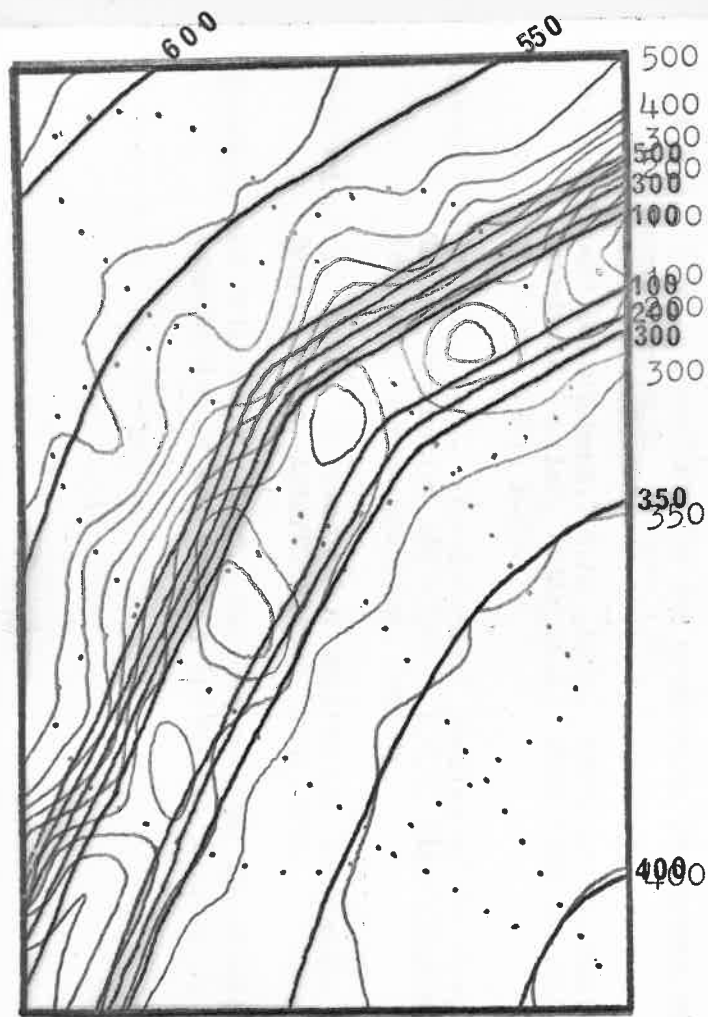


Figure 6.6.2

A contour map and a perspective grid of the example data  
interpolated using the author's algorithm.\*

## REFERENCES

-----

- Bailey, J.T. Evans, S. and Robin, G. de Q. 1964. Radio echo soundings of polar ice sheets. *Nature*, 204, No4957, p420.
- Bailey, R. 1951. Aperiodic aerials. *Wireless Engineer*, 28, p208.
- Beckmann, P. and Spizzichino, A. 1963. The scattering of electromagnetic waves from rough surfaces. Pergamon Press, London.
- Bengtsson, B.E. and Nordbeck, S. 1964. Construction of isarithms and isarithmic maps by computers. *BIT*, 4, p87.
- Bentley, C.R. 1964. The structure of Antarctica and its ice cover. *Research in Geophysics*, MIT Press, 2, p335.
- Budd, W. 1966. The dynamics of the Amery Ice Shelf. *J. Glaciol.*, 6, No45, p335.
- Bull, C. and Hardy, J.R. 1956. The determination of the thickness of a glacier from measurements of the value of gravity. *J. Glaciol.*, 2, No20, p755.
- Cole, A.J. 1969. Algorithm for the production of contour maps from scattered data. *Nature*, 220, p92.
- Collins, I. and Swithinbank, C.W.M. 1969. Rifts at the foot of the Beardmore Glacier, Antarctica. *IUGG/IASH General Assembly of Berne*, 1967, p109.
- Crary, A.P. et al. 1962. Glaciological Studies of the Ross Ice Shelf, Antarctica 1957-1960. *I.G.Y. Glaciological Report No6*. American Geographical Society.
- Dubrovin, L.I. 1962. O rassolakh v shel'fovykh lednikakh. *Inform. Byull. Sovet. Antark. Eksped.* No35, p35.
- Egner, H. and Eriksson, E. 1955. Current data on the chemical composition of air and precipitation. *Tellus*, 7, p134.

- Evans, S. 1961. Polar ionospheric spread echoes and the radio frequency properties of ice shelves. *J. Geophys. Res.*, 66, No12, p4137.
- Evans, S. 1963. Radio techniques for the measurement of ice thickness. *Polar Rec.*, 11, No73, p406. and No75, p795.
- Evans, S. 1965. Dielectric properties of ice and snow. *J. Glaciol.*, 5, No42, p773.
- Evans, S. 1966. Progress report on radio echo sounding. *Polar Rec.*, 13, No85, p413.
- Evans, S. and Robin, G. de Q. 1966. Glacier depth sounding from the air. *Nature*, 210, No5039, p883.
- Evans, S. et al. 1969. Glacier sounding in the polar regions - A symposium. *Geog. Journ.*, 135, Pt4, p547.
- Evans, S. and Smith, B. M. E. 1969. A radio echo equipment for depth sounding in polar ice sheets. *J. Scient. Instrum.*, Series 2, 2, p131.
- Evans, S. and Smith, B. M. E. 1970. Radio echo exploration of the Antarctic Ice Sheet, 1969-70. *Polar Rec.*, 15, p336.
- Ewen-Smith, B. M. 1971. Airborne radio echo sounding of glaciers in the Antarctic Peninsula. *British Antarctic Survey Bulletin*, (in press).
- Gorham, E. 1958. Soluble salt in a temperate glacier. *Tellus*, 10, p496.
- Gow, A. J., Ueda, H. T. and Garfield, D. E. 1968. Antarctic Ice Sheet: preliminary results of first core hole to bedrock. *Science*, 161, p1011.
- Harrison, C. H. 1970. Reconstruction of subglacial relief from radio echo sounding records. *Geophysics*, 35, No6, p1099.
- Harrison, C. H. 1971. Radio echo sounding: Reflections from wavy layers in ice. (In preparation - *Geophysical Journal*).

- Hasted, J.B. 1961. The dielectric properties of water. *Progress in Dielectrics*, 3, p101.
- Heine, A.J. 1968. Brine in the McMurdo Ice Shelf, Antarctica. *N.Z. J. Geol. Geophys.*, 11, No4, p829.
- Kapitsa, A.P. 1960. New data on ice thickness in the central regions of Antarctica. *Sovet. Antarkt. Eksped. Inform. Byull.*, No19, p10.
- Kayton, M. and Freid, W.R. (Eds) 1969. *Avionics navigation systems*. Wiley, New York.
- Lawson, J.L. and Uhlenbeck, G.E. 1950. *Threshold signals*. Radiation Lab. Series, McGraw Hill, New York.
- Linton, D.L. 1964. Landscape evolution. *Antarctic Research* (Eds. Priestley, R. Adie, R.J. and Robin, G.deQ.), Butterworths London, p85.
- Müller, F. 1963. *Jacobsen-McGill Arctic Research Expedition, 1959-1962 Preliminary report, 1961-1962*. McGill University, Montreal.
- Norton, K.A. Vogler, L.E. Mansfield, W.V. and Short, P.J. 1955. The probability distribution of the amplitude of a constant vector plus a Rayleigh-distributed vector. *Proc. Inst. Radio Eng.*, 43, p1354.
- Nye, J.F. 1952. A method of calculating the thicknesses of the ice sheets. *Nature*, 169, No4300, p529.
- Nye, J.F. and Frank, F.C. 1971. The hydrology of the intergranular veins in temperate glaciers. *IUGG/IASH. Symposium on the Hydrology of Glaciers*, Cambridge, Sept., 1969.
- Paren, J.G. 1970. Dielectric properties of ice. Unpublished Ph.D. Thesis. University of Cambridge.
- Paren, J.G. 1971. Theory of heterogeneous dielectrics applied to glacier ice, sea ice, and snows. (In preparation - *Philosophical Magazine*).

- Paren, J.G. and Walker, J.C.F. 1971. Limited solubility in ice: Its influence on electrical and mechanical properties. *Nature*, 230, p77
- Parkhomenko, E.I. 1967. Electrical properties of rocks. Plenum Press, New York, 1967.
- Ramsayer, K. 1969. Integrated navigation by least squares adjustment. *J. Inst. Navigation*, 23, p174.
- Robin, G.deQ. 1956. Determination of the thickness of ice shelves by seismic shooting methods. *Nature*, 177, No4508, p584.
- Robin, G.deQ. 1958. Seismic shooting and related investigations. Norwegian-British-Swedish Antarctic Exp., 1949-1952, Scientific Results, Volume V.
- Robin, G.deQ. Swithinbank, C.W.M. and Smith, B.M.E. 1969. Radio echo exploration of the Antarctic Ice Sheet. ISAGE Symposium, Pub. No86 of IASH, p97.
- Robin, G.deQ. Evans, S. and Bailey, J.T. 1969. Interpretation of radio echo sounding in polar ice sheets. *Phil. Trans. Royal Soc., A*, 265, p437.
- Ronne, F. 1948. Ronne Antarctic Research Expedition, 1946-48. *Geog. Rev.*, 38, No3, p355.
- Röthlisberger, H. 1967. Electrical resistivity measurements and soundings on glaciers: introductory remarks. *J. Glaciol.*, 6, No47, p599.
- Saxton, J.A. 1950. Reflection coefficient of snow and ice at VHF. *Wireless Engineer*, Jan, 1950, p17.
- Steenenson, B.O. 1951. Radar methods for the exploration of glaciers. Unpublished Ph.D. Thesis, California Institute of Technology, Pasadena, California.
- Stern, W. 1930. Principles, methods, and results of electrodynamic thickness measurement of glacier ice. *Zeitschrift für Gletscherkunde*, 18, p24.
- Stratton, J.A. 1941. *Electromagnetic Theory*. McGraw Hill, New York.

- Swithinbank, C.W.M. 1968. Radio echo sounding of Antarctic glaciers from light aircraft. IUGG/IASH General Assembly of Berne, 1967, p405.
- Swithinbank, C.W.M. 1969. Giant icebergs in the Weddell Sea, 1967-68. Polar Rec., 14, No91, p477.
- Swithinbank, C.W.M. 1970. Ice movement in the McMurdo Sound area of Antarctica. ISAGE Symposium, Pub. No86 of IASH, p472.
- Tolstikov, Y.I. et al. 1966. Atlas Antarktiki I. Moscow, Glavnoye Upravleniye Geodezii i Kartografi. p28.
- Waite, A.H. and Schmidt, S.J. 1962. Gross errors in height indication from pulsed radar altimeters operating over thick ice or snow. Proc. Inst. Radio Eng., 50, p1516.
- Walford, M.E.R. 1964. Radio Sounding through an ice shelf. Nature, 204, No4956., p317.
- Walford, M.E.R. 1967. Radio echo sounding of polar ice masses. Unpublished Ph.D. Thesis, University of Cambridge.
- Walford, M.E.R. 1968. Field measurements of dielectric absorption in Antarctic ice and snow at VHF. J. Glaciol., 7, No49, p89.
- Weber, J.R. and Andrieux, P. 1969. Radar soundings on the Penny Ice Cap., Baffin Land. J. Glaciol., 9, No55, p49.
- Wilkins, H. 1929. The Wilkins-Hearst Antarctic Expedition, 1928-1929. Geog. Rev., 19, No3, p353.

CAMBRIDGE  
UNIVERSITY LIBRARY

Attention is drawn to the fact that the copyright of this thesis rests with its author.

This copy of the thesis has been supplied on condition that anyone who consults it is understood to recognise that its copyright rests with its author and that no quotation from the thesis and no information derived from it may be published without the author's prior written consent.